Dissertation

On the Characterization of Coated Conductors with the M-Scan Device

Ausgeführt zum Zwecke der Erlangung des akademischen Grades
eines Doktors der technischen Wissenschaften
unter der Leitung von

Dr. Alexander Usoskin
Bruker HTS GmbH
Privatdoz. Dipl.-Ing. Dr. techn. Michael Eisterer
E141
Atominstitut

eingereicht an der Technischen Universität Wien
Fakultät für Physik

von

Dipl.-Ing. Johannes GNILSEN
Matrikelnummer: 0926381

Wien, am 27.10.2021 Johannes Gnilsen

Acknowledgements

Construction and development of the M-Scan was conducted at the Bruker HTS GmbH. I want to thank my colleagues, the company and especially my supervisor Dr. Alexander Usoskin for his great support in this project.

This work is part of the EASITrain network.

EASITrain – European Advanced Superconductivity Innovation and Training. This Marie Sklodowska-Curie Action (MSCA) Innovative Training Networks (ITN) receives funding from the European Union's H2020 Framework Programme under grant agreement no. 764879.

Abstract

The characteristic feature of loss-free current transport in superconducting materials is -since its first discovery in 1911- stimulating ideas for fantastic technical applications. However, the requirements of cryogenic temperatures to reach the superconducting state, high critical fields and critical current densities as well as competitive prices impose limits on many superconducting compounds on their technical usage. Still, a handful of compounds have been discovered and enhanced such that they are suitable for implementation in applications as technical (super-)conductors.

The era of high-temperature superconductivity (HTS) started with the discovery of superconductivity in copper oxides in 1986 in the Ba-La-Cu-O system with a critical temperature in the range of 30 K [1]. A euphoric breakthrough was made the next year as superconductivity was discovered in the Y-Ba-Cu-O (YBCO) compound system at a critical temperature of 93 K [2] which is above the boiling point of liquid nitrogen. Comprehensive efforts of research and development were necessary to overcome issues to design conductors out of this material which are reliable to be used in superconducting assemblies. At the current state of the art, YBCO coated conductor tapes with a length of several hundred meters are commercially available from a couple of manufacturers.

YBCO coated conductors are also known as 2nd generation (2G) coated conductors, which -in comparison to the first generation of industrially manufactured $Bi_2Sr_2Ca_2Cu_3O$ (BSCCO) tapes- are not based on a multifilament architecture or *c*-axis aligned grains but rather rely on a biaxially textured thin-film layer structure. On top of a polished (non-magnetic) metallic substrate, buffer layers enable biaxially alignment of the superconducting film when it epitaxially grows during its deposition. Charge doping is performed after coating the conductor with oxygen permeable silver. Stabilization of the conductor is done with copper plating. In the end, the tapes are electrically insulated and have a thickness of ∼100 µm to 200 µm and typically a width of 4 mm.

The outstanding properties of HTS coated conductors, especially at low temperatures (i.e. 4.2 K), are a driving factor to further push their development. For example, upper critical fields above 100 T allow to exceed the practical limit of 23.5 T of the Nb_3Sn low temperature superconductor in magnet applications. A giant step in improving the flux density of superconducting laboratory magnets was performed in 2017/18, when a 32 T magnet with a HTS inlet coil became operational at the National High-Field Magnet Laboratory (NHFML) in Tallahassee [3]. Beside magnet applications research is done to employ HTS coated conductors in fault-current limiters, superconducting generators or power transmission cables. Near-future prospects in large-scale facilities for example are HTS based magnet coils of nuclear fusion reactors such as SPARC from the Massachusetts Institute of Technology (MIT) [4].

Quality control of the tape along its entire length is inevitable prior to its implementation in a technical device. Local defects in the functional layer of the conductor might significantly degrade the critical current locally which limits the total dissipation-free

current throughput.

Routine characterization of long-length tapes is typically performed via contact-free Hall array scans at 77 K in self-field (SF). Direct, 4-probe characterization scan techniques typically struggle at establishing dynamic noise-free contacts between the tape and the measurement device. The natural formation of ice on the tape surface during the characterization process turns out to be an issue as well.

In this work, a new continuous four-probe measurement method that scans superconducting tapes from one end to another in a 2.61 T flux zone and at 77 K was developed. In this device, called M-Scan, the tape continuously translates from a take-off reel through a bath of liquid nitrogen to a pick-up reel. Inside the bath, there is the four-probe measurement stage employing contact rollers and a permanent magnet with a channel through which the tape translates. This magnet generates the 4 cm long flux zone of 2.61 T. The voltage response of the tape, which is loaded with a pre-selected constant transport current, is continuously measured during its translation with rollers.

This thesis is split into three major parts, namely:

1. Development and implementation of the M-Scan device with focus on the description of the permanent magnet, the developed low-noise rollers and gas-flow heated feedthroughs that prevent the formation of ice on the tape surface during the scan procedure.

2. The development of the model to determine the critical current from the measured voltage response of the tape during its translation through the M-Scan device. The approach was experimentally verified with a sample in a 3 T pulsed electromagnet.

3. The main result is the experimental confirmation of the feasibility of the developed M-Scan device. The measured I_c-curves obtained from the M-Scan were further analyzed and discussed with the developed model. Finally, the impact of defects on the critical current was investigated and compared with results from Hall-array scans.

Kurzfassung

Die charakteristische Eigenschaft des verlustfreien Stromtransports in supraleitenden Materialien beflügelt, seit seiner Entdeckung im Jahr 1911, Ideen für vielversprechende technologische Anwendungen. Die Anforderungen, diese Materialien auf tiefkalte Temperaturen abzukühlen, um den supraleitenden Zustand zu erreichen, die Notwendigkeit von hohen kritischen Feldern und kritischen Stromdichten sowie wirtschaftliche Konkurrenzfähigkeit beschränken jedoch die Verwendung vieler supraleitender Verbindungen in der Technologie. Trotzdem wurden bisher eine Handvoll dieser diesen Anforderungen genügenden Verbindungen entdeckt und zu technischen Supraleitern weiterentwickelt.

Die Ära der Hochtemperatursupraleiter (HTS) begann 1986 mit der Entdeckung von Supraleitung in den Kupferoxiden im Ba-La-Cu-O System mit einer Übergangstemperatur im Bereich von 30 K [1]. Ein Jahr später kam es zum Durchbruch, als Supraleitung im Y-Ba-Cu-O (YBCO) System bei einer kritischen Temperatur von 93 K entdeckt wurde [2], die oberhalb der Siedetemperatur von flüssigem Stickstoff liegt. In weiterer Folge wurde viel in Forschung und Entwicklung investiert, um aus diesem Material einen technisch anwendbaren Supraleiter herzustellen. Nach aktuellem Stand der Technik werden YBCO Bänder (*coated conductor*) mit einer Länge von einigen hundert Metern von einigen wenigen Herstellern kommerziell gefertigt.

Die YBCO Bandsupraleiter sind auch als Bandsupraleiter der zweiten Generation (2G) bekannt, die - im Vergleich zu den industriell hergestellten Bandsupraleitern erster Generation ($Bi_2Sr_2Ca_2Cu_3O$ - BSCCO) - nicht auf einer Multifilamentstruktur oder in die *c*-Achse ausgerichteten Kristallkörnern, sondern auf einem biaxial texturierten dünnen Kristallfilm aufgebaut sind. Im Zuge des epitaxialen Beschichtungsprozesses wird die biaxiale Ausrichtung des supraleitenden Films durch Pufferschichten auf einem polierten, nichtmagnetischen Substrat ermöglicht. Der Supraleiter wird nach der Ummantelung mit Silber in einer Sauerstoffatmospäre beladen, das heißt mit Ladungsträgern dotiert. Am Ende wird der Leiter durch eine Kupferschicht stabilisiert. Nach der elektrischen Isolierung ist der Bandsupraleiter ca. 100 µm bis 200 µm dick und weist eine Breite von 4 mm auf.

Die überragenden Eigenschaften von YBCO Bandleitern, besonders bei tiefen Temperaturen von 4.2 K, treiben deren Entwicklung weiter voran. Das obere kritischen Feld von über 100 T der Hochtemperatursupraleiter liegt weit über dem Limit von 23.5 T der "tieftemperatursupraleitenden" Verbindung Nb_3Sn. Ein Meilenstein wurde in den Jahren 2017/18 gesetzt, als ein 32 T Hochfeldmagnet mit einer HTS Innenspule im *National High-Field Magnet Laboratory* (NHFML) in Tallahassee in Betrieb genommen wurde [3]. Außerhalb von Magnetanwendungen werden HTS Leiter in Fehlerstrombegrenzern, supraleitenden Generatoren oder in Stromübertragungsleitungen eingesetzt. Aktuell widmen sich Großprojekte zum Beispiel dem Einsatz von Magnetspulen auf HTS Basis in Kernfusionsreaktoren, wie dem SPARC des *Massachusetts Institute of Technology* (MIT) [4].

Die Qualitätskontrolle der Bänder entlang der gesamten Bandlänge ist eine

notwendige Voraussetzung vor deren Verwendung in technischen Anwendungen. Das lokale Absinken des kritischen Stroms durch Defekte in der Funktionsschicht des Supraleiters können den verlustfreien Stromfluss im gesamten Leiter stark limitieren.

Die Charakterisierung von langen Bändern wird routinemäßig von einem kontaktfreien Hall-array Scanner bei 77 K im Selbstfeld (SF) durchgeführt. Ein typisches Problem bei der vier-Punkt Methode ist die Kontaktierung von rauschfreien dynamischen Kontakten, die das Band mit den Messgeräten verbinden. Die natürliche Ausbildung von Eis auf der Bandoberfläche während dem Charakterisierungsprozess ist ebenso zu berücksichtigen.

Im Zuge dieser Arbeit wurde eine kontinuierliche vier-Punkt Messmethode entwickelt und M-Scan bezeichnet. Das Band wird kontinuierlich von einer Abwickelspule durch ein Bad von Flüssigstickstoff zu einer Aufwickelspule überführt. Innerhalb des Stickstoffbads befindet sich die Messzelle, die sich aus den Kontaktrollen und einem Permanentmagnet mit einer durchgehenden Öffnung, durch die das Band geführt wird, zusammensetzt. Innerhalb des Magneten ist das Band auf einer Strecke von 4 cm einer Flussdichte von 2.61 T ausgesetzt. Die abfallende Spannung entlang des Bandes, welches mit einem zuvor bestimmten Transportstrom belastet wird, wird über die Kontaktrollen kontinuierlich gemessen.

Diese Arbeit setzt sich aus drei Hauptteilen zusammen:

1. Zunächst wird die Entwicklung und der Aufbau des M-Scanners - mit dem Fokus auf den Permanentmagnet, den entwickelten rauscharmen Kontaktrollen sowie der beheizten Gasstrom Banddurchführung (*gas-flow heated feedtrough*), welche die Bildung von Eis unterdrückt, beschrieben.

2. In weiterer Folge wird die Entwicklung des Modells erörtert welches den kritischen Strom aus dem gemessenen Spannungsabfall bestimmt. Dieser Ansatz wurde experimentell mit einem gepulsten 3 T Elektromagnet überprüft.

3. Es folgt die Darstellung der experimentellen Überprüfung der Machbarkeit des M-Scan und weiterführender Analysen der gemessenen I_c Kurven mit dem entwickelten Modell. Der Einfluss von Defekten auf den kritischen Strom wurde untersucht und mit den Resultaten von Hall-array Scans verglichen.

Contents

1

Introduction

Wissenschaft wird von Menschen gemacht.

W. Heisenberg

1.1 The Phenomenon of Superconductivity

Superconductivity is a challenging and highly complex field of solid state physics. Exotic properties like the capability of zero-resistance current transport enable unique technical applications like loss-free power transmission and give opportunities for comparably cheap production of persistent magnetic fields in tens of tesla range. Incredibly sensitive measurement devices to detect tiny variations of magnetic fluxes in the range of $10 \times 10^{-15}\,\mathrm{T\,m^2}$ can also only achieved by using superconducting materials (SQUIDs) [5, 6, 7].

The first discovered superconductor was mercury in 1911 shortly after the liquefaction of helium with the boiling point at ambient pressure at 4.2 K became technologically possible in 1908 [8, 9]. The interest of investigating the ohmic resistance closer and closer to absolute zero for pure materials was huge at this time. Mercury, as it is the liquid metal at room temperature, was comparably easy to clean from impurities and therefore chosen for measurements. Surprisingly, when cooling the sample, its ohmic resistance suddenly dropped to zero at 4 K due to -at this time- unknown reasons [10, 11].

Later on, more and more materials were found to be superconducting and the field of superconductivity started developing. The main obstacle in the beginning was the required access to liquid helium which was only available to a handful researchers.

Nowadays, this needs to be considered as well, as access to low temperatures requires sophisticated machines and very expensive coolants such as helium.

For specific industrial applications, the requirement of low temperatures extremely increases operation costs and therefore superconductors are only used when all other options fail. Reaching higher temperatures to achieve superconducting effects in materials are consequently of great interest as each degree of increased temperature tremendously lowers operational expenses and generally raise chances for establishing further feasible applications.

In 1986 superconductivity was found in a new material class, the cuprates, and shortly after superconductivity with $T_c = 93\,\mathrm{K}$ was found in the Y-Ba-Cu-O compound [2] which is above the boiling point of liquid nitrogen at ambient pressure. This was game-changing, as it potentially highly facilitates access to superconducting properties and massively gained the interest in the development of superconductors for industrial applications [12].

1.2 Type II Superconductivity

The counter-intuitive principles of quantum mechanics are essential in the understanding of key features of superconductivity. Other macroscopic quantum phenomenon in solid state physics like bose-einstein condensation or superfluid liquids like helium II rely on quantum principles as well and are strongly related to superconductivity [13]. The field of superconductors is extremely complex, challenging and still, since its discovery in 1911, far from being well understood.

The great success of the Bardeen-Cooper-Schrieffer (BCS) theory, established in 1957 [14], suggests that the long-range coupling of two electrons are forming a bosonic quasiparticle, called cooper pair, which is crucial for the appearance of superconductivity. In the therein described conventional superconductors, phonons are primarily responsible for a weak but still sufficient electron-electron coupling. For BCS superconductors, a singlet pairing mechanism is considered to form cooper pairs with zero angular momentum and spin quantum numbers ($L = 0$ and $S = 0$), which is in practice usually referred as s-wave pairing state.

The bosonic nature of cooper pairs quantum mechanically allow them to 'condensate' into a common ground state. This condensation has to be understood as a condensation due to statistics and must not be confused with condensation in the common sense which is due to interaction of particles. Such a condensate in its ground state can be described with a macroscopic wave function Ψ that describes all condensed (quasi-

)particles at once. Unlike 'classic' (i.e. atomic) Bose-Einstein condensates, a condensate of cooper pairs in a solid is charged.

The condensation of paired electrons alters the electronic density of states leading to a characteristic gap at the Fermi energy $N(E_\mathrm{F})$ that separates a pool of occupied and unoccupied states. This gap opens below a critical temperature T_c and has a width of $2\Delta(T)$.

In a quantum mechanical description of charged particles the momentum operator $\hat{p} = -i\hbar\nabla$ is extended with an additional term containing a vector potential $\mathbf{A}$ in order to take interaction with electromagnetic fields into account. Therefore, with the charge of a cooper pair $q = -2e$ the momentum operator $\hat{p}$ is replaced by the canonical momentum operator

$$\frac{\hbar}{i}\nabla \rightarrow \frac{\hbar}{i}\nabla + 2e\mathbf{A}. \tag{1}$$

Despite the most prominent and well known effect of zero resistance below a certain material dependent critical temperature T_c, the complete expulsion of a magnetic field in the interior of a bulk superconductor, also known as the Meissner-effect [15], is seen as the key feature that defines a material to be superconducting. Both effects, zero resistivity and the Meissner-effect, are essential to understand superconductivity as a thermodynamic phase and the transition from normal conducting state into superconducting state as a thermodynamic phase transition.

From the very first powerful phenomenological description of superconductors, the London model [16], one key parameter of superconductors can be derived:

$$\Delta\mathbf{B} = -\frac{1}{\lambda^2}\mathbf{B} \tag{2}$$

In general, the solution of a differential equation of the given type in equation (2) is exponentially decaying, in this case with a length-corresponding characteristic parameter λ. It follows that despite the complete expulsion of any magnetic field inside a solid in the Meissner-state, an external field still penetrates at its surface with exponentially decaying flux density towards its center.

A generalization of the London model, as it was done by Pippard in 1953 [17], allows the derivation of a second, evenly important key parameter of superconductors. By relating the current at a specific location $\mathbf{j}(\mathbf{r})$ to the vector potential $\mathbf{A}(\mathbf{r}')$ in the surroundings, the characteristic length ξ, called coherence length, appears. This parameter ξ can be intuitively understood as the minimum length of the macroscopic wave function Ψ at which its properties can be changed.

Both quantities, λ and ξ, can be calculated from the Ginzburg-Landau (GL) theory as well [18]. Although it is apparent, the fathers of the GL theory only focused on the description of materials with a small values of the ratio $\kappa = \frac{\lambda}{\xi}$, in particular $\kappa < \frac{1}{\sqrt{2}}$ [19].

In 1957, Abrikosov introduced a theoretical concept of a 'second group' of superconductors that have *negative* surface energy, i.e. $\kappa > \frac{1}{\sqrt{2}}$, at their superconducting phase border [20, 21]. These type II superconductors prefer the entrance of quantified magnetic flux lines above a lower critical field H_{c1} in a periodic *vortex lattice* [22, 23].

It turned out that most superconducting materials except pure elements and very few compounds (one example is $TaSi_2$ [24]) are of type II and therefore allow flux lines to enter the material for an external field $H_{c1} < H < H_{c2}$. Below H_{c1} type II superconductors are in the Meissner-state and above H_{c2} superconductivity collapses. In between, called the mixed, vortex state or Shubnikov phase, the material is still superconducting and doesn't produce electric field when a current below a threshold I_c is applied. It is remarkable that $\mu_0 H_{c2}$ can be in the range up to hundreds of tesla. This property is relevant for the feasibility of superconductors in technological applications which are therefore unexceptional of type II.

1.3 High-Temperature Superconductivity in Cuprates

The publication of the BCS theory in 1957 provided the first consistent quantum mechanical theory of superconductivity. In contrast to the prior empirical rules to find superconducting compounds with higher and higher T_c [25], the prediction of the critical temperature T_c in this microscopic framework raised new opportunities of thinking [26]. A famous equation for T_c from the BCS theory yields

$$k_B T_c = 1.13 \hbar \omega_D e^{\frac{-1}{N(E_F) V_{e-ph}}}, \tag{3}$$

with k_B being Boltzmann's, $\hbar$ Planck's constant and ω_D the Debye frequency of the solid.

From this point of view one can think of increasing T_c by enhancing the density of states at the Fermi level $N(E_F)$, strengthen the coupling mechanism between electrons described by the electron-phonon coupling parameter V_{e-ph} and/or increasing the maximum frequency in the phonon spectrum, characterized by the pre-exponential factor ω_D [27].

After superconductivity was observed in oxides with T_c's up to 13 K [28, 29], super-

conductivity with higher T_c was suspected in other oxide compounds which was then found in the La–Ba–Cu–O system in 1986 with a remarkably high T_c of 35 K. Mixed valences of Cu^{2+} and Cu^{3+} appearing from the added Ba were considered to enable a strong electron-phonon interaction. The charge carrier density was further tuned to its optimum value by varying the La/Ba ratio [1]. However, from the multi-phase La–Ba–Cu–O starting material, the actual superconducting phase was identified to be $La_{2-x}Ba_xCuO_4$ which exposes a layered perovskite structure and is responsible for the high T_c [30]. Remarkably, the pure parent compound La_2CuO_4 is insulating due to strong electron-electron repulsion [31].

Shortly after, the results of superconductivity in copper oxides were reproduced and enhanced by increasing the chemical pressure within the compound via replacing La with Y which has a smaller ionic radius. This yields a critical temperature of $T_c = 93$ K in the Y–Ba–Cu–O system as reported by Wu in 1987 [2].

Beside the outstanding high T_c, the layered crystal structure and especially the CuO_2 planes are a common feature of the superconducting cuprates. In principle, undoped CuO_2 planes are Mott insulators due to a strong inter-electron repulsion. Charge carriers (electrons or more importantly holes as in the case of $YBa_2Cu_3O_{7-x}$ and most other cuprates) are added from the charge carrier reservoir that sandwiches the practically two dimensional CuO_2 square lattice. These carriers enter a single conduction band in the CuO_2 plane which is created via hybridization between the accidentally degenerated singly occupied $3d_{x^2-y^2}$ orbital of Cu and the $2p_x$ and $2p_y$ orbitals of O. In the undoped CuO_2 plane, electrons are locally bond to the Cu-ions due to their strong repulsion with their spins being antiferromagnetically aligned. The added extra carriers from the surrounding reservoir blocks enable conductivity and superconductivity [32, 33].

Several families of cuprates categorized by the characteristic elements building up the crystal structure were discovered so far. These are the well known rare-earth elements (RE, especially Y), thallium (Tl), bismuth (Bi) or mercury (Hg) based cuprates. All these cuprates exhibit a layered structure with (super-)current carrying CuO_2 planes and their T_c is highly dependent on stochiometric and lattice variations [34].

Experiments revealed the unconventional pairing mechanism of cuprates and strong hints for a singlet d-wave coupling with wave quantum numbers S=0 and L=2 were found. This is related to the strong electron-electron repulsion and despite the lack of common consensus regarding the origin of this pairing mechanism, it seems that d-wave superconductivity is possible in close relation to an antiferromagnetic phase [35, 36].

1.4 Coated Conductors

From thousands of discovered superconducting materials so far, which can be categorized in 32 superconducting materials classes [37], only a small fraction of a few single compounds are suitable to be implemented as a technical superconductor. The critical temperature T_c of the superconducting material generally needs to be $T_c > 4.2\,\mathrm{K}$ and the upper critical field B_{c2} typically greater than 10 T. Additionally, the critical current density of the conductor shall exceed $J_c > 10^4\,\mathrm{A\,cm^{-2}}$ to $10^5\,\mathrm{A\,cm^{-2}}$ and the material must be tolerant to engineering requirements such as mechanical stresses or safety considerations [38]. The high T_c above the boiling point of liquid nitrogen and extraordinary large upper critical field H_{c2} are huge advantages for technical applications of $YBa_2Cu_3O_{7-x}$. Nevertheless, for the production of long-length coated conductors of cuprate superconductors, several issues have to be taken into account.

One of the main obstacles is the short coherence length ξ of a cuprate superconductor which can be calculated from BCS theory as follows

$$\xi = \frac{a\hbar v_F}{k_B T_c}. \tag{4}$$

The parameter a is dimensionless, v_F denotes the Fermi velocity, $\hbar$ Planck's constant divided by 2π and k_B the Boltzmann constant. For high-T_c cuprates, an extremely short coherence length is therefore predicted. Further, in d-wave superconductors ξ is anisotropic ($\xi_\perp \neq \xi_\parallel$). As a consequence, any disturbances of the crystal lattice periodicity will significantly block the current flow [39].

The weak link between high-angle misoriented grain boundaries of polycrystalline samples leads to small inter-grain superconducting coupling and further to disappointingly small critical current densities. Typically, a grain-alignment within a tolerance of 4° misorientation is necessary for strong superconducting coupling [40]. Therefore, biaxially aligned $YBa_2Cu_3O_{7-x}$ crystals are required to achieve sufficiently high critical current densities. This is achieved via biaxially aligned buffer layers on a substrate that serve as pattern on which the HTS material is epitaxially deposited.

1.5 Superconductors in Technology

Up to now, virtually all technologically used superconductors are either the alloy NbTi or the A15 compound Nb_3Sn [41, 42, 43]. These conductors are sometimes referred as LTS (low-temperature superconducting) materials and are generally cooled with liquid

helium down to 4.2 K. Other technologically used superconductors are MgB_2, first generation (1G) high temperature superconductors (HTS) Bi-2212 and Bi-2223 as well as the second generation (2G) HTS conductors YBCO. Additionally, the discovered iron-based superconductors in 2008 are a further promising class of technologically relevant superconductors [44, 45].

This state of the art repertoire of technical superconductors is used in several impacting technical applications [46, 47]. Main advantage is the outstanding performance of superconducting conductors exceeding critical current densities of at least $J_c > 10^4\,\mathrm{A\,cm^{-2}}$ [48] a value that is only hardly reached by conventional conductors [49]. Advantage of such high loss-free current densities is obvious for technologies that require the presence of high magnetic fields of several tesla which cannot be implemented cost-effectively with conventional conductors. Examples are bending magnets in particle accelerators or magnetic resonance imaging (MRI) facilities in medicine. Beside these practical applications, various flagship projects in different research areas are equipped with superconducting technology that further push the limits of research. The following paragraph introduces a few of them.

The most advanced and large-scale projects in the field of nuclear fusion like the tokamaks ITER (France) [50] and JT-60SA (Japan) [51] or the stellarator Wendelstein 7-X (Germany) [52] are using superconducting coils to produce sufficiently strong flux densities to generate the magnetic cage for fusion plasma confinement. At the large hadron collider (LHC) at CERN in Geneva, 1232 NbTi dipole magnets cooled with superfluid helium down to 1.9 K are bending the circulating particle beam in a 8 T field [53]. Additionally, superconductors are not only used in research devices for the academic sector but become more and more interesting for market and public applications as well. This is already the case for previously mentioned commercial MRI medical imaging systems. Another examples are magnetically levitating *Maglev* high-speed trains that operate with a combination of superconducting and permanent magnets and easily achieve traveling velocities of $500\,\mathrm{km\,h^{-1}}$ [54, 55].

However, constraints in a broad replacement of conventional conductors with technical superconductors are coming from an economical point of view. Despite of specific applications that explicitly rely on the outstanding performance of superconductors which justifies the material costs and required cooling mechanisms, for many cases conventional solutions are more practical. The requirement to cool down the superconducting parts in a facility to cryogenic temperatures is a process whose complexity and cost in general correlates with decreasing temperature and increasing mass that needs to be cooled. The high T_c of coated conductors therefore principally provide huge

advantages but their complex manufacturing route is still a cost-intensive process.

Nevertheless, a breakthrough for coated conductors was achieved in 2018 when a 32 T steady state superconducting magnet with HTS inlet coil became operational [56, 3]. Another example of a near-future large-scale project is the SPARC tokamak from the Massachussets Institute of Technology (MIT) where it is planned to produce the magnetic field for plasma confinement with HTS based coils [4].

1.6 Tape Characterization

Characterization of long-length tapes along its length is inevitable before their implementation into a technological application. Important concern of magnet designers is the homogeneity of the critical current along the conductor length which is usually characterized by manufacturers at 77 K in self-field (s.f.) [57]. Testing the I_c homogeneity in field is of importance as well as it has been shown that nominally identical RE123 coated conductors can yield significant deviations when exposed to magnetic fields due to microstructural features [58]. High resolution characterizations of the critical current homogeneity, preferably including the conductor's low temperature and high-field performance is needed.

However, systematic measurements at low temperatures and high fields are sophisticated and the demand of expensive coolants practically disable routine characterization of I_c at 4.2 K, causing that low temperature measurements at high fields are typically done only on short, representative samples. This leads to a lack of consistent quality assessment of continuous performance of the tape along the entire length. Consequently, a reliable method to continuously predict the critical currents at low temperatures and high magnetic fields from measurement at 77 K is ultimately desired.

Quality control of commercially available coated conductors is usually routinely performed by contactless Hall array scan tools such as TapeStar (THEVA) which is operating at 77 K in fields of a few mT [59]. In-field performance of tapes in fields up to 0.53 T in arbitrary orientation are measured in the YateStar device [60, 61, 62, 58].

Another approach of a continuous reel-to-reel characterization tool is reported by Kim et al. [63]. In this approach, the tape is guided through a liquid nitrogen bath. The voltage drop between voltage rollers is kept at a constant value and hence the feedback-adjusted transport current is directly related to the critical current. A further characterization tool for critical current assessment in-field is described by Li et al. in [64].

1.7 Scope of this Work

The main goal of this thesis was the development of a 4-probe reel-to-reel scan tool for critical current assessment of superconducting tapes. The main feature of this machine is a permanent magnet in which a flux density of 2.61 T ($B \perp$ tape surface) is reached in the center of a channel through which the tape is guided. The machine, called M-Scan, was built from scratch and the first part of this thesis is dedicated to its development and assembly. The purpose of this device is to scan tapes with a 4-probe configuration in a bath of liquid nitrogen in a field of 2.61 T. The contacts are provided by rollers that are directly contacted to the tape. During a scan, the device continuously measures the voltage drop due to a pre-selected transport current.

Cryo-measurements with an open liquid nitrogen bath give rise to certain issues that needs to be avoided in order to establish a reliable scan method. These are especially the formation of ice on the tape surface when the tape translates through a zone of cold nitrogen vapor and air above the bath and signal noise mitigation that is generated by moving electrical contacts. To adress these issues, gas flow feedthroughs (GFFs) and dot-like contact (DLC) array rollers were developed. The functionality of the most important components of the M-Scan device are described in the first sections of this work.

Another important chapter of this thesis deals with the current-voltage characteristics in inhomogeneous magnetic fields. Since the tape translates between the voltage contacts through a local magnetic flux zone generated by the 2.61 T permanent magnet, the tape between the voltage contacts is exposed to a magnetic field B with a certain distribution $B = B(x)$. For the assessment of the critical current I_c, a model to evaluate the measured voltage drop along magnetic fields with $B = B(x)$ is required. In this thesis, the electric field and the voltage drop of tapes in inhomogeneous magnetic fields was modeled via the 'Extended Alpha Approximation' (EAA). This approach was experimentally tested on a sample with a 3 T pulsed electromagnet that was developed in the scope of this study.

For the purpose of developing the M-Scan device, experiments have been conducted on different test benches. These experiments were performed in order to characterize the behavior of tapes and applying the results to the development of the M-Scan method.

In the following the test benches used for pre-study experiments are shortly described to give an overview to the reader.

- **Short sample holder.** Short samples with a length of 12 cm are mounted and 4-probe connected on a glass fiber reinforced composite sample holder. In addition,

there is the possibility to apply a set of two stacked miniature permanent magnets with the sample in between. In particular, two different kinds of magnet sets are used with a flux density in the center of either $B_{\max} = 0.57\,\mathrm{T}$ for magnets with rectangular shape and $B_{\max} = 0.53\,\mathrm{T}$ with cylindrical one. Measurements were performed with and without applied magnets.

- **M-Scan.** The development of the M-Scan device is the central aspects of this work. For the first tests of this device, tapes with lengths up to 100 m are scanned. The main feature of the M-Scan is a permanent magnet that provides a flux density of 2.61 T through which the tape is guided. The tape is scanned with a constant transport current and the according voltage signal is tapped by rollers.

- **Gas-Flow Cryostat.** In order to model the voltage drop between voltage contacts of tapes exposed to inhomogeneous fields $B(x)$ a set of samples is characterized in a gas-flow cryostat at 77 K with different homogeneous fields up to 7 T. From the datapoints of the characteristic $I_c - B$ curve, the dependence of $I_c(B)$ is modeled.

- 3 T **Pulsed Electromagnet.** The voltage drop of a sample in an inhomogeneous field is modeled with the EAA approach and experimentally assessed with a developed 3 T pulsed electromagnet. A tape is inserted into the channel between two copper coils. The flux density in a magnet pulse reaches at its maximum $B_{\max} = 3\,\mathrm{T}$ in the center and $B(x)$ decreases towards entrance and exit of the slit. In the pre-study tests with the 3 T pulsed electromagnet experimentally confirmed the reliability of the EAA approach.

Finally, to test the M-Scan method, three different tapes were scanned with the developed device. The tapes investigated exhibit mainly double-disordered tape structure (see section 2.2) but also a tape with standard (i.e. non double-disordered) structure. In complementary tests, the tapes were additionally scanned with a commercial scanning Hall probe device (TapeStar) which is typically used for routine tape characterization.

Based on this initial results, advantages and disadvantages of the developed M-Scan approach are discussed in the end. Topics to further develop this method are highlighted as well.

The end-to-end performance of a tape is lowered by defects that locally degrade the critical current at the defect's position which lowers the limit of current throughput. As a consequence, locally appearing electric fields render currents dissipative and generate

heat. The locally growing temperature increases the risk of a quench which propagation is initiated at the defect's position [65, 66].

In principle, defects can be imprinted at various stages of the production process and are visible or invisible at the tape surface. Therefore, it is necessary to assess the impact of defects on the tape performance and control the quality of the tape. The impact of different kinds of defects on I_c was investigated in several experiments of this work.

2

Tapes and Samples

2.1 Processing Route

The main parts of this work was conducted at Bruker HTS GmbH and therefore the production route of Bruker HTS tapes is shortly outlined in the following. This concerns the key features of the production route of coated conductors with lengths up to 600 m.

- **Alternating Beam Assisted Deposition.** As previously mentioned, biaxially textured substrates are needed for epitaxial growth of second-generation high temperature superconductors. One way is the deposition of a 1 µm to 2 µm thick yttria-stabilized zirconia (YSZ) template buffer layer on typically 0.1 mm thick Cr – Ni stainless steel tapes. This process is called alternating beam assisted deposition (ABAD) [67, 68].

- **Pulsed Laser Deposition.** Fast epitaxial growth of the superconducting layer on the textured substrate is enabled via high-rate pulsed laser deposition (HR-PLD) [69, 70, 71]. Prior to the HTS deposition, a cap layer of CeO_2 on top of the YSZ is added in the PLD processing chamber in order to avoid lattice mismatch between the texture layer and the HTS film [72].

  A schematic view of the PLD reaction chamber is given in figure 2.1. A focused laser beam is scanning the target enabling a fast repetition rate of laser pulses. Target turns prevent inhomogeneous removal of material and maintain deposition quality [73]. Inside the chamber quasi-equilibrium heating stabilizes the substrate temperature [74]. Pulse-like modulation of oxygen pressure in the deposition window create intrinsic disorders (i.e. stacking faults, nano-islands,

nano-precipitates) which serves as additional pinning centers in double-disordered tapes [75].

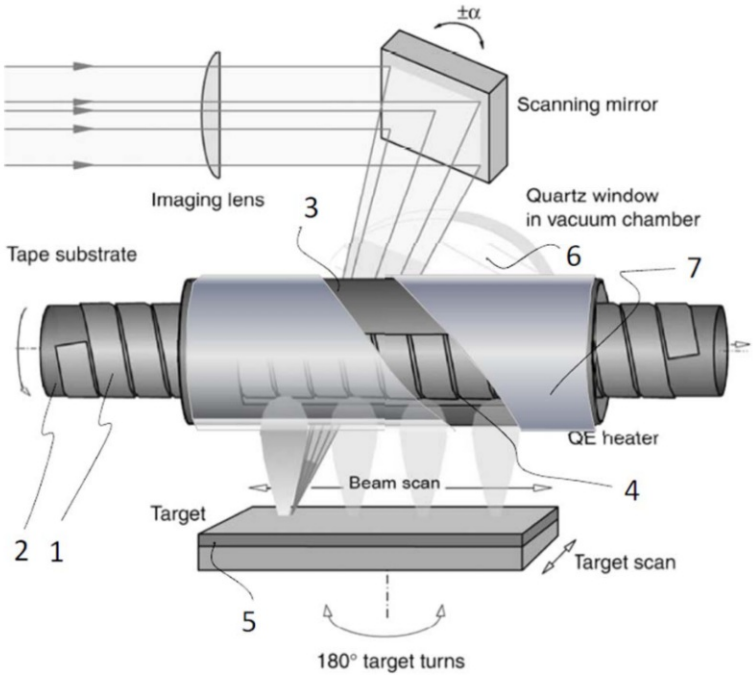

Figure 2.1 – *Scheme of the multi-plume drum based PLD device. The beam scan of a focused laser beam enables fast repetition rates of laser pulses. The figure was provided by courtesy from Alexander Usoskin [70].*

- **Silver and Copper Plating** Doping of the reduced YBa_2CuO_6 compound with oxygen is done after coating the the conductor with a 1 µm thin silver layer. The stabilization of the silver capped coated conductor is achieved by reel-to-reel copper electroplating in a bath of copper sulfate $CuSO_4$ [76, 77, 78]. Finally, the conductor is insulated with a Kapton polyimide tape.

The cross section of the layer structure of the coated conductor is shown in figure 2.2.

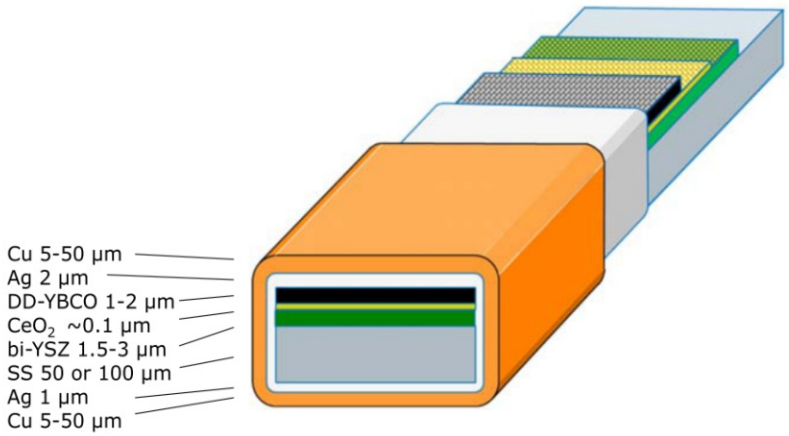

Figure 2.2 – *Schematic view of the layer structure of coated conductors. On a* 50 µm *to* 100 µm *thick stainless-steel substrate a* 1.5 µm *to* 3 µm *thick layer of biaxially textured yttria-stabilized zirconia (YSZ) enables epitaxial growth of the* 1 µm *to* 2 µm *thick YBCO layer. The YSZ layer is previously capped with a* $\sim$ 0.1 µm *thick* CeO_2 *layer. The layered conductor is coated with a silver layer (*1 µm*) and plated with copper (up to* 50 µm*). The figure is taken from [79]*

2.2 Double Disordered Tapes

In tapes employing a double disordered (DD) processing route record critical current values of 309 A in 31 T field ($B \perp$ tape surface) and 4.2 K were observed [75]. These outstanding current values originate from additional pinning centers of intrinsic and extrinsic disorder of the superconducting layer.
The intrinsic disorder is a result of pulse-like oxygen pressure modulation in the PLD process leading to stacking faults, nano-island, nano-precipitates in the HTS layer which serve as pinning centers.

Extrinsic disorder comes from foreign atoms, such as Zr, Ce or Ho that add lattice defects to the structure which are origin to local defects or bamboo-like nanorod structures grow during the deposition process [80].

In comparison to standard (i.e. non double disordered) YBCO tapes, a shift of T_c to lower values in the range of 84 K to 86 K than of the expected 93 K for standard YBCO tapes is observed. Additionally, extra ordinary high ratios between $I_c(4.2\,\mathrm{K}, 18\,\mathrm{T})$ and $I_c(77\,\mathrm{K}$, self-field), in the range of 5-15 are observed [73, 81]. Consequently, critical currents in double disordered tapes at 77 K are lower than those of standard tapes. This is compensated by outstanding critical current densities at low temperature and high-fields as reported by A. Usoskin et al. in [81, 79]

2.3 Tapes and Samples

In the scope of this work, both, short samples with lengths up to 55 cm and tapes up to 100 m have been investigated. In the following tables an overview of investigated samples and tapes is given.

All samples and tapes have a width of 4 mm.

Most of the short samples are cut from a silver coated single tape #T-A which parameters are given in table 2.2. The short samples are listed in table 2.1 and keywords regarding the experiment in which the according sample is measured are noted in the column 'Experiment'. The term 'Zooming effect' and 'Diode effect' will be described in chapter 4.

Sample ID	Length cm	Surface	I_c @ 77 K A	Experiment	Testbench
#S-1	12	Ag	8.5 @1 T	V-I Characteristic	Miniature PM
#S-5	12	Ag	8.5 @1 T	Zooming effect	
#S-6	12	Ag	8.5 @1 T	Diode effect	
#S-7	12	Ag	8.5 @1 T	Diode effect	
#S-2	3	Ag	10 @1 T	EAA modeling	Cryostat
#S-3	3	Ag	10 @1 T	EAA modeling	
#S-4	20	Ag	8.5 @1 T	EAA confirmation	3 T pulsed EM
#S-8	55	Ag	12.5 @1 T	defects in M-Scan	M-Scan
#S-9	3	Cu		T_c measurement	Cryostat

Table 2.1 – *Table of investigated short samples in the scope of development of M-Scan. Most samples, except #S2, #S3 and #S9 are cut from the same tape #T-1 which is described in table 2.2. The critical current of #T-1 is not homogeneously distributed and hence the cut samples have different nominal critical currents. Abbreviations PM and EM refer to permanent magnet and electro magnet, respectively.*

The following table 2.2 lists the tapes scanned in the developed M-Scan device. Tapes with double-disordered structure are indicated with 'DD'. The scan runs are numbered from 1-3 and labeled with a short description. Tapes #T-A, #T-B, #T-C and #T-D are used to cut short samples and, although not scanned in the M-Scanner, listed in the table for the sake of completeness.

Tape ID	scan ID #	Description	tape m	scan m	Surface	YBCO
#T-1	1	implementation of M-Scan	6	2	Cu	DD
#T-2	2	long-length scan	94	80	Cu	DD
#T-3	3	defects	10	10	Laminated	standard
#T-A		Used to cut samples #S1, #S4 - #S8			Ag	DD
#T-B		Used to provide sample #S2			Ag	DD
#T-C		Used to provide sample #S3			Ag	DD
#T-D		Origin of #S9			Cu	DD

Table 2.2 – *Table of tapes investigated. Tapes with double-disordered tape structure are indicated with DD in the 'YBCO'-column.*

3

M-Scan Development

In this section the main components of the developed M-Scanner are described and an overview of the functionality is given. The principle of the machine is as follows: the tape is transported continuously from a take-off reel through the measurement stage to a pick-up reel. In the measurement stage the tape is 4-probe connected with dynamic contacts. Two main features are established in the M-Scan:

1. The tape translates through the channel of a permanent magnet assembly whose magnetic flux desnity reaches 2.61 T in the center.

2. A constant transport current I_{tr} is applied on the tape during the scan and the corresponding voltage drop recorded. This voltage drop is then related to the critical current.

A rough scheme of the the transport scan method is given in figure 3.1 in which these two features are pointed out. The magnetic flux in the center of the magnet is supposed to be $B \sim$2 T to 3 T reducing the critical current ot a level to $I_{\mathrm{c}} \sim$3 A to 5 A.

Beyond the presented very intuitive initial concept, the development and implementation of the M-scan device provides several characteristic features which are described more precisely in the following paragraphs.

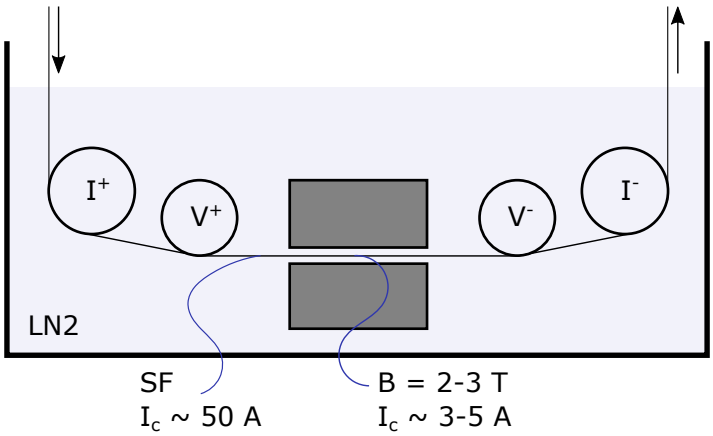

Figure 3.1 – *Rough scheme of the scan transport method. The tape translates through a zone of a flux density of B* ∼2 T *to* 3 T *in which the critical current is reduced to* I_c ∼3 A *to* 5 A*. The tape is 4-probe connected with current and voltage rollers.*

As already described above, it follows from the implementation of a magnetic flux zone provided by a 2.61 T permanent magnet in the center of the measurement stage that the critical current is significantly reduced by ∼80 % to 90 % in comparison to the critical current in self-field. In the case of double-disordered HTS tapes, which are optimized for high in-field I_c performance at low temperatures, extremely high ratios (up to 15) between in-field measurements of I_c(4.2 K, 18 T) and I_c(77 K in self-field) are observed [75, 81]. In comparison to 'standard' (i.e. non double-disordered) tapes, the values of I_c at 77 K are therefore comparably low. This leads to a level of the critical current in M-scans at 77 K in 2.61 T fields of 3 A to 6 A. In tape scans with standard tapes, critical currents up to 18 A were observed.

Working with such moderate transport currents (which are pre-selected to be slightly above the critical current) naturally mitigates the risk of tape damage due to a quench event while scanning. From quick estimations (as it is done later in table 5.2 in section 5.3), it follows that the generated power density in case of quench is below ∼20 mW cm^{-2} which is easily removed by the surrounding coolant.

The voltage drops mainly along the zone that is exposed to the magnetic field (i.e. inside the magnet). This follows from the previously mentioned drastic reduction of the critical current since the voltage response of a transport current representing only a fraction of the critical current outside the magnetic field zone can be practically neglected. However, this might be not true, when a severe defect degrades the critical current already by more than 80 %.

Placement of the tape carrying coils outside the bath of liquid nitrogen allows a

rather easy interchange of tapes since the system doesn't need to be heated. The main challenges to establish the continuous reel-to-reel scan system in the presented design and characteristic features of the developed M-scan are summarized in the enumeration below.

In principle, four main difficulties were solved during the development of the M-scan device, listed as follows:

1. A magnet providing a flux density between 2 T to 3 T needs to be designed and implemented into the measurement stage of the M-Scanner. This was established by the 2.61 T permanent magnet which is described in section 3.2.

2. Development of a model to calculate the critical current I_c from a continuous voltage measurement with constant transport current in a setup where a local flux zone is applied.

3. Providing sufficiently good electric contacts to mitigate noise in nV range from measurements on moving tapes.

4. A solution to the issue of ice formation on the tape surface preventing good electric contacts needs to be implemented. Naturally ice forms on the tape surface when the tape is translating through the nitrogen/air vapor above an open vessel of liquid nitrogen.

3.1 Concept

In general, the M-Scan device consists of two major parts, an outer tape carrying transport system and the inner measurement cell where the tape is measured. The outer structure and concept of the scanner are described in this section. Main components (2.61 T permanent magnet, dot-array rollers and gasflow feedthroughs) of the measurement cell are described in separate sections.

The outer tape transport system consists of two programmable motors that were programmed to provide different tape translation velocities in the range from 1 mm s^{-1} to 15 mm s^{-1}. Measurement stage, motors and tape guiding rollers are fixed on customary aluminum construction profiles. A comprehensive scheme of the M-scan system is shown in figure 3.2 and described in the following.

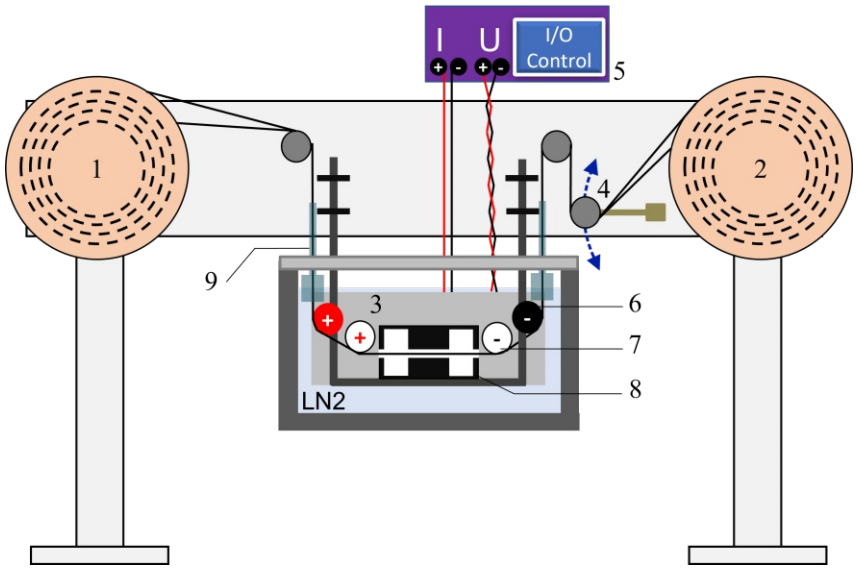

Figure 3.2 – *Scheme of the developed M-Scan. The tape is translated from a take-off reel (1) through the measurement stage (3) to a pick-up reel (2). Constant tape tension is provided by a 'dancer' (4) which is a ballasted roller on a movable axis. Voltage signals and transport currents are controlled with input/output devices (5). The tape is 4-probe connected with rollers acting as current (6) and voltage (7) contacts. Between the contacts, the* 2.61 T *permanent magnet (8) is placed. Gasflow feedthroughs (GFFs) (9) prevent ice formation on the tape which would form an insulating layer suppressing electric contacts between rollers and tape.*

The tape is mounted on a take-off reel (1) and guided via rollers through the measurement stage (3). In the M-Scan assembly the measurement stage is hung up on two stainless-steel rods in order to minimize the heat introduction into the liquid nitrogen bath by the comparably low thermal conductivity of stainless steel.

The tape is wound on a pick-up reel (2) on the other side. The measurement stage is fully immersed in an air-tightened bath of liquid nitrogen during operation. The consumption of liquid nitrogen is determined to be in the range of $1\,\mathrm{L\,h^{-1}}$ to $1.5\,\mathrm{L\,h^{-1}}$. During the scan procedure a constant tape tension from 12 N to 20 N is applied which is provided by a ballasted roller mounted on a movable lever, called 'dancer' (4). The voltage signals and the applied transport current are applied and processed by input/output devices (5). Small fluctuation of the resistance at the rotating dynamic current contacts are automatically balanced within 2 ms by the fast reacting digital power supply which is operated in current control mode. In comparison, the voltmeter takes 2-3 samples per second in high-resolution mode which is 2 orders of magnitude slower than the current balancing operation by the power supply.

In the scheme, the current rollers are depicted as (6) and voltage rollers as (7). The

current roller consist of stainless steel and the current is injected via the axis around which the roller is gliding. The distance between the voltage rollers is Δx_{d}=19 cm and their concept is described comprehensively in section 3.3.

However, the current flowing through the current circuit is additionally checked and recorded by the voltage drop along a calibrated ohmic resistor which is placed in series of the circuit. This resistor consists of a copper wire and is placed in a small vessel of liquid nitrogen to minimize temperature effects. It was previously tested, that this current control resistor is operating stable for applied transport currents up to 19 A. Therefore, for the scans in this study, the current limit through the circuit is set to 19 A, which is nevertheless sufficient for scanning the selected tapes in this work.

The 2.61 T permanent magnet (8) is placed centered within the measurement stage and is described in detail in section 3.2. The tape translates through gasflow feedthroughs (9) to prevent the natural formation of insulating ice at the intersection of liquid nitrogen and air/nitrogen vapor. This relevant component is described in section 3.4. Typically, the tape is moving from (1) to (2) but it can be operated in both directions.

A photograph of the measurement stage is shown in figure 3.3.

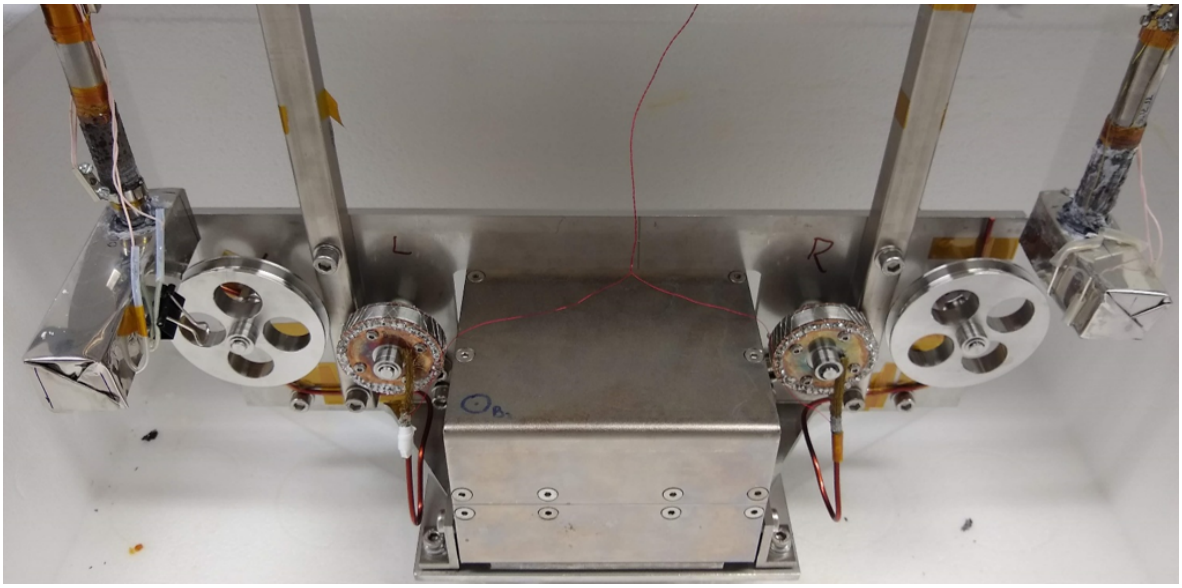

Figure 3.3 – *Picture of the measurement stage showing the main components (gas flow heated feedthroughs, current rollers, dot array voltage rollers and permanent magnet). The tape is entering the stage from the upper left corner and leaving in the upper right corner. The twisted cable for voltage measurement can be seen centrally whereas current cables are hidden behind the rectangular stainless-steel rods on which the assembly is hanged.*

The components are mounted on a stainless-steel structure which is fixed on two rectangular steel tubes and fully immersed in liquid nitrogen during operation. In the 4-probe configuration, the outer stainless-steel rollers act as current contacts and the inner ones as voltage contacts. These developed dot-like contact array (DLC-array) rollers will be described in section 3.3. Brass brushes are fixed on the copper discs of the voltage rollers and tap the voltage signal which is transferred to an electronic device via twisted cables. The cubic shape of the 2.61 T permanent magnet is visible in the center of the measurement stage through which the tape is guided.

3.2 2.61 T Permanent Magnet

In the scope of this work, high-field permanent magnets (PMs) of different materials have been used to create magnetic fields for tape characterization. Miniature permanent magnets are used to characterize short samples in magnetic field and the 2.61 T permanent magnet assembly with a Halbach-array like configuration is placed in the center of the M-Scan. Since permanent magnets therefore play an important role in this work, a rough introduction to high-field permanent magnets (especially rare-earth permanent magnets) is given in the following.

3.2.1 Introduction to High-Field Permanent Magnets

Each material shows a specific behavior when exposed to an external magnetic field H_{ext}. When a material tend to repel H_{ext} from its inside, it is called diamagnetic.
A paramagnetic material posses unpaired electrons in one of each atom's orbitals, in which its z-component of the spin is therefore not determined by Pauli's exclusion principle. The unpaired electron creates a permanent magnetic moment. When exposed to an external magnetic field, the moment of all unpaired electrons tend to orientate in direction of the field H_{ext}, thus reinforcing it. After switching off H_{ext} the macroscopically directed moments dissipate and a favored direction of the moments cannot be observed. Both effects, *diamagnetism* and *paramagnetism* are weak compared to *ferromagnetism* in which a long range interaction couples the magnetic moments.

Due to this interaction, the moments are aligned in domains in order to maintain a lower energy level. The moments will orient parallel in direction of an increasing external magnetic field until saturation of the magnetization is reached. Since the moments keep their direction when the external field is switched off, the material remains magnetized and creates a persistent magnetic field. This residual magnetization

is called remanescence B_r and makes ferromagnetic materials responsible to be used in commercially available permanent magnets.

When an external field is applied in opposite direction of its magnetization, the ferromagnet tend to demagnetize. However, the ability to withstand demagnetization is characterized by the coercitivity H_c. Its value allows classification of ferromagnets in 'magnetically soft' and 'magnetically hard' materials, for a low and high coercivity respectively.

Above all, the ferromagnetic properties are lost due to thermal motion above the material dependent Curie-Temperature T_C. The directed orientation of the magnetic moments breaks up and the permanent magnet has to be magnetized again, which sets T_C as intrinsic limit for industrial application of permanent magnets.

For high-field permanent magnets, high values of both, the remanence B_r and the coercitivity H_c are desired. This is achieved in magnets that include elements of the rare-earths, especially samarium (Sm) and neodymium (Nd). One key feature of magnet relevant rare-earth elements are unpaired and well protected magnetic moments within the internal f orbitals. The unpaired electrons lead to paramagnetism and also for some elements to ferromagnetism at comparably low temperatures. However, alloying rare-earths elements with a transition metal such as Co in the case of Sm or Fe in the case of Nd (with addition of boron (B)) creates the strongest permanent magnets. Both situations are shortly described in the following.

- **NdBFe** Magnets with the structure $Nd_2Fe_{14}B$ were developed independently and simultaneously by *Sumitomo Specail Materials Co.* and *General Motors GM* in 1984 [82, 83]. Neodymium magnets are known to have a typical residual field $B_r = 1.3\,\mathrm{T}$. The very high coercivity $H_c = 1.2\,\mathrm{T}$ to $1.3\,\mathrm{T}$ enables a high resistance against demagnetization. Disadvantages are their comparably low Curie Temperature T_C about $500\,\mathrm{K}$ to $600\,\mathrm{K}$ as well as their brittleness and higher vulnerability to oxidation than Samarium-Cobalt magnets [84, 85].

- **SmCo** The residual field of samarium-cobalt magnets is about 10 % lower than B_r of neodymium magnets. There are two possible configurations, namely $SmCo_5$ and Sm_2Co_{17}. The Curie-Temperature is higher in comparison to neodymium magnets [84, 85, 86].

To give an overview, some key values of the high field permanent magnets are shown in table 3.1. These values serve as references and are further tuned depending on the specific magnet application. This is shown for example for the N48H grade of neodymium based magnets, which is used for the 2.61 T permanent magnet. Databases

of technical specifications for magnet materials are openly accessible from commercial magnet merchants.

Material	B_r [T]	$\mu_0 H_\mathrm{c}$ [T]	T_C [K]
AlNiCo	1.35	0.07	1020
$SmCo_5$	1	0.83	1000
Sm_2Co_{17}	1.15	0.6	880
$Nd_2Fe_{14}B$	1.2	1.2	580
N48H	1.36 - 1.42	1.27 - 1.36	310

Table 3.1 – *Typical properties of rare-earth magnets and the magnetically soft AlNiCo alloy. The remanence and coercivity are described in tesla by B_r and $\mu_0 H_c$, respectively. Additionally, the Curie-Temperature is given by T_C. The materials can be categorized into magnetically soft (AlNiCo) and magnetically hard (others). The reference values are taken from [85] and for the N48H material from datasheets of commercial magnet merchants, eg. [87, 88, 89].*

3.2.2 Halbach Array

In 1973 John C. Mallinson theoretically found a special arrangement of permanent magnets that let all the flux escape from one side of a magnetic structure while none flux is leaving the other side [90]. Thereby the flux density is increased on the one side, whereas it is reduced on the other side. This is schematically and qualitatively shown in figure 3.4 and figure 3.5 where an assembly of five sintered NdFeB (type N48 - similar remanence B_r but lower coercitivity H_c, when compared to type N48H) magnets are simulated with the FEMM (Finite Element Method Magnetics) code package. An introduction to this code package is given in [91]. Figure 3.4 shows the configuration with parallel magnetization direction for each magnet segment. With the Halbach array like configuration, a flux density of $\sim 0.8\,\mathrm{T}$ is reached on the high-field side in the configuration shown in figure 3.5.

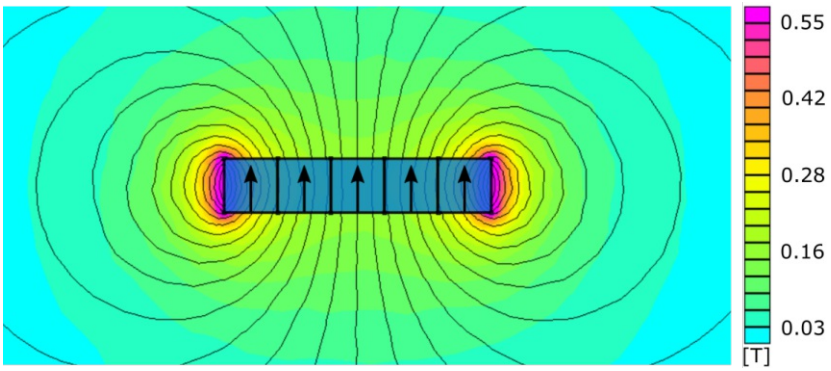

Figure 3.4 – *Flux density of five elements of N48 NdFeB magnets with parallel magnetization direction. The magnet configuration is calculated with the FEMM (Finite Elemente Method Magnetics) code package, available at www.femm.info (accessed in May 2021).*

In figure 3.5 the magnet segments are rotated and hence the magnetization of each segment is pointing in different directions. In the simulated configuration, the magnetic flux is concentrated to one side.

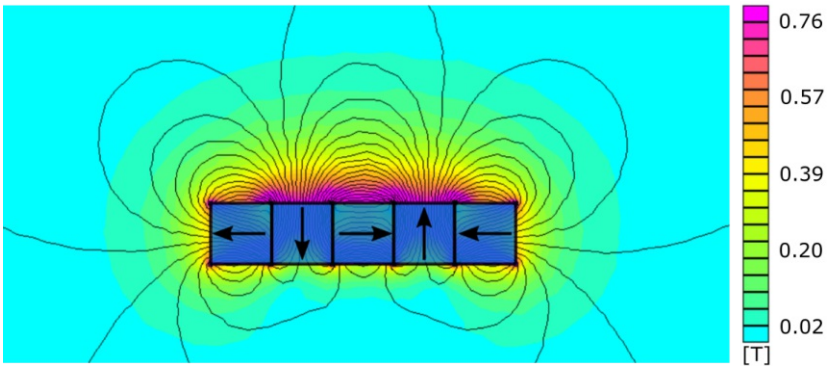

Figure 3.5 – *Halbach-array like configuration of the five magnet segments, calculated with the FEMM code package. The magnetization of each element is pointing in different direction and the flux density concentration to one side of the assembly is clearly visible. The simulated concentration of the flux density reaches* $\sim 0.8\,\mathrm{T}$. *Demagnetization due to the geometry of the configuration has to be taken into account.*

The same properties were found independently from Klaus Halbach who proposed a 16-piece quadrupole magnet in 1980 at the Lawrence Berkeley National Laboratory [92]. In the aperture of his rare earth cobalt magnet (REC-magnet) he could reach an aperture field of 1.34 T. However, with specially designed Halbach-array like configurations magnet, a flux density up to 4 T in the aperture of a magnet assembly can be achieved [86, 93]. The permanent magnet used in this work reaches 2.61 T (at 77 K) in

the aperture and is described in the following sections.

3.2.3 Assembly of the 2.61 T Permanent Magnet

The permanent magnet consists of two sets of four magnet segments of NdFeB (N48H) material with a remanence of $B_r = 1.39\,\mathrm{T}$. The magnetized segments are fixed in a stainless-steel chassis with specific orientation of each segment's magnetization to achieve a flux density concentration towards the center as described in previous sections. The components are fixed mechanically and no glue is used. There is an air gap between the two sets of the four magnet segments which has a cross section of $2 \times 20\,\mathrm{mm}^2$. The maximum flux density in the channel reaches $B_{max} = 2.54\,\mathrm{T}$ at room temperature ($T = 293\,\mathrm{K}$) and $B_{max} = 2.61\,\mathrm{T}$ at 77 K. A surrounding iron housing shields the stray fields except at a small region at the openings to a level below 0.5 mT, which is regarded as safety standard with respect to cardiac pacemakers [94, 95]. The total outer dimensions of the assembly are $130 \times 128 \times 88\,\mathrm{mm}^3$ and it weights 7 kg. The magnet was assembled and delivered by the *Bruker BioSpin GmbH*, located in 34 Rue de l'Industrie, 67160 Wissembourg, France. A picture of the permanent magnet assembly is shown in figure 3.6.

Figure 3.6 – *Picture of permanent magnet assembly. The magnetized NdFeB segments are surrounded by an iron housing. The entrance of the slit for tape throughput is visible. Courtesy by Bruker BioSpin.*

Within the channel, the the field lines are perpendicular to the tape and the channel, i.e. $B = B_z$ and in the central zone B_z is homogeneous within a precision of $\sim 1\,\%$.

The flux density distribution along the channel $B(x)$ will be discussed in section 3.2.4.

The mechanical stability of the structure and the persistence of the magnetic field was extensively tested by repeated cooling cycles where the complete magnet assembly was cooled down to 77 K in a bath of liquid nitrogen and thawed up to room temperature in an airtight box. This procedure was performed ten times and during each cooling cycle a cryogenic InAs Hall sensor was placed in the center of the magnet channel and the flux density recorded. When the magnet is fully cooled down, the flux density reaches 2.61 T in the center.

3.2.4 Flux Density Distribution of the 2.61 T Permanent Magnet

The flux density distribution $B(x)$ along the channel is shown in figure 3.7 before the first and after the tenth cooling cycle, which is denoted as $B_0(x)$ and $B_{10}(x)$, respectively. For the measurement of the distribution the Hall sensor is fixed on a plastic reinforced holder and stepwise introduced in the channel. This Hall scan is done at room temperature and matched to the flux density values at 77 K in the center of the magnet.

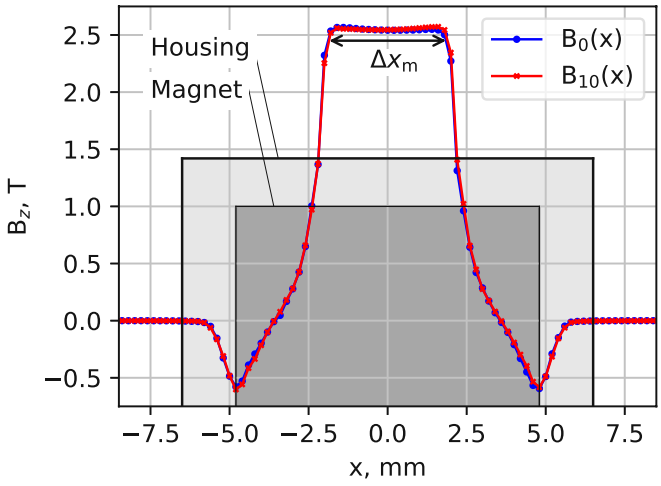

Figure 3.7 – *Flux density distribution along the channel of 2.61 T permanent magnet. The dimensions of the housing and the magnet structure are depicted schematically as grey areas. There is a* 4 cm *long homogeneous 'plateau'* Δx_m *from* $x = -2$ cm *to* 2 cm *with a flux density of* 2.61 T *in the center of the magnet. Out of* Δx_m*, the flux density rapidly drops and reverses at* $x = \pm 3.5$ cm*. The minimum field* $B_\mathrm{min} = -0.58$ T *is reached at* $x = \pm 4.8$ cm*.*

In figure 3.7, the housing and the inner structure of the magnet are introduced

schematically as grey areas. From comparison of the flux density distribution $B_0(x)$ and $B_{10}(x)$ it is considered that the mechanical structure and the flux density distribution in the magnet channel are sufficiently stable with respect to the repeated cooling cycles. The maximum magnetic field of $B_{\max} = 2.61\,\mathrm{T}$ at 77 K is reached within a homogeneous flux zone. In the following, this effective length is also named 'plateau-zone' and defined to reach from Δx_{m}=−2.0 cm to 2.0 cm. Out of Δx_{m}, the flux density significantly reduces and reverses at $x = \pm 3.5\,\mathrm{cm}$. The minimal value of the field $B_{\min} = -0.58\,\mathrm{T}$ is found at $x = \pm 4.8\,\mathrm{cm}$. At the opening of the housing at $x = \pm 6.5\,\mathrm{cm}$, the flux density is $-2.5\,\mathrm{mT}$. The safety threshold of 0.5 mT is reached at a distance of $\sim 8\,\mathrm{cm}$ from the center i.e. 1.5 cm from the opening of the housing.

The 40 mm long 'plateau'-zone of the flux density distribution is causing the overwhelming part of the voltage drop of current loaded tapes during their scan procedure. This means, that the tapes are scanned with a spatial resolution of 40 mm.

3.3 Dot-Like Contact Array Rollers

Providing 'dynamic' electric contacts of a four probe technique on translating tapes is one of the main issues at the development of the M-Scan. It turns out that naturally self-formed oxides on copper plated tapes mitigates the electrical conductivity and prevent tapes from being sufficiently conductive. This is similar as well for silver coated tapes since their surface tends to form silver sulfide Ag_2S which also has a rather limited conductivity [96, 97].

The challenge is to achieve practically noise-free signals for voltage and current measurements in the range of µV and µA on translating tapes. This can be achieved by sufficiently high pressure penetrating through these thin insulating layers [98]. A concept that solves that problem is described in the following.

The voltage is taken from rollers around which the tape is guided during its translation. In the M-Scan setup, the tension of the tape shall not exceed a tensile force of 20 N, which is considered to be a typical value of the tensile force of windings in tape carrying coils [72]. At the contacting zones between roller and tape, a contact pressure on the roller is created. This is shown schematically in figure 3.8.

The pressure between the tape on the roller is estimated from the relation for the pressure

$$p = \frac{|\mathbf{F}|}{\mathrm{A}}. \tag{5}$$

The force employed in equation 5 and further an expression for the pressure is derived

in the following.

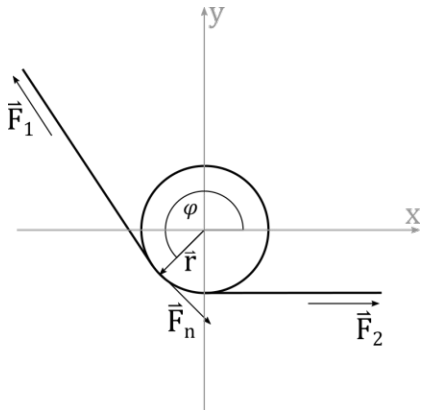

Figure 3.8 – *Scheme of a tape guided by a roller. Forces on both ends of the tape impose a tension on the tape. The tape is deflected on the roller and forces between roller and tape are exchanged. These creates a pressure p between roller and tape which is estimated in the following to be $p = \frac{1}{wR}F$, where w is the width of the tape, the value of the radius is given by R and $|\vec{F_1}| = |\vec{F_2}| = F$*

For this estimation, no deformation of the tape, roller and no friction are assumed. The force at the position $\mathbf{r} = R \cdot \hat{\mathbf{r}}$ is then given by $\mathbf{F}_\mathrm{n}$, where $\mathbf{F}_\mathrm{n} = \mathrm{F}(-\sin\varphi, \cos\varphi)^\mathrm{T}$ and $|\mathbf{F_1}| = |\mathbf{F_2}| = \mathrm{F}$. The value of the radius of the roller is given by R and the radial direction by $\hat{\mathbf{r}}$.

To estimate the pressure, an expression for the force from the tape to the roller, hence the component of $\mathbf{F}_\mathrm{n}$ in direction of $\hat{\mathbf{r}}$ is needed. The component of the force $\mathbf{F}_\mathrm{n}$ in radial direction becomes only non-zero when an infinitesimal deviation of $\mathbf{F}_\mathrm{n}$ is considered. Since the force $\mathbf{F}_\mathrm{n}$ denotes the force at the position $\mathbf{r}$, the radial component of the force can generally be written as $\mathrm{d}\mathbf{F} \cdot \hat{\mathbf{r}}$.

In principle, the total force $\mathbf{F}_\mathrm{tot}$ from the tape to the roller is given by integration of all infinitesimal forces $\mathrm{d}\mathbf{F} = \mathrm{F} \cdot \hat{\mathbf{r}} \cdot \mathrm{d}\varphi$ along $\Delta\varphi$, where $\Delta\varphi$ contains the angles between which the tape is touching the roller.

Additionally, the area A that the tape covers on the roller is given by $\mathrm{A} = w \cdot |\mathrm{d}\mathbf{r}| = wR \cdot \mathrm{d}\varphi$, with w being the width of the tape.
The pressure between the tape and the roller can therefore be written as

$$p = \frac{\mathrm{F}}{A} \rightarrow \frac{|\mathrm{d}\mathbf{F} \cdot \hat{\mathbf{r}}|}{w \cdot |\mathrm{d}\mathbf{r}|} = \frac{|\mathrm{F} \cdot \hat{\mathbf{r}} \cdot \mathrm{d}\varphi \cdot \hat{\mathbf{r}}|}{wR \cdot \mathrm{d}\varphi} = \frac{\mathrm{F} \cdot \mathrm{d}\varphi}{wR \cdot \mathrm{d}\varphi}. \tag{6}$$

This leads to the expression

$$p = \frac{1}{wR}\mathrm{F}. \tag{7}$$

It turned out in the scope of several preliminary tests, that the tensile force of 20 N on a roller with 46 mm diameter and a 4 mm wide tape leads to pressure of $p \sim 0.2$ MPa, which is insufficient for reliable contacts. A much higher contact pressure is needed, however without exceeding the tape damaging threshold of $p_c \sim 360$ MPa [72].

Finally, a dynamic contact roller was developed and implemented to the M-Scan that exhibits a dot-like contact array (DLC-array). The underlying idea of this concept is the reduction of the contacting area yielding significantly higher contact pressures between the tape and the roller in comparison to the bare roller. The cross section of the design is shown in figure 3.9. At both sides of the stainless-steel roller (1) two copper discs (2) are mounted. There are 48 copper pins (3) fixed on each copper disc that simplifies the soldering of a silver coated copper wire (4). Pan head screws (5) are used to fix the discs on the stainless steel roller. The diameter of the roller is 46 mm and the total height of the cylinder is 10 mm.

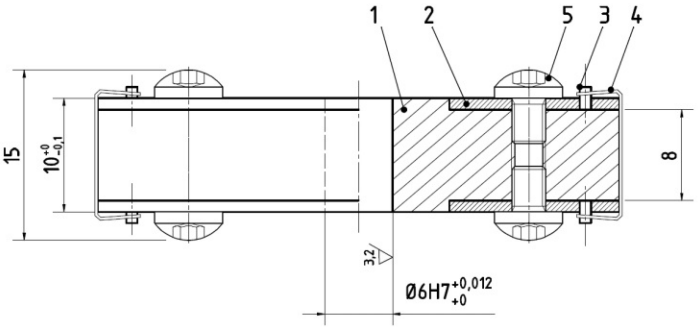

Figure 3.9 – *Cross-sectional drawing of the dot-like contact array roller. Two copper discs are mounted on the stainless steel roller (1). Several cooper pins (3), mounted on a copper disc (2), simplify the soldering of a silver coated copper wire (4). Pan head screws (5) are used to fix the copper disc on the stainless steel roller. The total height of the cylinder is* 10 mm *and the diameter is* 46 mm. *Details on this concept were developed together with my supervisor Dr. Alexander Usoskin.*

From the tested arrangements of the silver coated copper wire, the 'criss-cross' configuration, as shown in figure 3.10, turned out to be the most reliable concept to achieve a noise-free signal. With the given diameter of the thin silver coated copper wire, $d = 0.07$ mm, the pressure at the contact dots is estimated using equation 7. Assuming, that the tape during its translation is directly connected to one silver coated copper wire at once, the pressure is estimated to be $p \sim 130$ MPa.

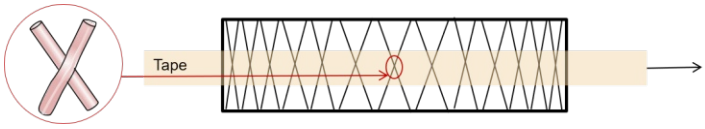

Figure 3.10 – *'criss-cross'-configuration of the silver coated copper wire. The pressure at the intersection between tape and roller within the red circle is estimated to be* $p \sim 130\,\mathrm{MPa}$.

All Ag-coated copper wires are connected to each other and hence having the copper discs on each roller being on the same potential. This potential is tapped by gliding brass brushes on each roller that are directly connected to the voltmeter. A picture of on of the implemented rollers is shown in figure 3.11.

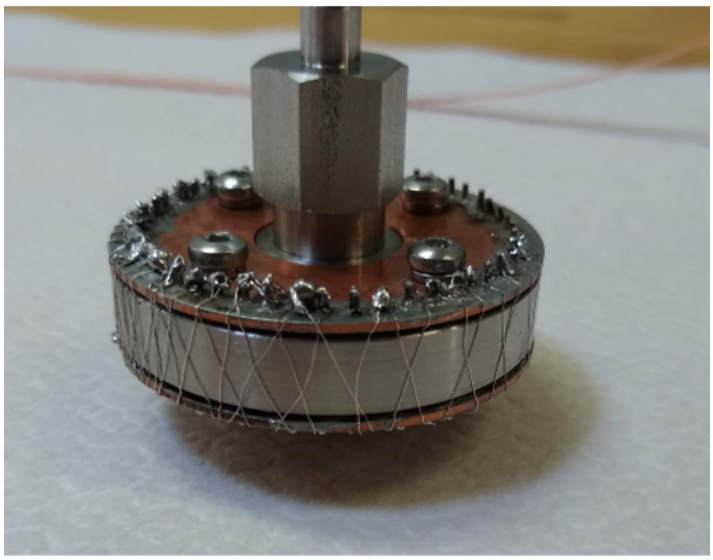

Figure 3.11 – *Picture of the dot-like contact array roller. Thin silver coated copper wires are soldered on copper pins which are fixed on copper discs. The 'criss-cross' configuration, shown here, turned out to be the most favorable.*

The implementation of the roller into the measurement stage is shown in detail in figure 3.12. The gliding brass brush is tapping the voltage from the roller and is directly connected to the voltmeter.

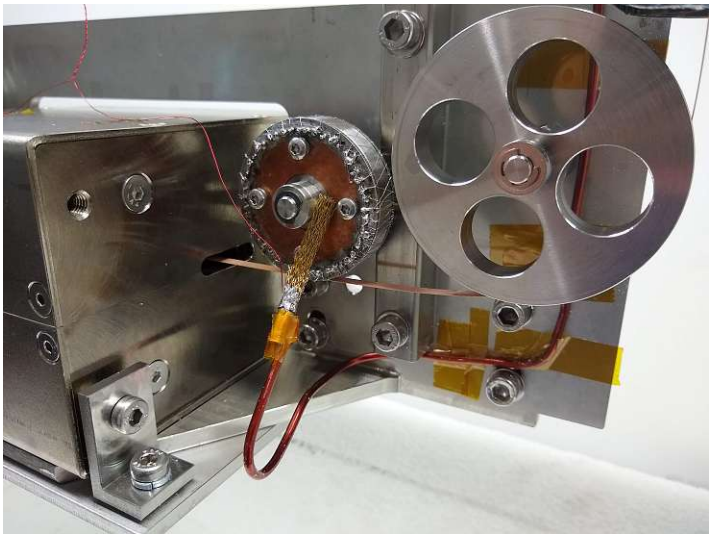

Figure 3.12 – *Implementation of the dot-like contact (DLC) array roller into the measurement stage of the M-Scanner. Both copper discs of the DLC roller are on the same potential, which is tapped by a gliding brass brush.*

3.4 Gasflow Heated Feedthroughs

The natural formation of ice on the tape surface during its translation within a gaseous environment of air and cold nitrogen vapor, which is naturally the case over an open bath of liquid nitrogen, insulates the tape from being electrically conductive. It was tested, that without a solution to the problem of ice formation on the tape surface, dynamic four probe measurements are practically impossible. For reliable scans, a method to prevent ice forming on the tape surface needs to be implemented into the M-Scanner.

The first idea of course is to avoid the tape translating through the open gaseous phase at all, which can be established by keeping reels and the tape altogether in liquid nitrogen.

A second, well established approach is to keep the reels at room temperature and protect the tape from air with an air-tightened cover above the cryostat. This is realized in the TapeStar reel-to-reel measurement tool based on Hall-scan measurements on coated conductors [99, 59].

The issue of ice formation is solved in the M-Scanner with a different approach that is based on local gas-flow feedthroughs for the moving tape. A drawing of the gas-flow feedthrough is shown in figure 3.13.

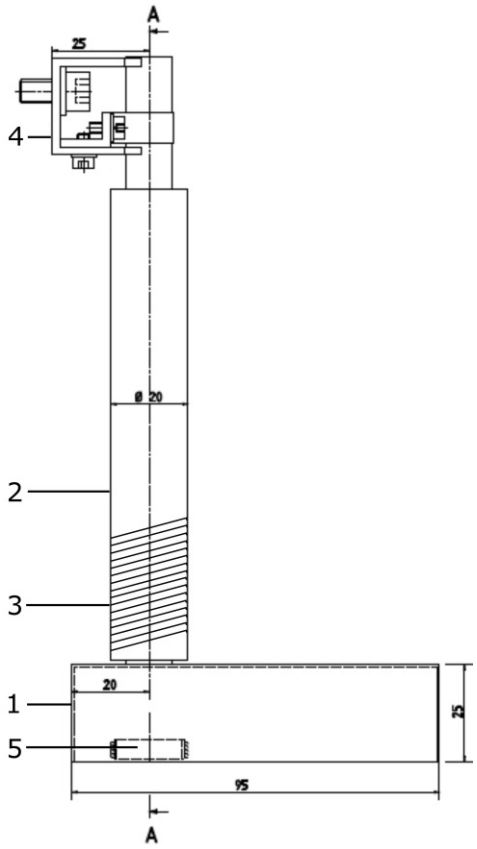

Figure 3.13 – *Drawing of the gas-flow feedthrough. The box in which the nitrogen is evaporated is indicated with (1) and the stainless-steel tube with (2). The nitrogen gas heater is depicted in (3). The gas-flow feedthrough is mounted at the warm end with a double-prism holder (4). Liquid nitrogen is evaporated by a resistive heater (5). The concept was developed together with my supervisor Dr. Alexander Usoskin.*

The tape storing reels are placed at ambient temperature with a tape path translating the tape in vertical direction into the liquid nitrogen bath. The tape is guided through a stainless-steel tube (2) into the nitrogen bath in which a flow of warm nitrogen gas is employed. This is provided by a nitrogen gas heater element (3), that is wrapped around the tube. External power supplies control the current flowing in the heater and therefore the generated heat. In this way, the nitrogen gas is heated to a temperature of 20 °C to 30 °C. The cold end of the tube is, in comparison to the warm end, supposed to be the closer end to the surface of the nitrogen liquid. The nitrogen gas is evaporated via evaporator (5) from the cryo vessel within a small box (1) that is opened at the bottom and tightly connected to the cold end of the tube. A steady flow of nitrogen gas is therefore guided through the tube. The whole assembly is placed outside the LN2 vessel with a double-prism holder (4) that is mounted at the warm end of the tube to

the outer structure of the M-Scan system. However, during operation the level of liquid nitrogen in the vessel should be at the half-height of the box, with the evaporator fully immersed in the liquid nitrogen.

On the tape surface, that is entering the liquid nitrogen vessel in vertical direction through the 'input' GFF, no ice is formed. Vice versa, the tape is heated in a dry nitrogen gas back to room temperature (or slightly above it) in the 'output' GFF, when the tape is leaving the liquid nitrogen. The heating regime of the gas heater is different for 'input' and 'output' GFF. This is especially true when the tape is translated with a speed higher than $10\,\mathrm{mm\,s^{-1}}$. In this regime, the heating power at the 'input' GFF is 10 W to 15 W while the heating power at the 'output' GFF should be increased to 35 W.

The total energy consumption of both GFFs is in the range of 50 W to 60 W from which only a minor fraction of 5 % is dissipated in the liquid nitrogen bath. The nitrogen consumption of the M-Scan vessel was determined to be $1\,\mathrm{L\,h^{-1}}$ to $1.5\,\mathrm{L\,h^{-1}}$. In table 3.2 an overview of calculated parameters and values of the GFFs are listed.

Parameter	Value
Current I @ 45 W	1 A
Heater Power	45 W
LN2 consumption	$1\,\mathrm{L\,h^{-1}}$
	$0.000\,278\,\mathrm{L\,s^{-1}}$
	$0.278\,\mathrm{cm^3\,s^{-1}}$
	$0.194\,\mathrm{g\,s^{-1}}$
N2 gas flow	$0.151\,\mathrm{L\,s^{-1}}$
	$150.7\,\mathrm{cm^3\,s^{-1}}$
Volume tube	$17.0\,\mathrm{cm^3}$
Volume tube/VN2	$8.9\,\mathrm{s^{-1}}$
Target Vtube/VN2	$1\,\mathrm{s^{-1}}$
Ptarget, min	5.1 W
Ptarget, max	10.1 W

Table 3.2 – *Evaluated values of the parameters of the evaporator.*

Finally, a picture of the gas-flow feedthrough is shown in figure 3.14. The previously described elements (1)-(5) are indicated as well as in the drawing of the GFF (figure 3.13). The evaporator (5) is inside the box and not visible in this picture.

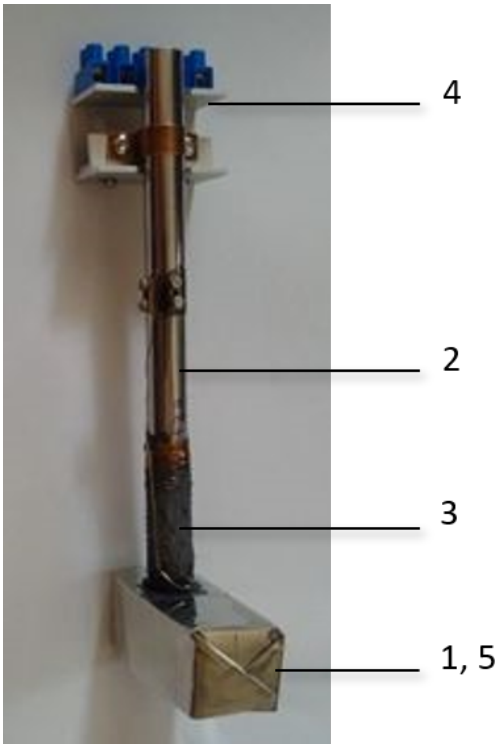

Figure 3.14 – *Picture of the gas-flow feedthrough. The elements stainless-steel box (1), tube (2), heater (3), double-prism holder (4) and evaporator (5) are described as well in figure 3.13.*

3.5 Tape Windings on Coil

A trivial consideration that needs to be treated in long-length scans is the varying effective coil diameter of tape carrying coils during a scan. It is obvious that the stacking of the tape on the coil during the winding process is altering the distance from the coil core from which the tape is taken or on which it is picked up. Therefore the 'effective' radius of the coil is chainging during a scan. Hence, when the tape is driven by the tape carrying coils, a constant translation velocity of the tape through the measurement stage generally requires a separate control the angular velocity of the tape carrying coils.

Since it turned out to be useful in the scope of M-Scan development, an analytic expression to calculate the tape length from its stacking height on the tape carrying coil is derived in the following. This is done by line integration of an archimedian-like spiral that starts from an inner core radius r_0 of the coil. It is parameterized by

modifying a circle that changes its radius r with increasing parameter t.

$$r\begin{pmatrix}\cos(\varphi)\\ \sin(\varphi)\end{pmatrix} \rightarrow r(t)\begin{pmatrix}\cos(t)\\ \sin(t)\end{pmatrix} \tag{8}$$

The tape is wound on a coil with a solid inner core radius r_0 which is, since the tape has a thickness z, increased by z each turn. This can be written as

$$r(t) = r_0 + \frac{t}{2\pi}z. \tag{9}$$

The length of a curve $\gamma(t)$ is calculated via the line integration as follows

$$L(\gamma) = \int_0^{\varphi} \|\dot{\gamma}(t)\| \mathrm{d}t. \tag{10}$$

In this expression, the upper integration limit φ denotes the total angle of which the coil needs to be turned in order to wind a tape with length L. The number of full turns then can be calculated by $N = \frac{\varphi}{2\pi}$.

From the previous parametrization (8) and with the radius $r(t)$ from equation (9) the curve $\gamma(t)$ is immediately written as

$$\gamma(t) = \left(r_0 + \frac{t}{2\pi}z\right)\begin{pmatrix}\cos(t)\\ \sin(t)\end{pmatrix} \tag{11}$$

which leads to the euclidean norm for $\|\dot{\gamma}(t)\|$ as follows

$$\|\dot{\gamma}(t)\| = \sqrt{\frac{z^2}{4\pi^2} + \left(r_0 + \frac{t}{2\pi}z\right)^2}. \tag{12}$$

However, since the constant first term $\frac{z^2}{4\pi^2} \ll 1$ for small z and much smaller than the second term of the sum, the further calculation becomes much easier when it is neglected. The integral (10) becomes then

$$L(\gamma) = L = r_0\varphi + \frac{z}{2\pi}\frac{\varphi^2}{2}. \tag{13}$$

In order to connect the tape length to the number of turns needed to wind it on a tape

with inner core radius r_0, the quadratic equation

$$\frac{z}{4\pi}\varphi^2 + r_0\varphi - L = 0 \tag{14}$$

has to be solved (where only the positive solution is used)

$$\varphi_{1,2} = -\frac{2\pi r_0}{z} \pm \sqrt{\frac{4r_0^2\pi^2}{z^2} + \frac{4\pi L}{z}}. \tag{15}$$

Equation (15) gives a relation between a tape with length L and thickness z that and the turning angle that is needed to wind it on a coil with inner core radius r_0. As mentioned above, this angle can be converted to full turns of the coil via $N = \frac{\varphi}{2\pi}$.

The previously derived set of equations can be used the other way round to estimate the tape length from the height of the tape stack on the coil with core radius r_0. This is done by measuring the height h of the tape stack on the coil and the tape thickness z which allows an estimation of N via $N = \frac{h}{z}$.

N is then implemented in equation (13) via $\varphi = 2\pi N$. This gives the length of the tape, estimated from the number of turns $N = \frac{h}{z}$ via

$$L = \pi\frac{h}{z}(2r_0 + h). \tag{16}$$

The derived equation (16) is an useful tool for a general estimation of the tape length with thickness z from the stacking height h of its windings on a coil with inner core radius r_0.

The initially scan procedure developed in this thesis is based on a constant angular velocity of the driving reels, which hence leads to deviations in the translation velocity when the stacking height on the coils alter during a scan. This error is neglected in the first scans conducted in this thesis.

4

Voltage Response Modeling

In the 4-probe measurement stage of the M-Scanner, the tape travels through the channel of the magnet assembly. Therein, the magnetic flux is focused to a central region exhibiting a homogeneous plateau-like field distribution of 2.61 T at 77 K. This means, that the magnetic field is not homogeneously distributed between both voltage rollers but restricted to a local zone and the tape translates through edge gradients of the magnetic field.

In this section, experiments on short samples are described in order to develop an approach which is called 'Extended Alpha Approximation' (EAA). An overview of the measured samples was previously given in table 2.1.

4.1 Extended Alpha Approximation

4.1.1 V-I Characterization in Assembly with Miniature Permanent Magnets

On short samples the critical current of a superconducting tape is typically evaluated by ramping up a transport current and measuring the characteristic current-voltage curve (V-I characteristic) of the sample. The critical current I_c of the sample is determined when the measured voltage drop U exceeds a critical value V_c. This value is defined by a criterion of an electric field, which is typically set to

$$E_c = \frac{dV_c}{dx} = 1\,\mu V\,cm^{-1}. \tag{17}$$

In a homogeneous field, the critical voltage V_c can be evaluated by knowledge of the distance Δx of the potential contacts. The corresponding critical current I_c follows immediately from the measured V-I characteristic of the sample when the critical voltage V_c is known.

The 4-probe short-sample testbench to evaluate the critical current from V-I characterization at 77 K is shown in figure 4.1. The 12 cm long sample #S-1 was fixed on a glass-fiber reinforced composite holder and the voltage and current contacts were carefully connected with low temperature solder in order to not damage the thin silver coating. An assembly of two stacked miniature SmCo permanent magnets, with dimensions $12 \times 10 \times 5\,\mathrm{mm}^3$ was placed between both potential contacts. The magnets were separated by two pieces of non-magnetic wires parallel to the tape in order to open a slit of 0.67 mm height for sample throughput. In this setup, the potential contacts were separated by $\Delta x = 3$ cm and the V-I curve was taken (a) in self-field (s.f.) i.e. without the magnet assembly and (b) with applied magnets as shown in figure 4.1. After preparation of the sample on the holder and connection of all contacts, the whole setup was immersed in a bath of liquid nitrogen and the V-I characteristics recorded.

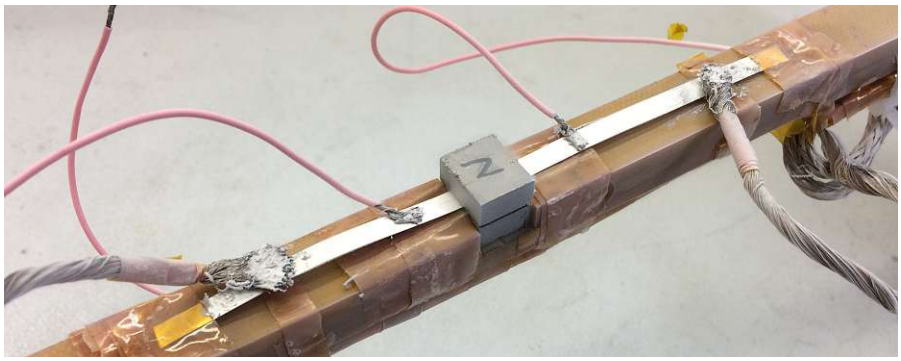

Figure 4.1 – *Testbench of V-I characterization for short samples. A stack of two miniature permanent magnets was placed between the voltage contacts. The contacts were soldered with a low-temperature solder and the voltage contacts separated by $\Delta x = 3$ cm. The whole testbench was immersed in a bath of liquid nitrogen after the sample preparation. Tests were performed with applied magnets and also in self-field. Test with this sample holder are also reported in [100].*

The flux density distribution of the miniature permanent magnet assembly was recorded along the sample by a Hall probe which is shown in figure 4.2. The flux density reaches its maximum $B_{max} = 0.57$ T around the region at $x = 0$ mm which is located in the center of the magnet stack. For the first test in this setup, the measured field distribution was approximated by a rectangular shaped distribution as it is de-

noted as black dashed line. The field is therein at its maximum value $B_{\max} = 0.57\,\mathrm{T}$ from $-5\,\mathrm{mm}$ to $5\,\mathrm{mm}$, which is corresponding to the x-dimension of the magnet stack, and zero elsewhere. It will be shown later in section 6.1.1 that the error due to this approximation is estimated to be in the range of 4-5%.

However, when a drop of voltage is measured by the potential contacts that are separated by $\Delta x = 3\,\mathrm{cm}$, the main contribution of the corresponding electric field is restricted to the zone where the field is applied, hence inside the 1 cm long slit of the magnet assembly.

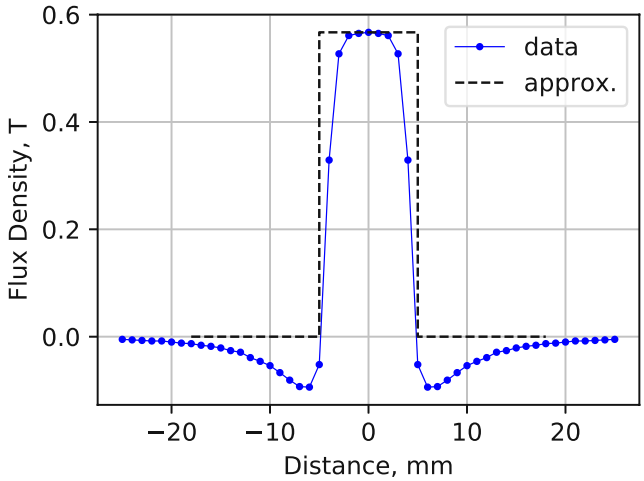

Figure 4.2 – *Flux density distribution of miniature permanent magnets. The maximum field $B_{\max} = 0.57\,\mathrm{T}$ is reached in the center of the magnet stack. The experimental field distribution in initial tests was approximated with a rectangular shaped distribution, which is indicated as dashed line.*

Figure 4.3 shows the V-I curves of the previously shown sample for both cases, (a) in self-field without the magnet assembly with green circles and (b) with applied magnets with red triangles. The critical voltage for each case V_c is denoted by a solid black horizontal line. In case (a) the critical voltage was set to $V_\mathrm{c}^{\mathrm{s.f.}} = 3\,\mu\mathrm{V}$ and for (b) the critical voltage was set to $V_\mathrm{c}^{\mathrm{mag}} = 1\,\mu\mathrm{V}$. The voltage criterion corresponding to the length between the voltage contacts Δx is denoted as *cr-1*. The critical current was then evaluated to $I_\mathrm{c} = 39\,\mathrm{A}$ in self-field and to $I_\mathrm{c} = 11\,\mathrm{A}$ when the stack of permanent magnets was applied. Figure 4.3 shows the measured V-I characteristics which were approximated by a power law with characteristic exponents n according to

$$U = V_\mathrm{c} \left(\frac{I}{I_\mathrm{c}} \right)^n . \tag{18}$$

The values of the exponent n were determined by evaluating the slope of the curves above the according voltage criterion. The n-values of $n = 26$ in self-field and $n = 13$ when the magnets were applied are used in equation (18) to model the measured data. The quality of HTS tapes is related to the exponent n, and therefore the n-value is relevant for tape characterization [62, 101, 102]. However, the n-value and I_c are dependent on the magnetic field.

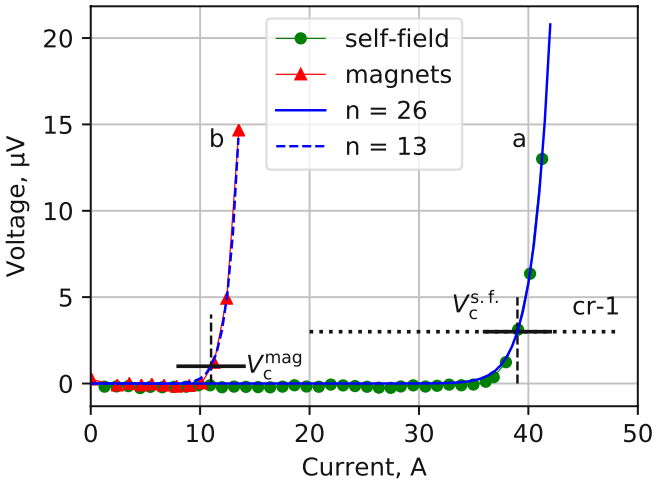

Figure 4.3 – *V-I characteristics of the measured sample. Case (a) denotes the measurement in self-field and (b) when the magnet stack was applied. The different values of V_c are depicted as black horizontal dashed line. Critical currents for case (a) and (b) are found to be $I_c = 39\,A$ and $I_c = 11\,A$, respectively. The according n-values are $n = 26$ in self-field and $n = 13$ when the magnets are applied. A dotted line cr-1 represents the critical voltage between the voltage contacts. The V-I curves are approximated with a power law with indicated numerical exponents and depicted with blue lines (solid, dashed).*

4.1.2 HTS Tape Characterization at 77 K in Magnetic Fields

Earlier attempts of approximations for $I_c(B)$ are not sufficient to be used as 'universal' tool for I_c modeling [103, 104, 105]. In order to search a simplified mathematical description for double disordered technical superconductors, the following approach was chosen. This approach is also reported in [100].

The samples #S-2 and #S-3 were characterized in the gas-flow cryostat in which magnetic flux densities up to 15 T can be applied. The V-I characteristics of both samples were taken at $T = 77\,K$ and a pre-selected set of different magnetic fields in the range of 0 T to 5 T. The obtained critical currents in dependence of the magnetic

field for samples #S-2 and #S-3 are shown in figure 4.4 with red circles and blue triangles, respectively.

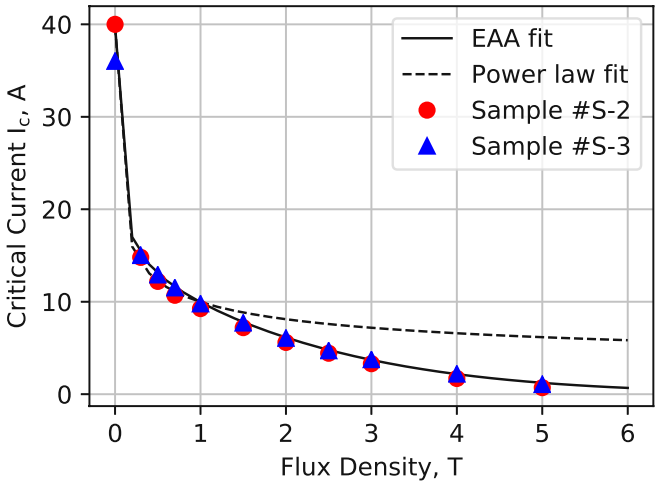

Figure 4.4 – *Characterization of samples #S-2 and #S-3 at 77 K and different magnetic fields with flux densities up to 5 T. The experimental data are approximated with a 'classical' power law $I_c \propto B^{-\alpha} \rightarrow I_c = 10B^{-0.3}$ and the 'Extended Alpha Approximation' from equation (20) with parameters taken from table 4.1.*

In a first approximation a simple power law

$$I_c \propto B^{-\alpha}, \tag{19}$$

where α is an empirical parameter was applied. However, it can be seen that there is a disagreement between the approximation with $I_c = 10 \cdot B^{-0.3}$ and the experimental values for $B > 1\,\mathrm{T}$. The 'classical' power approximation is therefore not sufficient to model the dependence of $I_c(B)$ of double-disordered tapes at $T = 77\,\mathrm{K}$ and was therefore extended with additional parameters. The approximation of $I_c \propto B^{-\alpha}$ is indicated by a dashed line in figure 4.4.

The following equation (20) was made to model the dependence of the critical current on the magnetic field appropriately and named 'Extended Alpha Approximation' (EAA)

$$I_c(B) = I_0 \cdot (\bar{B} + \delta_0)^{-(\alpha_0 + \beta \cdot \bar{B})}. \tag{20}$$

The best fit of the experimental data was obtained with the values $I_0 = I_c(1\,\mathrm{T}) = 10\,\mathrm{A}$ and the dimensionless parameters $\delta_0 = 0.01$, $\alpha_0 = 0.3$ and $\beta = 0.2$. I_0 denotes the critical current at 1 T. In equation (20) $\bar{B}$ is the applied magnetic field divided by 1 T.

The shifting parameter δ_0 was introduced to avoid divergence at $B = 0\,\mathrm{T}$.

As it was already indicated in figure 4.3, the n-value is generally a function of B as the value of n decreases with increasing field. From the measured V-I characteristic of samples #S-2 and #S-3, the according n-values were determined and the dependence on the flux density B is shown in figure 4.5.

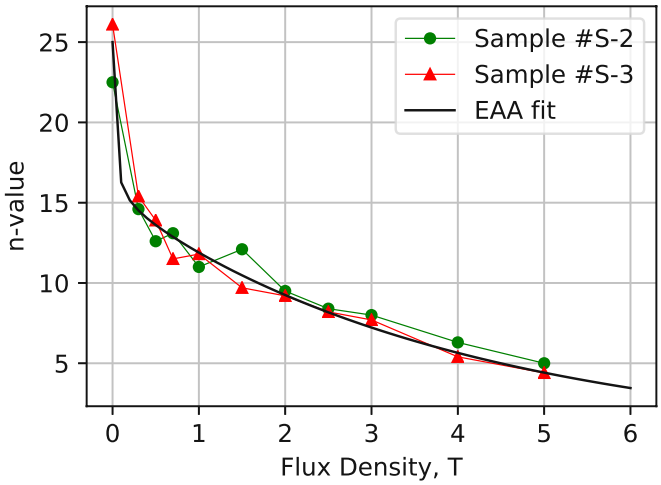

Figure 4.5 – *The n-values were determined from the V-I curves of two samples #S-2 and #S-3. The dependence of n on the flux density B was approximated with a function of similar structure as the 'Extended Alpha Approximation' (solid black line).*

The best approximation for n of the samples #S-2 and #S-3 in figure 4.5 was found to be

$$n(B) = \left[a + \frac{b}{\bar{B} + \delta_1}\right] e^{-\alpha_1 \bar{B}}. \tag{21}$$

To model the n-values in figure 4.5 the parameters $a = 15$, $b = 0.2$, $\delta_1 = 0.02$ and $\alpha_1 = 0.245$ were used.

To summarize the previously derived approximations for the n-values and the critical currents I_c the curves are depicted together in figure 4.6.

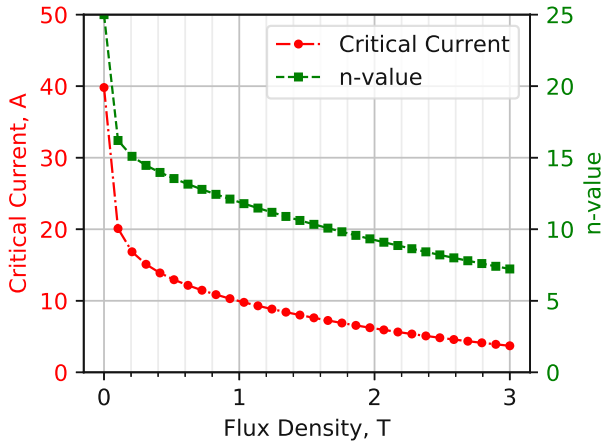

Figure 4.6 – *Curves of the approximations for I_c and n derived from equations* (20) *and* (21)*, respectively. Both curves are strongly dependent on the magnetic field B.*

To summarize this section, the parameters used in equations (20) and (22) found to be suitable for double-disordered tapes are listed in table 4.1. For samples with lower currents, the parameter I_0 needs to be fine-tuned and set to e.g. $I_0 = 8.5\,\mathrm{A}$.

Parameter	Quantity
$I_0 = I_c(1\,\mathrm{T})$	10 A
δ_0	0.01
α_0	0.3
β	0.2
a	15
b	0.2
δ_1	0.02
α_1	0.245

Table 4.1 – *Set of parameters used to model the field dependence of the critical current and the n-value for double-disordered tapes.*

4.1.3 Voltage in Inhomogeneous Magnetic Fields

The previously derived empirical approximation (18) is written in a more general B-dependent form yielding

$$U(B) = \left(\frac{\mathrm{d}U}{\mathrm{d}x}\right)_{\mathrm{cr}} \cdot \Delta x \cdot \left(\frac{I}{I_{\mathrm{c}}(B)}\right)^{n(B)}. \tag{22}$$

In this expression the term $\left(\frac{\mathrm{d}U}{\mathrm{d}x}\right)_{\mathrm{cr}}$ denotes the voltage drop per unit length i.e. the electric field which is used as criterion for voltage evaluation. In equation (22) it is assumed that the voltage contacts are separated by a length Δx in which the field is homogeneously distributed. The previously experimentally determined relations for I_{c} (20) and n (21) and can be substituted in equation (22) giving the following expression

$$U(B) = \left(\frac{\mathrm{d}U}{\mathrm{d}x}\right)_{\mathrm{cr}} \cdot \Delta x \cdot \left[\frac{I}{I_0}(\bar{B}+\delta_0)^{+(\alpha_0+\beta\cdot\bar{B})}\right]^{\left[a+b/(\bar{B}+\delta_1)\right]\exp(-\alpha_1\bar{B})}. \tag{23}$$

In equation (23) a homogeneous distribution of the magnetic field between the 4-probe potential contacts along Δx is assumed. To relate equation (23) to an inhomogeneous field distribution $B(x)$ along Δx, the following integral expression with $\bar{B} \rightarrow \bar{B}(x)$ is used to describe the total voltage response

$$U_{\mathrm{int}} = \left(\frac{\mathrm{d}U}{\mathrm{d}x}\right)_{\mathrm{cr}} \cdot \int_{\frac{-\Delta x}{2}}^{\frac{\Delta x}{2}} \left[\frac{I}{I_0}(\bar{B}(x)+\delta_0)^{+(\alpha_0+\beta\cdot\bar{B}(x))}\right]^{\left[a+b/(\bar{B}(x)+\delta_1)\right]\exp(-\alpha_1\bar{B}(x))} \mathrm{d}x. \tag{24}$$

In this expression, the limits of the integrals are chosen in order to center Δx around $x = 0$ which is suitable for magnetic fields with a symmetric field distribution. This is true for the magnet of the M-Scanner and for other magnet assemblies investigated in this work.

4.2 Tests on Short Samples

This section reports experimental tests of the previously derived model on short samples #S-5 - #S-8. Additionally the impact of artificially introduced defects on the voltage response was investigated.

The tests were performed on the short sample testbench with applied miniature permanent magnets and in a setup where a sample tape translates through the magnet

channel of the 2.61 T permanent magnet. To create macroscopic defects on the tape, a diamond hard spike tool was used to carefully remove the silver cap and the underlying YBCO layer via scratching.

4.2.1 Zooming effect

The impact of defects on the critical current in magnetic fields with edge gradients is discussed and experimentally tested in the following on a sample mounted on the short sample test bench employing the miniature permanent magnet assembly. The results of this section are already published in [100].

The 12 cm long sample #S-5 was placed on the short sample testbench in a bath of liquid nitrogen and tested in different configurations, (a) in self-field and (b) with applied miniature permanent magnets. In a second test sequence, a 2.4 cm long scratch along the sample was introduced and the V-I characteristic was taken again (c) in self-field and (d) with magnet assembly placed on the testbench.

The 2.4 cm long scratch was introduced with a hard metal spike tool and placed aside the center with a distance of 1 mm from the edge. It was priory confirmed in other tests, that such a scratch in transverse direction completely interrupts the superconducting current.

A scheme of the prepared sample is shown in figure 4.7 for case (d) where magnet and scratch were both applied. The sample (1) was 4-probe connected with current and voltage contacts, depicted as (2) and (3), respectively. In the scope of the measurement, a magnet assembly (4) was placed on the sample and a scratch (5) was introduced in the sample. The length $\Delta x_0 \approx 3\,\mathrm{cm}$ denotes the distance between both voltage contacts and $\Delta x_\mathrm{m} \approx 0.8\,\mathrm{cm}$ corresponds to the part where the tape is exposed to the magnetic field.

In contrast to the measurement described above in section 4.1.1, a stack of two cylindrical miniature permanent magnets is used to generate the magnetic field. The flux density distribution is shown in figure 4.8 exhibiting a flat top in the center with maximum flux density $B_\mathrm{max} = 0.53\,\mathrm{T}$.

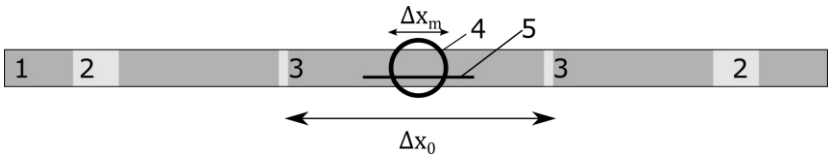

Figure 4.7 – *Scheme of the* 12 cm *long prepared sample in the short sample test bench. The sample (1) was 4-probe connected with current (2) and voltage (3) contacts. The voltage contacts were separated by a distance of* Δx_0*. A stack of cylindrical miniature permanent magnet (4) was placed in the center of the sample. The dimension of the flux density distribution is denoted with* Δx_m*. A longitudinal,* 2.4 cm *long scratch (5) was introduced in the sample with a hard spike tool. The sample was placed in a bath of liquid nitrogen and the V-I characteristic was taken. The experiment is also described in [100].*

The electric field generated by different applied currents I along the tape between the stack of the miniature permanent magnets was modeled using the previously derived approximations for the n-value (21) and the voltage drop (23). The combined equation is explicitly written in equation (25)

$$E(x) = \left(\frac{\mathrm{d}U}{\mathrm{d}x}\right)_{cr} \left[\frac{I}{I_0}(\bar{B}+\delta_0)^{-(\alpha_0+\beta\bar{B})}\right]^{\left[a+b/(\bar{B}+\delta_1)\right]\exp(-\alpha_1\bar{B})} . \tag{25}$$

This expression can computed by a straight forward calculation for which the parameters listed in table 4.1 were used. To fit the lower critical current of sample #S-5, the value of I_c at 1 T was adapted to $I_\mathrm{c}(1\,\mathrm{T}) = 8.5\,\mathrm{A}$.

In this way, the electric field $E(x)$ in a tape exposed to the field $B(x)$ was modeled for currents from 10 A to 12 A and the experimental values of the magnetic field distribution $B(x)$ of the cylindrical miniature permanent magnets. The curves of $E(x)$ are depicted in figure 4.8 for the selected currents in the range of $I_\mathrm{tr} = 10\,\mathrm{A}$ to 12 A. It turns out, that the full width at half maximum (FWHM) of the electric field is FWHM = 7 mm and remains nearly unchanged for different transport currents. Appearing negative values of $B(x)$ for $|x| > 5\,\mathrm{mm}$ are too low to cause a sufficient electric field for a voltage response. The minimum value B_min is above $B_\mathrm{min} > -0.06\,\mathrm{T}$ which means that the magnitude of B_min is roughly one order of magnitude lower than the magnitude of the maximum value B_max.

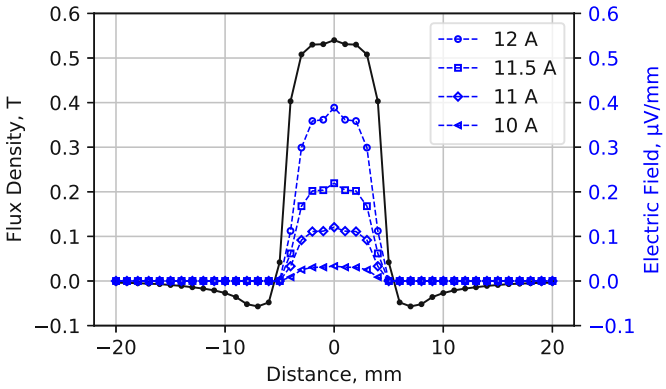

Figure 4.8 – *Flux density distribution of the magnet stack with cylindrical miniature permanent magnets. The maximum field is* 0.53 T *in the center of the assembly. The electric field* $E(x)$ *was modeled for different transport currents* I_{tr} =10 A *to* 12 A. *The full width at half maximum is* $FWHM = 8$ mm *for the magnetic field* $B(x)$ *and* $FWHM = 7$ mm *for the calculated electric fields* $E(x)$.

The corresponding V-I curves of the 4-probe measurements are shown in figure 4.9. The voltage contacts are separated by $\Delta x_0 = 3$ cm and the criterion *cr-1* denotes the critical voltage of $V_c = 3\,\mu V$. To evaluate the impact of the 2.4 cm long defect on I_c in all cases (a) - (d), the criterion *cr-1* was used to evaluate the critical current I_c.

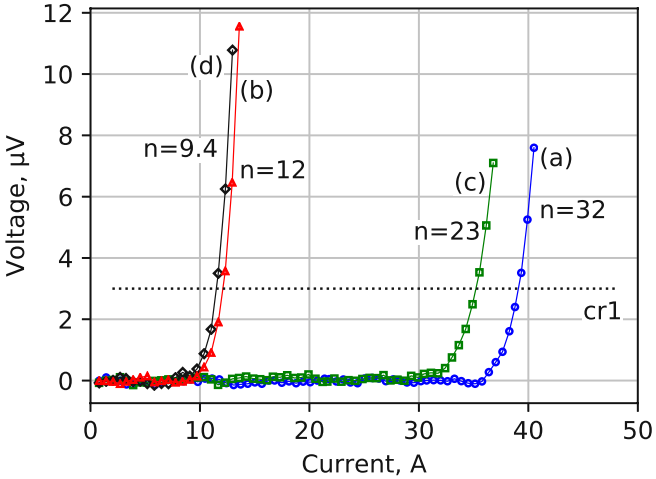

Figure 4.9 – *V-I characteristics of short sample #S-5 in the short sample testbench. Four tests were performed, (a) in self-field, (b) with artificially introduced scratch, (c) with miniature permanent magnet and (d) with scratch and miniature permanent magnet.*

The critical current in self-field (a) was determined to $I_c^{(a)} = 39\,\mathrm{A}$ with a related n-value of $n = 32$. Applying the magnet assembly (b) degraded the critical current to $I_c^{(b)} = 12.1\,\mathrm{A}$ and reduced the n-value to $n = 12$. Introduction of the longitudinal, 2.4 cm long scratch degraded the critical current to $I_c^{(c)} = 35.2\,\mathrm{A}$ in self-field and when the magnets were applied it reached $I_c^{(d)} = 11.5\,\mathrm{A}$. The n-values were found to be n=23 in case (c) and n=9.4 in case (d).

The n-values and critical currents of the tests (a)-(d) are listed in table 4.2. Both, the critical current and the n-value degrade when a defect is introduced to the tape (as it is in cases (c) and (d)).

Case	I_c, A	n-value
(a) self-field	39	32
(b) magnet assembly	12.1	12
(c) self-field with scratch	35.2	23
(d) magnet assembly with scratch	11.5	9.4

Table 4.2 – *For the determination of the critical current I_c in the investigated cases (a)-(d) the criterion cr-1 was used. According n-values were determined from the current-voltage characteristics.*

It follows from the distribution of the inhomogeneous electric field within the tape, that in the areas of low magnetic field practically no voltage response is expected. Therefore, the voltage drop practically appears in the high-field zone within the region of the applied magnets only. This means that, the 'out-of-field' regions will retain a higher I_c whereas the much lower applied transport currents I_{tr} correspond to the lowest I_c within the magnetic flux zone.

A tape defect is therefore most important within the high-field flux zone of the magnets since the 'low enough' applied transport current will not cause a voltage response in the 'out-of-field' region. This obviously doesn't apply to 'severe' local defects, that reduce the critical current in the 'out-of-field' zone to a level, that is below the critical current I_c in the high-field zone.

This means that no contribution of I_c inhomogeneities will be detected in the 'out-of-field' regions in the voltage response between two potential contacts. Due to the specific level of $I_c^{(a)}$ and $I_c^{(b)}$, this applies if the degradation of I_c due to a defect or inhomogeneities is lower than $\sim 1/3$ of $I_c^{(a)}$.

An estimation of the relative impact of the defect on I_c was calculated and the results

written in table 4.3. It was considered, that the effective cross-section of the tape is narrowed by the width of the scratch and a surrounding zone of HTS layer damaging micro-cracks. In the case of the introduced scratch, the critical current was degraded by 9.7 % relative to the critical current of the 'clean' tape.

Following from this reduction of I_c, the effective width of the scratch was assumed to be ∼0.4 mm corresponding to 10 % of the tape width. A difference of the impact of the defect between the cases whether with or without the applied magnet assembly was observed.

When the magnet assembly was applied, the relative impact of the defect is only 4.9 % which corresponds to ∼ 1/2 of the relative impact compared to the cases without magnets.

	I_c, A	I_c^{scr}, A	Impact $(I_c - I_c^{scr})/I_c$
s.f.	39	35.2	9.7 %
mag.	12.1	11.5	4.9 %

Table 4.3 – *Relative impact of scratch on the critical current I_c. In the case when the magnets were applied, the degradation of the critical current due to the defect was 4.9 % whereas in self-field the degradation was 9.7 %.*

In the following, the equations of the EAA were used to model the response of the voltage along the sample in the cases (b) where the magnetic field was applied and (d) additionally introduced scratch with applied field.

Referring to the shape of the magnetic field $B(x)$, the integral expression of the voltage response (see equation (24)) can be split into two parts of homogeneous fields. In the first part the homogeneous field is $B_0 = 0\,\mathrm{T}$ and in the second part the homogeneous field $B_m = 0.53\,\mathrm{T}$.

$$U_{int} \approx \left(\frac{dU}{dx}\right)_{cr} \left[\left(\frac{I}{I_0}\right)^{n(0)} \cdot {\delta_0}^{\alpha_0 \cdot n(0)} (\Delta x_0 - \Delta x_m) + \left[\frac{I}{I_0} B_m^{\alpha_0 + \beta B_m}\right]^{n(B_m)} \cdot \Delta x_m\right] \quad (26)$$

The first term that contains $(\Delta x_0 - \Delta x_m)$ can be neglected when the magnetic field B_m is much larger than B_0. In this case, equation (26) can be reduced to the following expression

$$U_{int} \approx \left(\frac{dU}{dx}\right)_{cr} \left(\frac{I}{I_0}\right) B_m^{(\alpha_0 + \beta B_m) \cdot n(B_m)} \cdot \Delta x_m. \quad (27)$$

The EAA equation (27) was used to model the current-voltage dependencies for the cases (b) and (d), which shown in figure 4.10. The impact of the scratch was considered formally by reducing I_0 by 9.7 % from originally $I_0 = 8.5\,\mathrm{A}$ to ${I_0}^{\mathrm{scr}} = 7.6755\,\mathrm{A}$.

Additionally, the curves were modeled using a simple power law (SPL), $U_{\mathrm{SPL}} = \left(\frac{I}{I_0} \cdot {B_{\mathrm{m}}}^{0.3}\right)^n \cdot \Delta x_{\mathrm{m}}$.

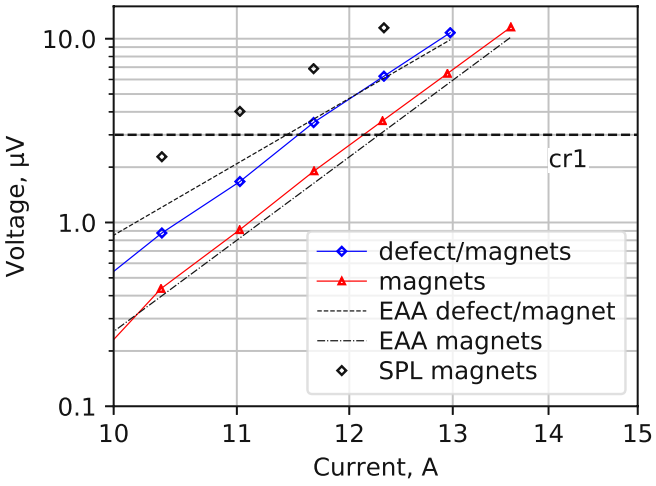

Figure 4.10 – *Comparison of experimental values and modeling with the 'Extended Alpha Approximation' (EAA). Equation* (27) *was employed to model the voltage response. Red triangles denote the V-I characteristic in the magnetic field of the miniature permanent magnet assembly. Blue squares denote the V-I characteristic when a longitudinal scratch is additionally employed. In comparison to the EAA modeling, the misfit obtained from a simple power law (SPL) is larger.*

The agreement of the modeling with the EAA expression (27) matches not perfectly to the experimentally found data. However, modeling with the simple power law shows a larger misfit.

4.2.2 Diode Effect

The dependence of the V-I characteristic and the critical current on the polarity of the transport current was investigated separately which is reported in this section.

In this study, the V-I characteristics of two different samples #S-6 and #S-7 with different applied magnet stacks are compared. Both samples were silver capped (without the copper layer), cut from the same tape and therefore from the same production run. Additionally to 'simple' V-I measurements, the polarity of the applied transport

current was reversed and the following positive and negative voltage output recorded. Surprisingly, it turned out, that the value of the critical current is dependent on the current polarity when a stack of permanent magnets was applied. In self-field measurements, no such deviations were observed in the measured samples.

In the following description, the polarity of the transport current is indicated with I^+ and I^- and was considered only relative to the actual measured sample and cannot be taken as 'absolute' for all samples. In the following, the current polarity I^+ conventionally gives the lower critical current of both current directions when the magnets were applied.

Two samples #S-6 and #S-7 with a length of 12 cm were prepared similar to sample #S-5, presented in the previous section 4.2.1. A scheme of the prepared samples is shown in figure 4.11. Current and voltage contacts are indicated as (1) and (2). Introduced scratches are denoted as (3) and the applied magnet assembly by (4). It can be seen that for sample #S-6 the stack of cylindrical magnets ($B_{\mathrm{max}} = 0.53\,\mathrm{T}$) was applied whereas for sample #S-7 the stack of rectangular magnets ($B_{\mathrm{max}} = 0.57\,\mathrm{T}$) was used.

Again, Δx_{m} denotes the spatial length of the flux zone, whereas Δx_0 corresponds to the distance between the voltage contacts. For both samples, $\Delta x_0 = 3\,\mathrm{cm}$, but $\Delta x_{\mathrm{m}} = 0.8\,\mathrm{cm}$ for the cylindrical magnets applied to sample #S-6 and $\Delta x_{\mathrm{m}} = 1\,\mathrm{cm}$ for the rectangular magnets used for sample #S-7. In this setup, the length Δx_{m} defined the voltage criterion *cr-mag* in the measured V-I characteristics when the magnets were applied. In self-field, the distance between the voltage contacts Δx_0 defined the value of the critical voltage using a standard criterion which is indicated as *cr-1*.

The longitudinal scratch of sample #S-6 had a length of ∼2 cm and was placed asymmetrically to the center of the tape, similar to the scratch in sample #S-5. In contrast, a vertical scratch with a length of 0.08 cm was introduced on one side of sample #S-7 outside the flux zone Δx_{m}. However, the scratch was placed at a distance of $\sim 0.5\,\mathrm{cm}$ from the edge of the magnet and hence within the zone of reversed field of the magnet assembly as it can be seen in figure 4.2.

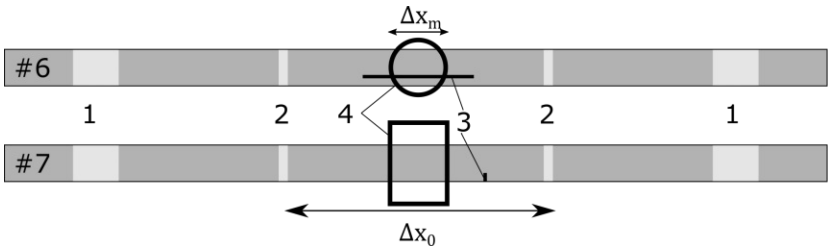

Figure 4.11 – *Scheme of the prepared samples #S-6 and #S-7. Current and voltage contacts are indicated as (1) and (2), respectively. Introduced scratches are shown as (3) and the applied magnet assembyl is denoted by (4).*

The V-I characteristics of sample #S-6 for both current directions I^+ and I^- are shown in figure 4.12. On the right-hand side the measurements taken in self-field are shown and the V-I curves with the cylindrical magnets applied are visible on the left-hand side. All curves were taken 2 to 5 times and averaged values with the corresponding standard deviation are shown.

The critical current in self-field measurements obtained from the critical voltage defined by *cr-1* is not affected by the reversion of the transport current polarity. This is in contrast to the case when the magnet stack is applied and a difference on the critical current of $\Delta I_c = 0.15\,\mathrm{A}$ is observed when the transport current polarity is reversed.

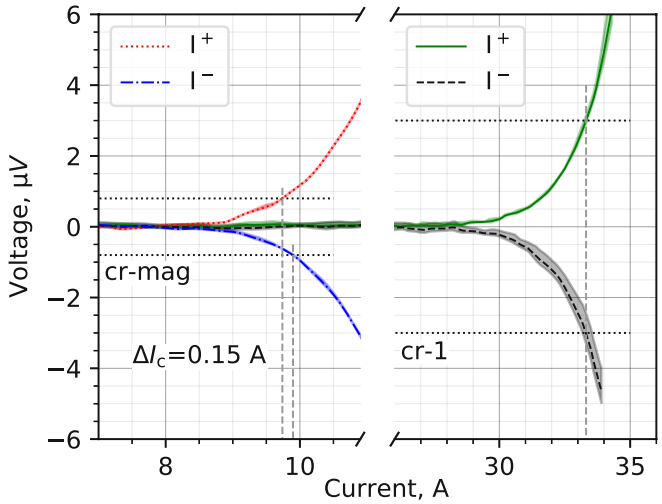

Figure 4.12 – *V-I characteristics of sample #S-6 (cylindrical magnets applied with $B_{\max} = 0.53\,\mathrm{T}$). The critical current, obtained from cr-mag in the left part of the figure deviates by $\Delta I_c = 0.15\,\mathrm{A}$. In contrast, no difference in the critical current is observed when the transport current polarity is reversed in self-field.*

An analogous result was observed for sample #S-7 which is shown in figure 4.13. In self-field, the critical current, defined by the criterion *cr-1*, was on the same level for both polarities I^+ and I^- of the transport current. Similar to the previous case and when the magnet stack was applied, a difference of $\Delta I_c = 0.3\,\mathrm{A}$ of the critical current was observed when the transport current polarity was reversed.

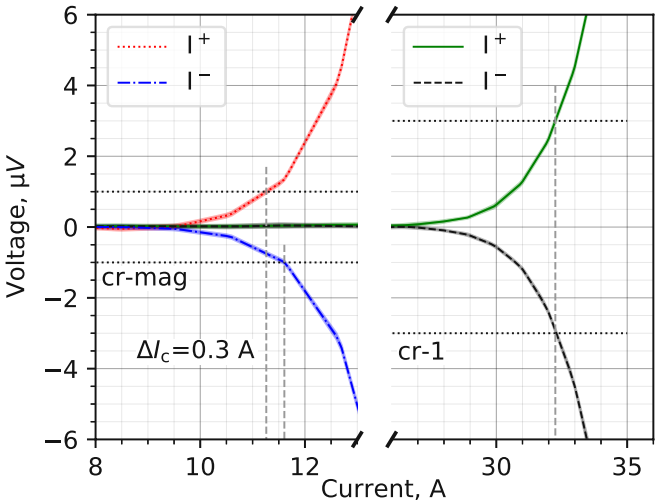

Figure 4.13 – *Diode Effect Sample #S-7 (rectangular magnets applied with* $B_{\mathrm{max}} = 0.57\,\mathrm{T}$*). The difference of the critical current in dependence of the transport current direction, obtained by cr-mag, is* $\Delta I_c = 0.3\,\mathrm{A}$.

It was observed that the value of ΔI_c is higher for sample #S-7 than for #S-6. In comparison to sample #S-6, the maximum value of the flux density of the magnet stack applied in #S-7 was $B_{\mathrm{max}} = 0.57\,\mathrm{A}$ and larger than for #S-6, where it was $B_{\mathrm{max}} = 0.53\,\mathrm{T}$. Since the description of the origin of this effect was not focus of this thesis, it is only presented here without further systematic investigation.

4.2.3 Semi-Dynamic M-Scan with soldered contacts

Sample Preparation

The silver capped sample #S-8 was investigated in a semi-dynamic configuration of the M-Scan which means that the sample was moving through the magnet of the M-Scanner but being still 4-probe connected with soldered contacts. In this chapter the investigated impact of defects on the tape surface during the translation through a flux zone is described. The flux density distribution in the the 2.61 T magnet was already shown in figure 3.7.

The 55 cm long sample #S-8 was prepared exhibiting two artificial defects E1 and E2, which were introduced with the diamond spike tool. The defects had a width of 1.1 mm and 1.5 mm and hence reduced the sample's cross-section by about ∼30 % to 40 %. E1 was characterized as a vertical scratch with dimensions $1 \times 1.5\,\mathrm{mm}^2$ and E2 was identified as defect zone with dimensions $2.5 \times 1.1\,\mathrm{mm}^2$. The defects were separated by a distance of $\Delta_E = 7\,\mathrm{cm}$ i.e. during translation there was only one defect inside the 4 cm long homogeneous flux zone at once.

Voltage and current contacts were soldered with flexible wires at the outer ends of the sample and a 20 cm long section of the sample was guided through the magnet. The voltage signal was amplified in a 60 dB low-noise amplifier. The sample was prepared such, that both defects fully translate through the channel of the permanent magnet.

In figure 4.14 a scheme of the prepared sample is shown. The sample was point-welded to a stainless-steel tape which was connected by two motors driving. In this setup, the tape translated with a speed of $1\,\mathrm{mm\,s^{-1}}$.

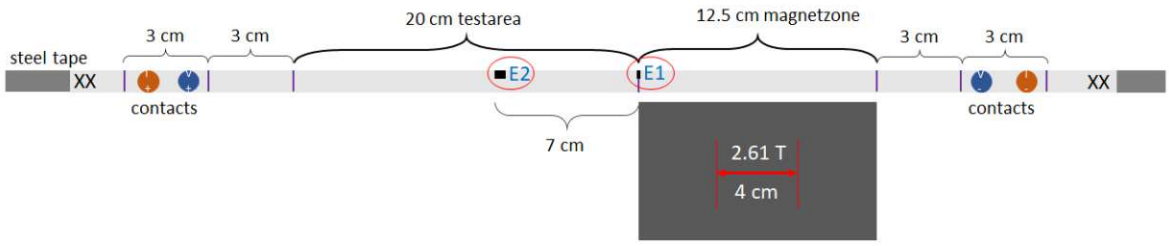

Figure 4.14 – *Scheme of the tape used in the M-scan with soldered contacts. Artificially introduced defects are indicated as E1 (vertical scratch, dimensions* $1 \times 1.5\,\mathrm{mm}^2$*) and E2 (defect zone with dimensions* $2.5 \times 1.1\,\mathrm{mm}^2$*). The tape translated with a velocity of* $1\,\mathrm{mm\,s^{-1}}$ *into the right direction.*

Figure 4.15 shows the sample implemented in the experimental setup. The Magnet and the sample was placed in a styrofoam vessel which was filled with liquid nitrogen. Sample and magnet were fully immersed in liquid nitrogen during operation.

Figure 4.15 – *Picture of the silver capped sample in the experimental setup. Sample and magnet were fully immersed in liquid nitrogen during the scan.*

A more detailed view is shown in figure 4.16. The sample is at its initial position before the scans and both defects are indicated with blue circles as E1 and E2, respectively. The tape was guided through the magnet channel by copper rollers at the entrance of the magnet slit.

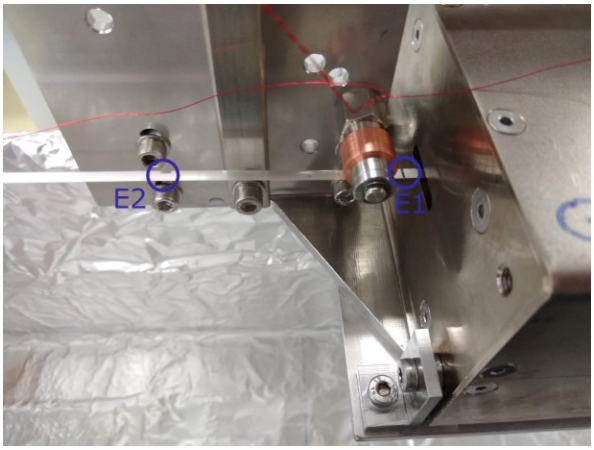

Figure 4.16 – *More detailed view of the prepared sample. Defects E1 and E2 are marked with blue circles. The sample was moving to the right with* $1\,\mathrm{mm\,s^{-1}}$ *during operation.*

Scan Results

By translating the sample with $1\,\mathrm{mm\,s^{-1}}$, the test area was fully traversed after 200 s. After each scan, the sample was re-placed at its initial starting position. The sample was loaded with different transport currents and the voltage drop of cases $I_{\mathrm{tr}} = 5.0\,\mathrm{A}$, 6.3 A and 6.9 A is shown in figure 4.17. As expected, the level of the voltage drop is the lowest for $I_{\mathrm{tr}} = 5\,\mathrm{A}$ and increasing with increasing transport current. All scans were starting at $t = 0\,\mathrm{s}$. At $t = 46\,\mathrm{s}$, defect E1 reached the homogeneous 2.61 T flux zone of

the permanent magnet which was immediately followed by an increased response of the voltage signals. The response was more pronounced in case with 6.9 A in comparison to the cases with 6.3 A and 5.0 A. The level of the peak in the case of 5.0 A was 1 µV to 2 µV above its pre-peak value. The peak of E1 in the voltage signals decreased after 40 s returning back to its pre-peak level. This corresponds exactly to the time of translation through the 4 cm long homogeneous zone of the permanent magnet.

A similar situation was observed for the second defect, E2. At $t = 123$ s, E2 entered the 4 cm long homogeneous flux density zone. Again the voltage signal increased and a 40 s long peak was observed.

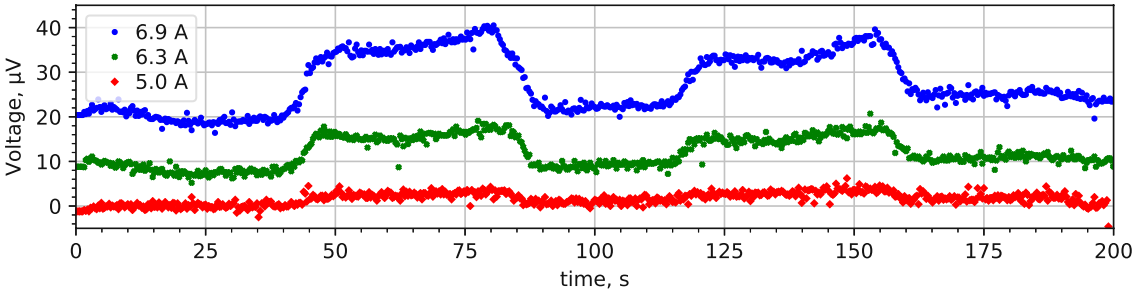

Figure 4.17 – *Measured voltage response of scan with soldered contacts and transport currents* $I_{\mathrm{tr}} = 5.0\,\mathrm{A}$, 6.3 A *and* 6.9 A *at a translation speed of* $1\,\mathrm{mm\,s^{-1}}$.

Modeling with the EAA approach

The translation of defects like E1 and E2 through the 2.61 T permanent magnet was simulated with the EAA approach as well. The parameters of table 4.1 were used for the calculation of $U(B)$ and $n(B)$ with equations (23) and (21), respectively. However, the parameter I_0 was tuned to be $I_0 = 12.5\,\mathrm{A}$ to take the higher critical currents of sample #S-8 into account.

To simulate the impact of the defects on the voltage response numerically, an 1-dimensional array representing a discrete distribution $I_0(x)$ along the sample was considered. At some entries of this array, the value of I_0 was lowered to a value I_{D} which corresponds to a local degradation of the critical current. In this way, the reduction of the cross-section at the defects position was taken into account. In this simulation, the mesh size of the 1-dimensional grid was set to 0.5 mm.

The voltage drop $U_{\mathrm{int}}(B)$ along the tape was repeatedly calculated for each incrementally varied position of the defect within the flux zone $B(x)$. In other words, the voltage response was modeled for each discrete step of the defect during its translation

through the (static) magnetic flux zone.

Defect E1 ($1 \times 1.5\,\mathrm{mm}^2$) was simulated by reducing I_0 locally from $I_0 = 12.5\,\mathrm{A}$ to $I_\mathrm{D} = 7.8\,\mathrm{A}$ along a simulated length of 1 mm which corresponds roughly to a local cross-section reduction by 38 %. Similarly, the defect E2 ($2.5 \times 1.1\,\mathrm{mm}^2$) was simulated by degrading I_0 by 28 % along a length of 2.5 mm. At this length, I_0 degraded locally from $I_0 = 12.5\,\mathrm{A}$ to $I_\mathrm{D} = 9\,\mathrm{A}$.

In this way, the voltage response was simulated for both defects along the $B(x)$ distribution of the permanent magnet for the three applied transport currents. The results of the simulated voltage response (dashed lines) of the defect's transition through the permanent magnet are shown together with the measured data (markers) in figure 4.18.

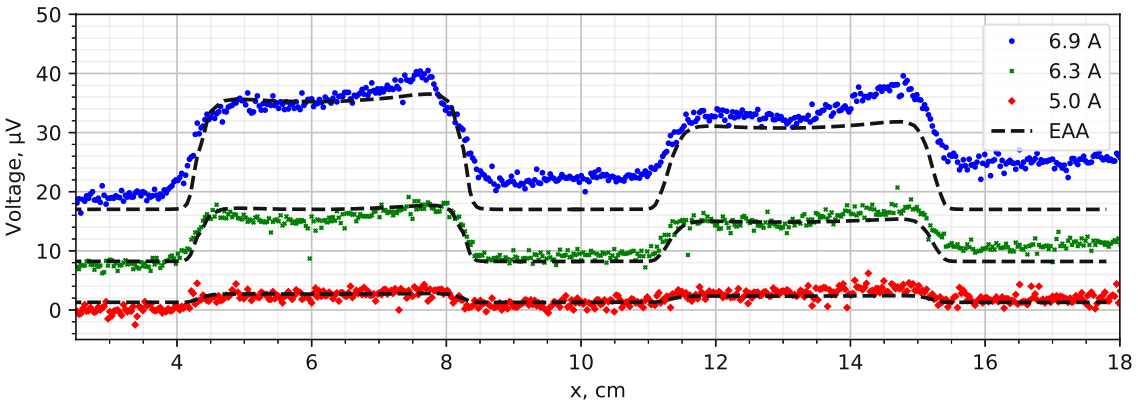

Figure 4.18 – *Comparison of the simulated voltage response with the EAA approach and measured voltage response for three different transport currents* 5.0 A, 6.3 A *and* 6.9 A.

For the cases $I_\mathrm{tr} = 5.0\,\mathrm{A}$ and $I_\mathrm{tr} = 6.3\,\mathrm{A}$ the simulated data agrees with the measured results. In the case with the highest $I_\mathrm{tr} = 6.9\,\mathrm{A}$ disagreement between measured and simulated results was observed which apparently increases with increasing scan length x. Two combined effects are considered to be origin to this behavior.

First, the current flow in the dissipative regime might partly flows through the silver cap layer of the superconducting sample. In a simple model of parallel connected resistors between the silver and YBCO layer, the relative amount of current flowing through the silver layer increases with increased applied transport current. Since the simulations in the scope of this experiments consider current flow through the superconducting layer only, errors are made when neglecting the current flow in the silver. However, errors due to this effect in the silver capped sample #S-8 were considered

to play a minor role in comparison to a representative copper coated sample, since the resistance of the thin silver layer is about ∼100 times greater than of the copper coating.

Second, the critical current of the sample might be not homogeneously distributed as it was assumed in the simulated tape. A gradual, 'slow' decrease of the critical current along x will result in an according increasing voltage response.

Finally, the slope of the voltage increase when the defect enters the magnet was investigated. Defects E1 and E2 differ in their dimensions ($1 \times 1.5\,\mathrm{mm}^2$ and $2.5 \times 1.1\,\mathrm{mm}^2$, respectively) as described above. In figure 4.19, the case of $I_{\mathrm{tr}} = 6.3\,\mathrm{A}$ is shown again and the slopes of the increasing/decreasing voltage signal due to the defects are denoted as black lines. The value k of the linearly approximated slopes with $g(x) = kx + d$ is written next to each slope.

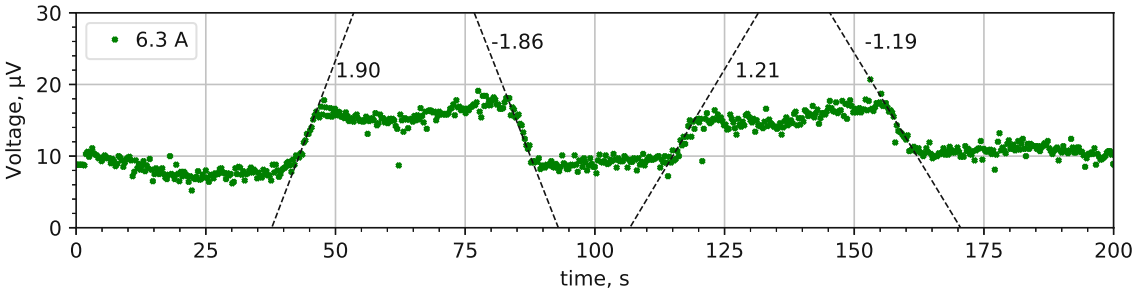

Figure 4.19 – *More detailed view on the voltage response of the case $I_{\mathrm{tr}} = 6.3\,\mathrm{A}$. The value k of the slope is written next to each line. It can be seen, that $|k|$ is in general smaller for E1 than for E2.*

Apparently, the slope $|k|$ is larger for the peak E1 (average of $|k_1| = 1.88$) than for the peak E2 (average of $|k_2| = 1.2$). This is considered to originate due to the different size of the defects and consequently different time spent during their translation through the edge zones of the homogeneous flux density distribution inside the permanent magnet. This indicates the possibility of relating the impact of the defect by evaluation of the derivative of the voltage signal.

5

3 T Pulsed Electromagnet

The previously described approach for tape characterization in magnetic fields with edge gradients was also tested and developed with a self-made 3 T pulsed electromagnet. In this section, the development of the assembly and experimental setup of the 3 T pulsed electromagnet is described.

The results of this experiment are published in [100].

5.1 Concept and Assembly

The electromagnet consists of two copper coils that are connected in series and are fixed in an outer structure. A gap between the two spools with 2 mm height makes a channel for a tape sample. Both coils have a diameter of 10 cm and a height of 2.3 cm and consist of a copper wire with 2 mm diameter. The magnet is designed to produce a flux density of 3 T in the center. This is achieved with current pulses of up to 700 A. The outer structure is able to compensate the appearing mechanical forces during operation.

The total resistance of the electromagnet circuit when the magnet is fully immersed in liquid nitrogen was determined to $R = 30\,\mathrm{m\Omega}$ allowing a power introduction of the previously mentioned 700 A.

A drawing of the magnet design is shown in figure 5.1, showing the assembly's cross sectional view with the tape guiding channel in the center. Both coils are separated with a plate made of carbon reinforced plastic.

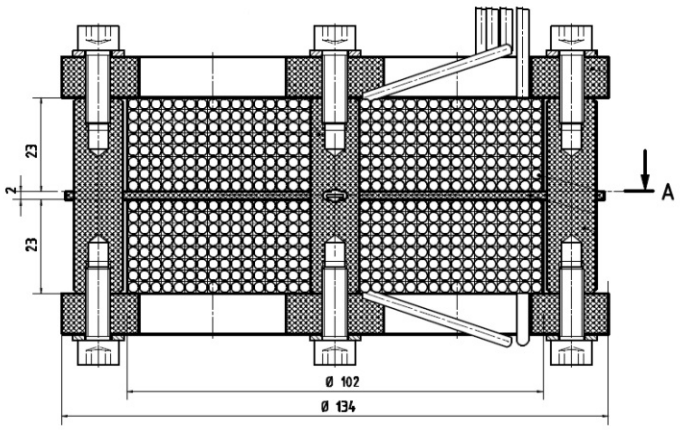

Figure 5.1 – *Scheme of the* 3 T *pulsed electromagnet. Two copper coils with diameter* 10 cm *and height* 2.3 cm *are connected in series. The flux density reaches* 3.1 T *in the center when the magnet is powered with a pulse of* 700 A *in a bath of liquid nitrogen at* 77 K. *This drawing of the magnet is taken with courtesy by Alexander Usoskin.*

The magnet was preliminary modeled based on Biot-Savart's law to achieve flux densities of 3 T at maximum current of 700 A. Nevertheless, the flux density distribution of the field component normal to the tape surface (z-direction) B_z along the tape channel was experimentally investigated via introduction of a Hall sensor. It turned out, that at room temperature the magnetic field and the resistance due to ohmic heating is sufficiently stable when the magnet is loaded with currents up to 20 A. In this stable regime, a Hall sensor was stepwise introduced into the channel and the values of the magnetic field at each position recorded.

Since there is no iron core (or other soft magnetic material) placed in the center of the windings, the produced magnetic flux density is directly proportional to the current. Since, the inductance of the coil was estimated to increase not more than ∼0.5 % due to thermal contraction of the copper material when immersed in liquid nitrogen, temperature dependency was neglected.

The proportionality constant was experimentally determined by simultaneously varying the current load in the magnet and measuring the produced magnetic field. In the following, the flux density is related to the current with the linear relation $B = c \cdot I$, where the coefficient is experimentally determined to $c = 0.0044(1)\,\mathrm{T\,A^{-1}}$.

The distribution of the magnetic field is shown in figure 5.2. The position axis (x-axis) is aligned to the center of the magnet where the magnetic field reaches 3.1 T. From the center, the flux density is monotonously decreasing on both sides and there is a zero-crossing of B_z at $x = \pm 4.7$ cm where the measured field reverses. The minimum

value is reached at $x = \pm 5.4\,\mathrm{cm}$ and then asymptotically approaches $B_z = 0\,\mathrm{T}$ again.

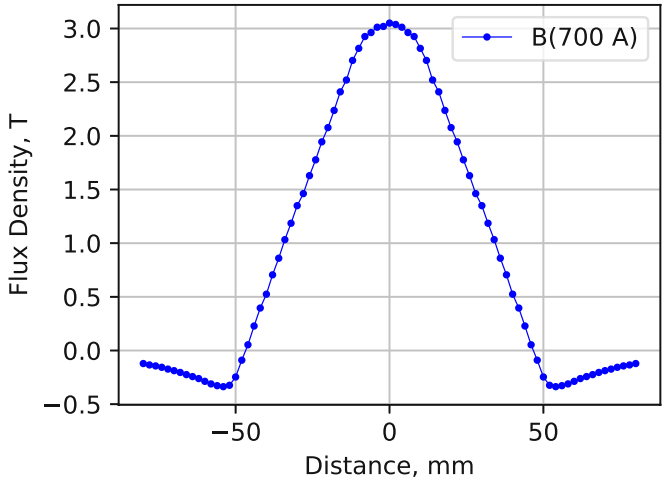

Figure 5.2 – *Flux density distribution of the* 3 T *pulsed electromagnet at maximum power of* 700 A. *The field distribution at* 700 A *has been determined from linear extrapolation of field measurements at lower currents (in the range of up to* 20 A*) with the previously determined coefficient* $c = 0.0044(1)\,\mathrm{T\,A^{-1}}$ *at a regime where the temperature and electrical resistance of the copper coils was stable.*

For experiments, the 3 T electromagnet was embedded in a setup as it is depicted in figure 5.3. The power supply (a) provided current pulses up to 700 A which were feed into the magnet (e). The introduced tape was loaded with a specific, pre-selected constant transport current I_{tr}, which was provided from a second power supply (b). The current in the magnet was recorded with a current clamp, that inductively measured the current in the power lines. This signal was directly converted to the magnetic flux density using the coefficient $c = 0.0044(1)\,\mathrm{T\,A^{-1}}$. Both, voltage and power signal were recorded by an oscilloscope (c).

The 20 cm long sample #S-4 was guided through the slit and fixed on a plate at the entrance and exit of the magnet. In one of these fixations a spring was employed to keep tension on the tape constant and compensate forces appearing due to thermal shrinking.

The voltage wires were made of a flat 50 µm thick copper tape that were insulated on one side. Both wires were coming out of the same side of the slit in order to minimize inductance in the conductor loop due to induction of changing magnetic fields due to current pulses ($\mathrm{d}B/\mathrm{d}t \neq 0$). The raw voltage signal was amplified in a 60 dB low noise amplifier (d). The assembly was placed in a cryo-vessel made of styro-foam (e).

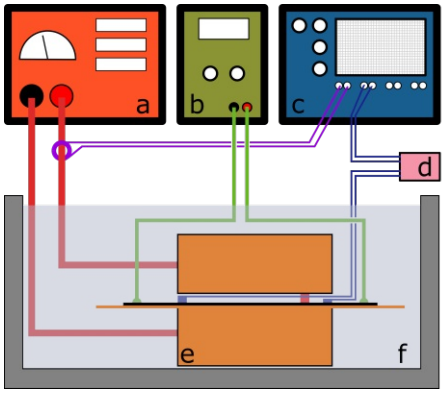

Figure 5.3 – *Scheme of the* 3 T *pulsed electromagnet testbench. The magnet (e) was connected to a power supply (a) providing pulses of* 700 A*. A power supply (b) provided currents up to* 10 A *which were loaded onto the tape. The current in the magnet was assessed with a current clamp and stored together with the voltage signal in an oscilloscope (c). The voltage signal was amplified by a* 60 dB *low-noise amplifier (d). For voltage wires,* 50 µm *thick copper tapes were used entering the magnet from the same side to avoid inductance in the conductor loop. Magnet and tape were placed in a bath of liquid nitrogen (f) during operation.*

The duration of the pulses were varied between 0.3 s to 3 s. When switched on, the power input to the magnet ($P_{\text{input}} \approx 14.7\,\text{kW}$) exceeded the cooling capacity of the LN2 bath on the magnet surface ($P_{\text{bath}} \approx -2.5\,\text{kW}$) and hence the system was leaving thermal equilibrium. Consequently, the temperature in the windings was increasing during a pulse which generally lead to an increased resistance of the current carrying copper material. Power limitation of the current source therefore reduced the maximum current output and hence reduced the field inside the magnet. The maximum duration of each pulse was set to 3 s and between two consecutive pulses the magnet was fully chilled back to 77 K by waiting a sufficient period of ∼60 s.

Figure 5.4 shows a picture of the magnet assembly in the cryo-vessel without liquid nitrogen. The flat copper voltage wires are leaving the picture on the top. The power cables that power the magnet are coming from the left side and the power lines to load current on the tape are visible from the right side. The low-resistance contact from the 700 A power cables to the 2 mm thick copper wires of the magnet are made of soldered meander-like pattern on a copper plate. One of these meander-like contact elements is visible on the left side of the picture in figure 5.4. The whole assembly was fully immersed in liquid nitrogen during operation.

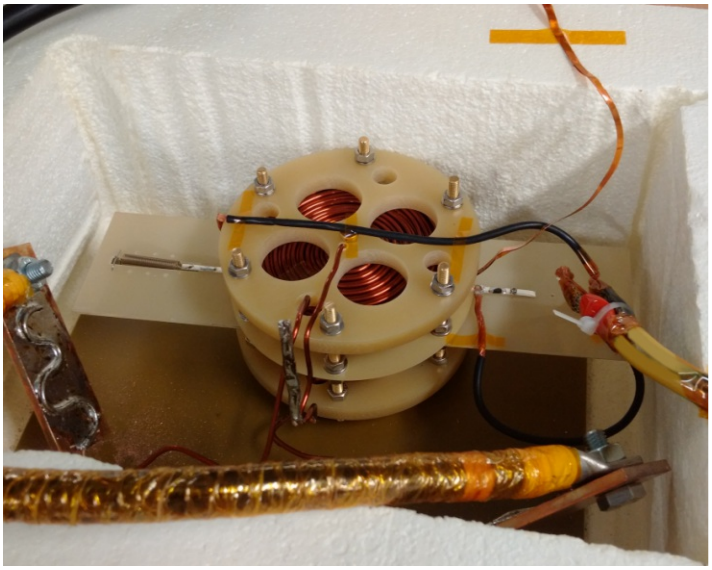

Figure 5.4 – *Picture of the* 3 T *pulsed electromagnet in styrofoam vessel. The flat copper voltage wires leave the picture on the top. The magnet is powered from the lines coming from the left side which are connected to copper plates on which the meander-like patterned end of the copper wires of the magnet have been soldered. The tape inside the magnet was loaded with currents up to* 10 A*, coming from the wires on the right. This picture is also published in [100].*

The most important specifications of the magnet and the experimental setup are summarized in table 5.1.

Description	Symbol	Quantity
Maximum magnet current	$I_{\max}$	700 A
Maximum flux density ($x = 0\,\mathrm{cm}$)	$B_{\max}$	3.1 T
Minimum flux density ($x = \pm 5.4\,\mathrm{cm}$)	$B_{\min}$	-0.37 T
Duration of magnet pulse	$\Delta\tau$	0.5 - 3 s
Sample length	l	20 cm
Current load in sample	I_{tr}	up to 10 A
Voltage lead separation	Δd_{V}	10 cm
Voltage signal amplification	G	60 dB

Table 5.1 – *Most important specifications of the* 3 T *pulsed electromagnet setup.*

5.2 Modelling of Electric Field

The results of the modeling of the electric field from equation (25) for transport currents $I_{tr} = 5\,A$ to $8\,A$ are shown in figure 5.5. In this figure, the previously shown field distribution of the 3 T pulsed electromagnet is implemented as well using black datapoints.

The calculated electric fields exhibit a peak at the center where the highest fields occur and the maximum of the peak increases with increasing transport current. The appearing local electrical fields exceed values of $0.1\,\mu V\,mm^{-1}$, which is representing the conventionally used criterion ($1\,\mu V\,cm^{-1}$) for I_c assessment. The slope of the electric field is rather steep reaching its half maximum value at $|x| = 1\,cm$, hence the assumption that the main voltage drop occurring only along a small zone in the center of the magnet is valid in first approximation.

The value of the full width at half maximum (FWHM) is 20 mm for the calculated electric fields and nearly the same for all different transport currents. In comparison, the flux density distribution exhibits a FWHM of 52 mm.

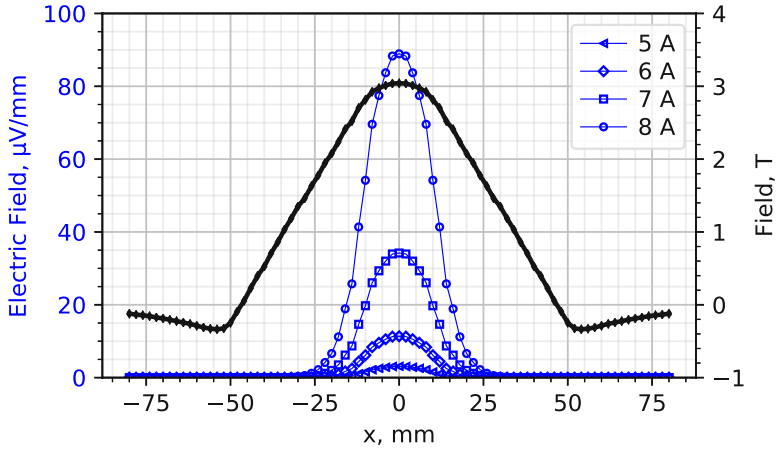

Figure 5.5 – *Calculated electric field in a 4 mm wide tape at 77 K in the pulsed 3 T electromagnet. The calculation was done using the EAA approach and current loads from 5 A to 8 A. The electric field exhibits a peak whose maximum increases with increasing transport current. The previously discussed flux density distribution of the magnet is additionally shown in black. This result is published in [100] as well.*

A more detailed view of the electric field is shown in figure 5.6. Zero-crossings of the magnetic field at $x = \pm 4.7\,cm$ define the minima in the calculated electric field. In this view, it can be seen that the modeled electric field runs through $\sim$ 13 orders of

magnitude. From this it is concluded, that large parts of the field distribution inside the magnet and especially the zones of the negative return field ($|x| > 4.7\,\mathrm{cm}$) have practically no impact on the real measured voltage drop. The severely dominating part of the electric field is located in the center of the magnet.

This is illustrated by an example: the electric field in the center of the magnet reaches $E(x = 0) = 900\,\mu\mathrm{V\,cm^{-1}}$ in the case $I_{\mathrm{tr}} = 8\,\mathrm{A}$. For the same transport current, the electric field is reduced by roughly two orders of magnitude to $E = 6\,\mu\mathrm{V\,cm^{-1}}$ at the position $|x| = 2\,\mathrm{cm}$.

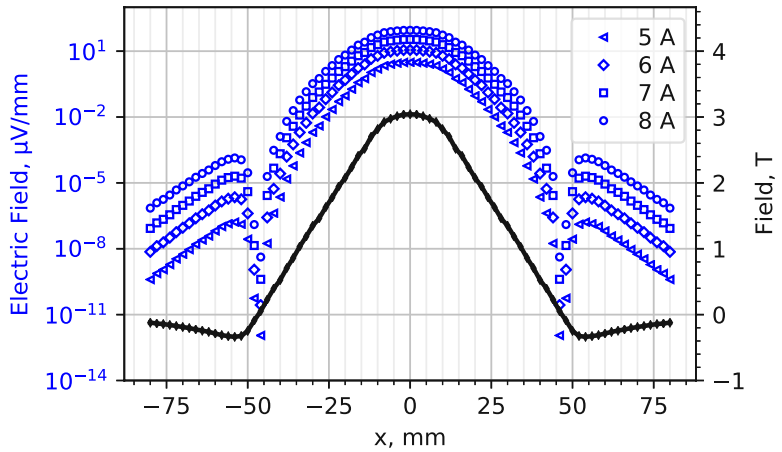

Figure 5.6 – *More detailed view on the electric field in pulsed* 3 T *electromagnet on a* 4 mm *wide tape at* 77 K *loaded with transport currents from* 5 A *to* 8 A. *The calculated electric field varies in a range of* ∼ 13 *orders of magnitude. For real measurements the voltage drop can be neglected in the zone of negative return field* ($B < 0$) *and its most dominant part is in the center. This result is published in [100].*

5.3 Voltage Response

The 20 cm long sample #S-4 was prepared and investigated in the pulsed electromagnet assembly. The voltage contacts of the 4-probe connected sample were separated by $\Delta d_{\mathrm{V}} = 10\,\mathrm{cm}$ which were directly placed at the openings of the magnet channel.

From previous measurements of double-disordered tapes (see figure 4.4) at 77 K and 3 T field, the critical current was expected to be in the range of ∼4 A to 5 A. Therefore, the voltage response for the cases $I_{\mathrm{tr}} = 3\,\mathrm{A}$, $I_{\mathrm{tr}} = 4\,\mathrm{A}$ and $I_{\mathrm{tr}} = 6\,\mathrm{A}$ is explicitly described and shown in figures 5.7, 5.8 and 5.9. Furthermore, in a subsequent analysis the tape was loaded with higher transport currents up to 8 A.

For these tests, the magnet pulse was selected to be ∼1.5 s long. For convenience, the time axes of the datasets were synchronized and the onset of the pulse chosen to be at $t = 0\,\mathrm{s}$. In all figures, the signal of the magnetic field is shown in red color and is already inverted from the signal of the current clamp.

The observation for the case of $I_{\mathrm{tr}} = 3\,\mathrm{A}$ is described in the following which is shown in figure 5.7. At $t = 0\,\mathrm{s}$ the power is switched on and the magnet builds up the field at a maximum rate of $16\,\mathrm{T\,s^{-1}}$. This is typically reached after $\sim 55\,\mathrm{ms}$. The flux density increases until it reaches its maximum value of $B_{\mathrm{max}} = 3.1\,\mathrm{T}$ at $t \sim 350\,\mathrm{ms}$. Subsequently, the flux density decreases due to increasing thermal resistance of the windings at a rate not faster than $1\,\mathrm{T\,s^{-1}}$ until the magnet is switched off.

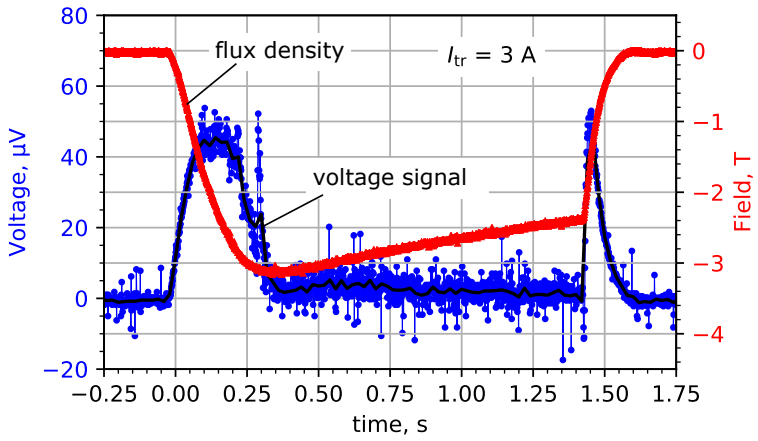

Figure 5.7 – *The sample #S-4 in the* 1.5 s *long magnet pulse of the* 3 T *electromagnet (red solid line) was loaded with a transport current* $I_{\mathrm{tr}} = 3\,\mathrm{A}$. *The onset of the pulse was chosen to be at* $t = 0\,\mathrm{s}$. *The according voltage response is shown as blue dots with averaged values (black solid line). During the quick ramp-up of the magnetic field from* $t = 0\,\mathrm{s}$ *to its maximum at* $t \sim 350\,\mathrm{ms}$ *a peak in the voltage response was observed. This 'induced' peak was considered to be a result of pushed flux vortices that render the sub-critical transport current dissipative.*

At $t = 0\,\mathrm{s}$ a peak in the induced voltage signal, which reaches its maximum value $U_{\mathrm{peak}} = 45\,\mu\mathrm{V}$ at $t = 150\,\mathrm{ms}$, is visible. It is considered that this peak comes from tape penetrating flux vortices produced by the magnetic field. Due to the rapidly increasing flux density these flux lines are pushed inside the tape. As a consequence of moving vortices, the sub-critical transport current of $I_{\mathrm{tr}} = 3\,\mathrm{A}$ is rendered dissipative.

When the maximum field is reached at $t \sim 350\,\mathrm{ms}$ the induced voltage relaxes and the 'induced' peak disappears. In the following, the voltage signal remains at a constant

level, which indicates that a transport current of $I_{tr} = 3\,A$ is sub-dissipative and hence is considered to be below the sample specific critical current I_c. Finally, the magnet is switched off at $t = 1.45\,s$ and the flux density returns to zero. The simultaneously arising 'second induced' peak in the voltage signal is not of importance and was therefore neglected.

A comparable situation was observed when the transport current I_{tr} was increased to $I_{tr} = 4\,A$ which is shown in equivalent form in figure 5.8.

The previously described induced peak is visible again, but reaches a maximum value of $U_{peak} = 65\,\mu V$. In comparison to the case $I_{tr} = 3\,A$, the higher voltage is clearly a consequence of the increased transport current. After the first induced peak the voltage doesn't immediately return to a constant level as it was observed in the previous case, but rather monotonously decreases in accordance with the decreasing magnetic field. This is considered to be a result of the transport current that dissipates in the specific flux density of the magnetic field $B(t)$ at the time t.

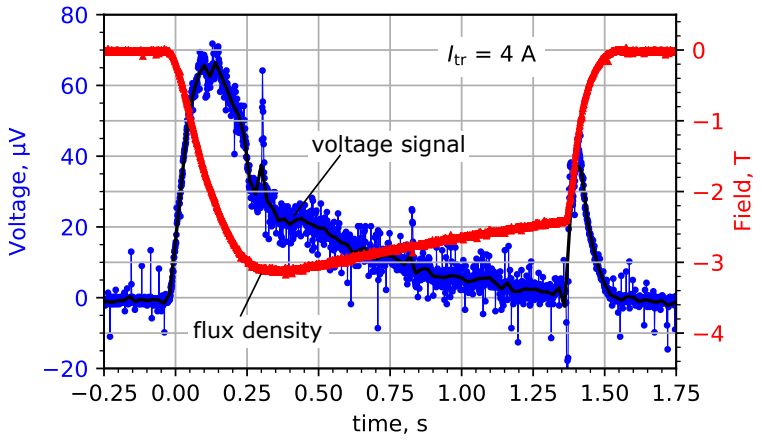

Figure 5.8 – *Magnet pulse with 3 T electromagnet with a tape load of $I_{tr} = 4\,A$. A comparable situation to the case $I_{tr} = 3\,A$ was observed. The 'induced' peak reaches a maximum of $U_{peak} = 65\,\mu V$. Subconsquently, the current monotonously decreases to in accordance with the decreasing magnetic field $B(t)$.*

In the third case of $I_{tr} = 6\,A$, the observed voltage drop is more pronounced in comparison to previous shown results. The value of the previously described induced peak increases to $U_{peak} = 100\,\mu V$. In contrast to the other discussed cases, the voltage signal further increases and reaching a 'main' peak of $U_{max} = 200\,\mu V$ at $t = 380\,ms$. Again, as the flux density decreases, the observed voltage drop decreases simultaneously.

This 'main' peak is resulting from dissipative current ($I_{tr} > I_c$) in the region of highest magnetic field .

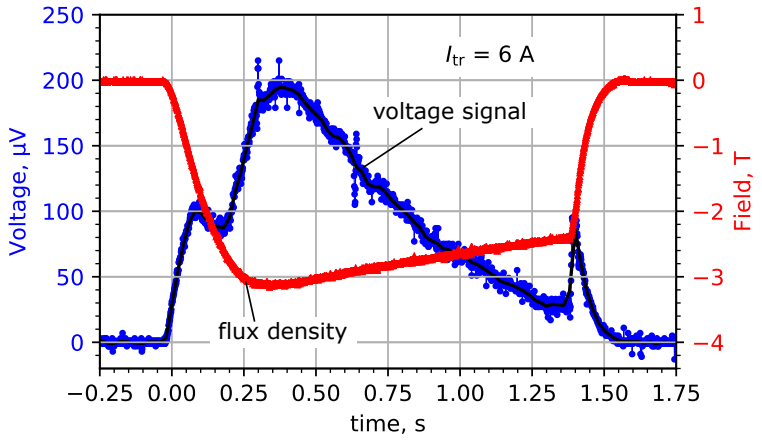

Figure 5.9 – *Magnet pulse with* 3 T *electromagnet and a tape load of* $I_{tr} = 6$ A. *After the induced peak, a 'main' peak of* $U_{max} = 200\,\mu V$ *appears at* $t = 380$ ms. *This peak is resulting from dissipative current in the region of the highest magnetic field.*

A detailed look on the timescale shows a delay between the instant of maximum field B_{max} and the instant of maximum voltage U_{max} in the range of ~ 30 ms. This is caused by minor heat diffusion that slightly extends the dissipative zone formed in the tape in the inhomogeneous field. This effect is small even at high induced voltages up to 900 µV due to the drastically reduced critical currents in the magnetic field. Inside the sample, the generated Joule's heat can be estimated to be up to $P = 18\,\mathrm{mW\,cm^{-2}}$.

The cooling capacity of liquid nitrogen on tapes per surface unit is assumed to be $P_{cooling} = 8\,\mathrm{W\,cm^{-2}}$ [106]. In table 5.2 the ratio between generated heat in the sample and cooling capacity of the liquid nitrogen reservoir is estimated.

Quantity	Unit	Value
$B_{\max}$	T	3
$I_{\mathrm{tr,max}}$	A	8
$U_{\max}$	μV	900
Surface per tape-cm S	cm^2	0.4
P	mWcm^{-2}	18
P/P_{cooling}		0.225 %

Table 5.2 – *Estimated power dissipation in the experimental setup with inhomogeneous fields. The cooling power P_{cooling} is assumed to be* $8\,\mathrm{W\,cm}^{-1}$ *and it is shown that the generated Joule's heat P is easily compensated by the liquid nitrogen reservoir even in cases of high dissipated voltage up to* 900 µV.

The influence of thermal effects seems therefore negligible even in case of a highly dissipative regime.

In the next step, the applied transport currents were increased to 8 A and the total voltage response of the tape in the field of the pulsed electromagnet was measured and compared to the calculations from the EAA approach. Thereby the voltage contact separation of 10 cm defined the limits of the integration of the electric field. For the EAA modeling, experimental values of the flux density distribution $B(x)$ were used. The integral expression of the voltage response was calculated using equation (24), yielding

$$U_{\mathrm{int}} = \left(\frac{1\mu\mathrm{V}}{1\mathrm{cm}}\right)_{\mathrm{cr}} \cdot \int_{-5}^{5} \left[\frac{I_{\mathrm{tr}}}{8.5}(\bar{B}(x)+0.01)^{+(0.3+0.2\cdot\bar{B}(x))}\right]^{n(\bar{B}(x))} \mathrm{d}x. \tag{28}$$

The parameters have been already explicitly written in equation (28), where $\bar{B}(x)$ denotes the experimental values of $B(x)$, divided by 1 T. The integration was repeated for values of $I_{\mathrm{tr}} = 4$ A, 6 A and 8 A. The n-value was calculated as before (equation (22)) using the explicit values $\left[15 + 0.2/(\bar{B}(x)+0.02)\right]\exp(-0.245\bar{B}(x))$. The parameter I_0 was set to $I_0 = 8.5$ A.

Figure 5.10 shows the calculated voltage response for different transport currents as the black lines. For comparison, experimentally determined values are introduced as data points, where the case $I_{\mathrm{tr}} = 8$ A is shown as blue diamonds, $I_{\mathrm{tr}} = 6$ A as orange squares and the case $I_{\mathrm{tr}} = 4$ A is denoted as green circles. The voltage response decreases by two orders of magnitude during the decreasing field from 3 T to 1 T.

For the cases $I_{tr} = 6\,A$ and $8\,A$ the voltage is exceeding the critical voltage of $10\,\mu V$ for a standard criterion of $1\,\mu V\,cm^{-1}$ significantly. Because of reasonable agreement between the experimental values and the predicted ones, even in the high dissipative regime, it is expected that no additional effects influence the superconducting behavior [100].

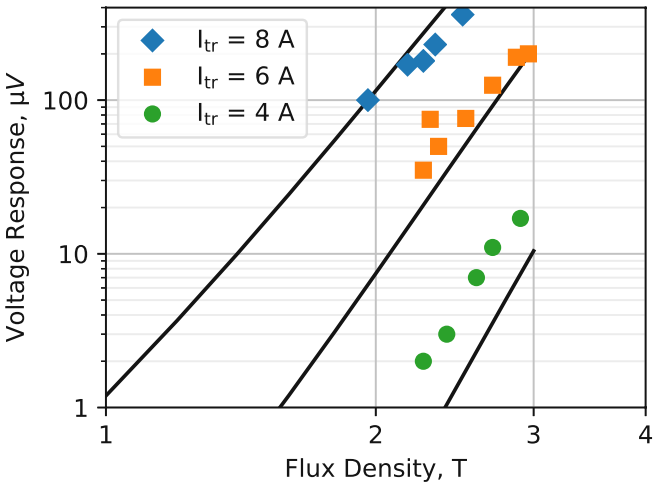

Figure 5.10 – *Comparison of modeled integral voltage response (black solid lines) and experimental values (data points) for transport currents $I_{tr} = 4\,A$, $6\,A$ and $8\,A$. This result is published in [100].*

6

Dynamic Tape Scans

This chapter deals with the implementation of the M-Scan method and presents results of several scans of different tapes with lengths up to 100 m. The tapes were normally exhibiting double disordered tape structure but one tape scan was also performed for a tape exhibiting a standard structure. In the beginning of this chapter the critical current determination in the frame of the EAA model is described.

In comparison to the tests in previous chapters, the tapes were measured with 'dynamic' four probe contacts of the M-Scan device and the feasibility of this method is shown.

6.1 M-Scan Critical Current Determination

The objective of the M-Scanner is the assessment of the critical current $I_c(x)$ in a magnetic field with a flux density of 2.61 T. During the scan procedure, the tape is loaded with a constant transport current $I_{tr} > I_c$ when continuously translated through the measurement stage. The corresponding voltage drop is directly measured on the moving tape.

In the following sections, considerations about the determination of the critical current from the measured voltage signal are described and discussed.

6.1.1 Influence of Edge Regions of the Magnetic Field

Modeling of the electric field and the voltage response between the voltage contacts of a sample exposed to a magnetic field with inhomogeneous flux density distribution $B(x)$ was described and discussed above in chapter 4 and experimentally confirmed

in the chapter 5. The expression of the voltage response in homogeneous fields (see equation (22)) is the root of I_c determination in M-Scan. This general expression (22) is modified as an integral expression for arbitrary field distributions $B(x)$ yielding

$$U_{\mathrm{int}}(I_{\mathrm{tr}}) = \left(\frac{\mathrm{d}U}{\mathrm{d}x}\right)_{\mathrm{cr}} \int_{-\frac{\Delta x}{2}}^{\frac{\Delta x}{2}} \left(\frac{I_{\mathrm{tr}}}{I_{\mathrm{c}}(B(x))}\right)^{n(B(x))} \mathrm{d}x. \tag{29}$$

In this equation, the integration is done along a path with length Δx which denotes the distance between the voltage contacts and with $x = 0$ at the center between the voltage contacts. In real measurements, the tape is loaded with a pre-determined transport current I_{tr} and the voltage drop U_{int} between the voltage contacts is measured during tape translation. The recorded voltage response is related to I_c.

However, as it was previously reported for the magnetic field of the 3 T pulsed electromagnet in section 5.2, the measured voltage along the sample dropped overwhelmingly in the center of the magnet, where the magnetic field exhibited its highest flux density. The generated electric field exceeded the electric field elsewhere up to 8 orders of magnitude. In other words, although the voltage contacts were separated by 10 cm in this setup, the main voltage response occurred practically only along the central region of maximum flux density inside the pulsed electromagnet.

This result is applied to the specific case of the permanent magnet assembly as well. Only the electric field generated within the 4 cm long 'plateau-zone' in the center of the permanent magnet is therefore considered to practically cause a voltage drop. Within this plateau-zone Δx_{m}, the field is sufficiently homogeneous and denoted with B_{m}.

Nevertheless, the voltage drop U_{int} within $\Delta x_{\mathrm{m}} = 4\,\mathrm{cm}$ is influenced by the field gradients at the edges of the 'plateau-zone'. The impact of these 'edge zones' is estimated in the following by splitting the homogeneous field zone Δx_{m} into a sum of (i) a 'central', homogeneous field region $\Delta x_{\mathrm{m}'}$ and (ii) edge regions $\Delta x_1 = \Delta x_2$.

This was done by adapting the integral in equation (29) to a sum along the zones $\Delta x_{\mathrm{m}'}$ and $\Delta x_1 = \Delta x_2$ which is written in equation (30). In the permanent magnet flux density distribution, the length of the central flux zone $\Delta x_{\mathrm{m}'} = 3.68\,\mathrm{cm}$ and the correction terms of edge regions with length $\Delta x_1 = \Delta x_2 = 0.16\,\mathrm{cm}$. It follows immediately $\Delta x_{\mathrm{m}'} + \Delta x_1 + \Delta x_2 = \Delta x_{\mathrm{m}} = 4\,\mathrm{cm}$.

$$U_{\mathrm{int}} = \left(\frac{\mathrm{d}U}{\mathrm{d}x}\right)_{\mathrm{cr}} \left[\Delta x_{\mathrm{m}'} \left(\frac{I_{\mathrm{tr}}}{I_{\mathrm{c}}(B_{\mathrm{m}})}\right)^{n(B_{\mathrm{m}})} + \int_{\Delta x_1} \left(\frac{I_{\mathrm{tr}}}{I_{\mathrm{c}}(B_1(x))}\right)^{n(B_1(x))} \mathrm{d}x + \int_{\Delta x_2} \left(\frac{I_{\mathrm{tr}}}{I_{\mathrm{c}}(B_2(x))}\right)^{n(B_2(x))} \mathrm{d}x\right] \tag{30}$$

The parts of the sum of equation (30) were solved separately and the terms with Δx_1 and Δx_2 put in a ratio to the total voltage drop U_{int} in order to determine their

relative impact. The critical current for B_m and $B(x)|_{\Delta x_1} = B(x)|_{\Delta x_2}$ in equation (30) was modeled using the previously derived expression for the critical current $I_c = I_0 \cdot (\bar{B}(x) + \delta)^{-\alpha_0 + \beta \bar{B}(x)}$ (see equation (20)) for two cases of I_0, namely $I_0 = 8.5\,\mathrm{A}$ and $I_0 = 10\,\mathrm{A}$.

The results of the calculation are listed in table 6.2 for the samples with lower current $I_0 = 8.5\,\mathrm{A}$ and in table 6.1 for the initial case with $I_0 = 10\,\mathrm{A}$. Both calculations, the edge regions (Δx_1 and Δx_2) and the drop along the central region $\Delta x_{m'}$ were performed for different transport currents from $I_{tr} = 5\,\mathrm{A}$ to $7\,\mathrm{A}$.

All values of the quantities $I_c(B_m)$, $n(B_m)$, $I_c(B_1(x)) = I_c(B_2(x))$ and $n(B_1(x)) = n(B_2(x))$ were calculated from the EAA parameters for double disordered tapes and values of B_m, $B(x)|_{\Delta x_1}$ and $B(x)|_{\Delta x_2}$ from the measured flux density distribution $B(x)$ of the permanent magnet. It follows from the calculations, that the edge regions yield an impact of ~3 % to 4 % to U_{int} along the homogeneous flux zone Δx_m and have similar values for both cases $I_0 = 8.5\,\mathrm{A}$ and $I_0 = 10\,\mathrm{A}$.

I_{tr} ($I_0 = 10\,\mathrm{A}$)	5 A	5.5 A	6.0 A	6.5 A	7.0 A
$U_{int}(\Delta x_{m'})$, µV	5.7	12.3	24.8	47.3	86.1
$U_{int}(\Delta x_1 = \Delta x_2)$, µV	0.97	0.22	0.46	0.92	1.74
Impact of two edges, %	3.30	3.46	3.61	3.76	3.90

Table 6.1 – *Calculation of the impact of both edges Δx_1 and Δx_2 on the total voltage response $U_{int}(\Delta x_m)$. The relative impact increases with increasing transport current and is conducted for $I_0 = 10\,\mathrm{A}$.*

In comparison to the case $I_0 = 10\,\mathrm{A}$ the relative impact of both edges on U_{int} is higher for tapes with lower currents, $I_0 = 8.5\,\mathrm{A}$.

I_{tr} ($I_0 = 8.5\,\mathrm{A}$)	5 A	5.5 A	6.0 A	6.5 A	7.0 A
$U_{int}(\Delta x_{m'})$, µV	21.1	45.6	92.1	175.8	320.0
$U_{int}(\Delta x_1 = \Delta x_2)$, µV	0.39	0.89	1.88	3.73	7.05
Impact of two edges, %	3.58	3.75	3.91	4.07	4.22

Table 6.2 – *Calculation of the impact of both edges on the total voltage response $U_{int}(\Delta x_m)$. In comparison to the calculations with $I_0 = 10\,\mathrm{A}$, the relative impact for each transport current is higher in the case of $I_0 = 8.5\,\mathrm{A}$.*

In an ideal homogeneous field B_m along Δx_m, an impact of 8 % to U_int along the edge regions would be expected, since the spatial part of the edge regions is $^{0.32\,\mathrm{cm}}/_{4.0\,\mathrm{cm}} = 8\,\%$ of Δx_m. However, it follows from the previous considerations, that the calculated impact of 4 % at the edge regions is $\sim 50\,\%$ below the expected impact for the assumed ideal situation. Consequently, if an ideal homogeneous field along Δx_m is assumed, the modeled voltage response U_int is overestimated by $\sim 4\,\%$ compared to the voltage response in the 'real' field $B(x)$. However, first approximations of the critical current in this study assume the 'ideal' situation, as it is described in the following.

6.1.2 Selection of Transport Current

To extract the critical current from the voltage drop, equation (29) needs to be transformed to express I_c. The n-value can be obtained via the EAA approach (see equation (21)) or determined experimentally using a power law. Regarding the considerations above, the general expression is simplified when assuming the flux density distribution $B(x) = const. = B_\mathrm{m}$ along the central zone Δx_m and zero elswhere. In this case B_m is replacing the general $B(x)$ and the integral expression vanishes except along Δx_m where it yields:

$$I_\mathrm{c}(B) = I_\mathrm{tr} \cdot \left[\Delta x_\mathrm{m} \left(\frac{\mathrm{d}U}{\mathrm{d}x} \right)_\mathrm{cr} / U_\mathrm{int}(B_\mathrm{m}) \right]^{\frac{1}{n(B_\mathrm{m})}} \tag{31}$$

In this way, the summation of infinitesimal x-dependent voltage responses via integration in presence of x-dependent fields $B(x)$ is reduced to a simple power law in the region Δx_m.

The critical current I_c is evaluated by measurement of U_int and employing the determined n value in the exponent. However, the magnitude of the total voltage drop U_int can be controlled by the pre-selected constant transport current I_tr, which is feed into the tape.

Figure 6.1 shows the determination of I_c from $U_\mathrm{int}(I_\mathrm{tr})$ for a set of different transport currents I_tr in the range from 5 A to 7 A. Different curves of $U_\mathrm{int}(I_\mathrm{tr})$ are related to different transport currents. The curves were modeled using equation (31) employing a typical value of $n(2.61\,\mathrm{T}) = 8$ and $\Delta x_\mathrm{m} = 4\,\mathrm{cm}$. A horizontal dashed line indicates a nominal critical current of $I_\mathrm{c} = 5\,\mathrm{A}$ at 2.61 T. A wide range of voltage drops from 4 µV to 50 µV for the determination of I_c is expected. The crossing points of the curves with the horizontal dashed line indicate the associated voltage drop for each selected transport current at the nominally assumed $I_\mathrm{c} = 5\,\mathrm{A}$. Note that the voltage drop U_int in case of $I_\mathrm{tr} = 5\,\mathrm{A}$ is exactly 4 µV and hence giving the trivial result expected for the

$1\,\mu V\,cm^{-1}$ criterion along a 4 cm long path. Nevertheless, the wide range of U_{int} from which the critical current can be determined is visible in this figure.

Figure 6.1 visualizes, that the critical current I_c can be determined independently from a wide range of pre-selected transport currents I_{tr}. To find reasonable values of I_{tr} an initial current-voltage characteristics of a short representative sample of each tape is recorded prior to the scan. Using the typical criterion of $1\,\mu V\,cm^{-1}$ to determine the critical voltage, the critical current of the representative sample is determined. In the subsequent scan, a pronounced voltage signal is observed when the pre-selected transport current exceeds the critical current, $I_{tr} > I_c$. Typically I_{tr} is selected to exceed I_c by $\sim 30\,\%$.

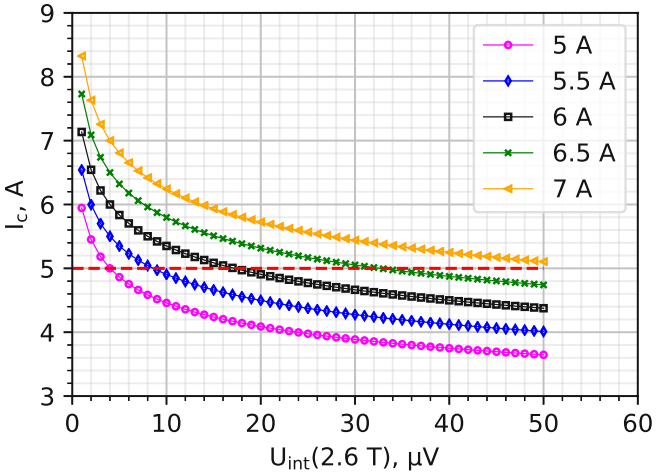

Figure 6.1 – *Critical current I_c dependence on measured voltage response U_{int} for given pre-selected transport currents I_{tr}. Crossing points of the horizontal red dashed line and the curves of U_{int} indicate the specific voltage drop for a sample with nominally $I_c = 5$ A for each pre-selected transport current I_{tr}.*

In the modeled curves of figure 6.1 a typical n-value of $n = 8$ is employed for the calculation of U_{int}. However, the B-field dependent n-value needs to be determined in real scans. This can be done on a representative sample in the beginning of the scan or by an alternation of the transport current from $I_{tr,1}$ to $I_{tr,2}$. The corresponding change in the voltage drop from $U_{int,1}$ to $U_{int,1}$ can be recorded and the n-value determined using the following expression which is immediately derived from the power law $U = (I/I_c)^n$.

$$n(x) = \frac{\ln\left(U_{int,1}(x)/U_{int,2}(x)\right)}{\ln(I_{tr,1}/I_{tr,2})}. \tag{32}$$

6.1.3 'Effective' Transport Current

Up to now, only silver capped samples were investigated and current flowing solely in the YBCO layer of the coated conductor was considered. However, in commercially produced coated conductors, the copper coating protects and stabilizes the conductor in case of dissipative fluctuations in the superconducting layer. Since the M-Scanner is purposely operated in a dissipative current regime, i.e. $I_{tr} > I_c$, it is expected, that parts of the applied transport current 'escape' from the YBCO and flow through the copper layer instead. However, for a precise critical current determination, the knowledge of the 'effective' transport current, i.e. the part of the transport current exclusively flowing through the YBCO, is required.

It is once again mentioned, that for the case of the pulsed 3 T electro magnet, the observed power dissipation of up to 18 mW cm^{-2} was easily transported away from the nitrogen coolant. It follows, that although the M-Scan is operated in dissipative regime, the comparably low applied transport currents limit the maximum dissipated power far below the amount which can be compensated by the coolant ($P_{limit} = 8\,\mathrm{W\,cm^{-2}}$).

In the following, a model to evaluate the current share in current in the copper layer I_{Cu} and current in the superconducting layer I_{YBCO} is briefly described. Therein, both layers are considered as being parallelly connected which is schematically shown in figure 6.2. Further, the thickness of the copper layer is neglected and no contact resistance is considered. Therefore, ideal current sharing is assumed.

The resistance of the copper R_{Cu} was characterized by extrapolating the voltage drop of a representative double disordered copper coated sample in a resistive T_c measurement to 77 K. The voltage drop of $U = 0.237\,\mu V$ appears along the 3 mm separated voltage pins at a current of 10 mA. The resistance R_{Cu} was then obtained by adapting the ratio $R = U/I$ for a 40 mm long tape piece, corresponding to the previously evaluated dissipative 'plateau-zone' Δx_m. In this way, the resistance of the copper coating R_{Cu} was calculated to be $R_{Cu} = 0.32\,m\Omega$. Figure 6.3 shows the plot of this measurement.

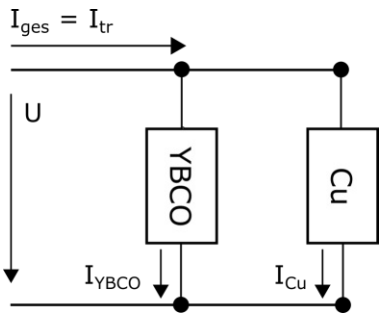

Figure 6.2 – *Scheme of the circuit of a parallel Cu and YBCO layer. The applied transport current $I_{tr} = I_{ges}$ splits in two parts, namely I_{Cu} and I_{YBCO}. From knowledge of R_{Cu}, I_{ges} and $U = U_{int}$, the current I_{YBCO} can be calculated.*

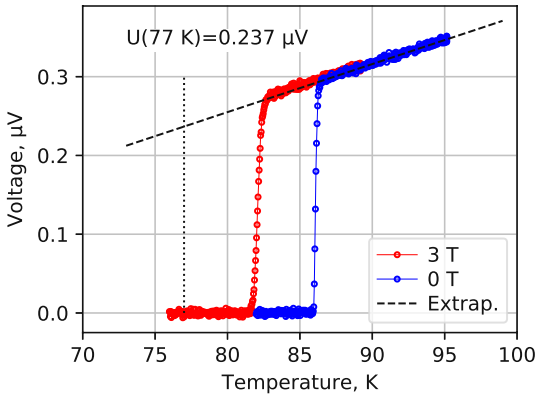

Figure 6.3 – *Calculation of the resistance in the copper layer along the coated conductor from resistive T_c measurement of a representative copper coated double disordered tape sample. The voltage drop between the 3 mm separated voltage contacts for a 10 mA current is extrapolated to 77 K and yields $U = 0.237\,\mu V$. The resistance along the 'plateau-zone' Δx_m is then calculated to be $R_{Cu} = 0.32\,m\Omega$.*

In this parallel circuit model, the resistance of the YBCO layer is calculated by

$$R_{YBCO} = \frac{1}{\frac{1}{R_{ges}} - \frac{1}{R_{Cu}}} \tag{33}$$

with $R_{ges} = U_{int}/I_{tr}$.
From the knowledge of R_{YBCO} the current parts I_{Cu} and I_{YBCO} can be determined as follows

$$\begin{aligned} I_{Cu} &= \frac{R_{YBCO}}{R_{YBCO} + R_{Cu}} \cdot I_{tr} \\ I_{YBCO} &= \frac{R_{Cu}}{R_{YBCO} + R_{Cu}} \cdot I_{tr} \end{aligned} \tag{34}$$

Below I_c, naturally no power dissipation is observed from which a transport current flow through the superconducting layer only is concluded. It follows from the according V-I characteristics of YBCO and Cu, that in dissipative regime, increasing transport currents yield a power-law based growth in the resistance of YBCO and a linear one for copper. Therefore, further increase of the applied transport current yields an increase of the relative amount of current flowing through the copper, described by the ratio of

I_{Cu}/I_{tr}.

The presented ideal model of two parallel conductors is a very rough approximation. In a more realistic consideration, the two conductors are in permanent interchange of current due to the low interfacial resistance. Detailed analysis can be performed by a current interchange model, which is discussed in e.g. [107, 108, 109].

6.2 Scan 1 - Implementation of M-Scan

In the following section, results of multiple 2 m scans of tape #T-1 with the M-Scan device are presented. For these scans, the pre-selected transport current was varied between 4 A to 6 A and the voltage drop was recorded for each case.

6.2.1 Tape Preparation

Tape #T-1 has a copper surface and was selected as test tape with a rather large I_c-inhomogeneity. Three defects were introduced into the first part of #T-1 reaching from $x_0 = 0\,\text{cm}$ to $x = 1.25\,\text{m}$. The first defect (D1) at $x_1 = 0.25\,\text{m}$ was introduced with a punching tool of 2 mm diameter, fully perforating the tape including the substrate. For introduction of defect (D2) at position $x_2 = 0.75\,\text{m}$ the superconducting layer was removed on a square shaped area with dimensions $2 \times 2\,\text{mm}^2$ with a diamond scratch tool. Defect (D3) at position $x_3 = 1.25\,\text{m}$ is a perpendicular scratch introduced with the diamond scratch tool as well and has dimensions $0.5 \times 2\,\text{mm}^2$. The introduced defects are schematically depicted in figure 6.4. All three defects have a width of 2 mm and correspondingly a current-bypass width of 2 mm. In contrast to the defect D1, the copper layer on the bottom side of the tape is undisturbed for defects D2 and D3. As indicated in figure 6.4, the scan was performed along the arrow.

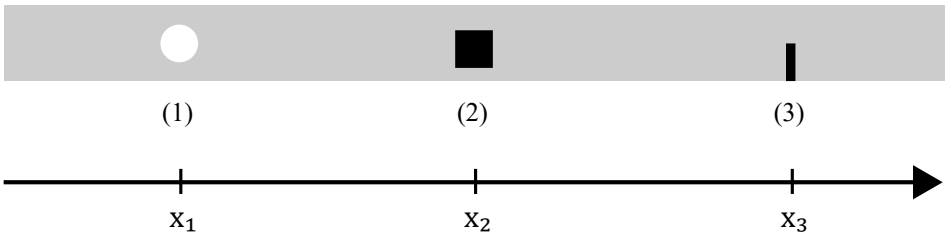

Figure 6.4 – *Schematic view of introduced artificial defects labeled (D1), (D2) and (D3) at distances $x_1 = 0.25\,\text{m}$, $x_2 = 0.75\,\text{m}$ and $x_3 = 1.25\,\text{m}$ from the staring point of the scan $x_0 = 0\,\text{cm}$. The scan is performed along the arrow.*

6.2.2 M-Scan of #T-1

Voltage Signal

In the first and second scan, the tape was scanned with a constant transport current of $I_{tr} = 4\,A$ the first time and with $I_{tr} = 5\,A$ the second one. Between both scans, the tape was rewound and each scan started at the same initial position $x_0 = 0\,cm$. Each time, the translation speed was selected to be $1\,mm\,s^{-1}$.

The voltage drop along the scanned distance with pre-selected transport currents $I_{tr} = 4\,A$ and $I_{tr} = 5\,A$ is shown in figure 6.5. In the case $I_{tr} = 4\,A$ the measured voltage is within a range of $0.02\,mV$ to $0.15\,mV$ whereas for $I_{tr} = 5\,A$ the voltage drop is between $0.1\,mV$ to $0.3\,mV$. The shape of both curves follow the same trend but obviously the amplitude of the observed periodic-like pattern along the scan is more pronounced for the case $I_{tr} = 5\,A$ than for $I_{tr} = 4\,A$. Defect-induced 'peaks' in the voltage response can be identified as a local increase of the measured voltage at the according positions of the defects. The width of these peaks is $4\,cm$ which is in agreement with the width of the $B_{max} = 2.61\,T$ central flux density zone $\Delta x_m = 4\,cm$.

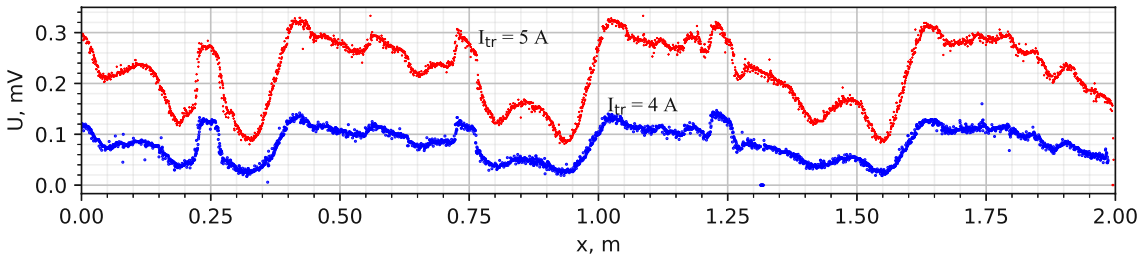

Figure 6.5 – *Scanned voltage response of tape #T-1 with* $I_{tr} = 4\,A$ *(blue) and* $I_{tr} = 5\,A$ *(red). The periodic-like pattern of both curves follow the same trend with a greater amplitude for the case* $I_{tr} = 5\,A$*. At positions* $x_1 = 0.25\,m$, $x_2 = 0.75\,m$ *and* $x_3 = 1.25\,m$ *voltage peaks induced by the artificial defects are observed.*

The depicted voltage represents the total voltage that was recorded between the voltage contacts, but dropped overwhelmingly within the 'plateau-zone' of highest field Δx_m. However, in a dissipative current regime, a part of $I_{tr} > I_c$ is expected to flow through the copper layer of the conductor whose amount I_{Cu} is calculated in the following. For accurate determination of the critical current I_{Cu} needs to be subtracted.

Parallel Currents

Following the considerations of section 6.1.3, the amount of current flowing through the copper layer is calculated. Since the voltage drop is considered to occur within the 4 cm long region Δx_{m} only, the resistance of the 'active' 4 cm long copper layer was previously found to be $R_{\mathrm{Cu}} = 0.32\,\mathrm{m\Omega}$ (see section 6.1.3 and figure 6.3). With $R_{\mathrm{Cu}} = 0.32\,\mathrm{m\Omega}$, the applied transport current I_{tr} and the measured voltage drop U_{int}, the current flowing in the YBCO layer I_{YBCO} was characterized by equations (33) and (34). I_{YBCO} is sometimes referred as 'effective' transport current in the following. Both parts I_{Cu} and I_{YBCO} are shown in figure 6.6 for the case $I_{\mathrm{tr}} = 5\,\mathrm{A}$.

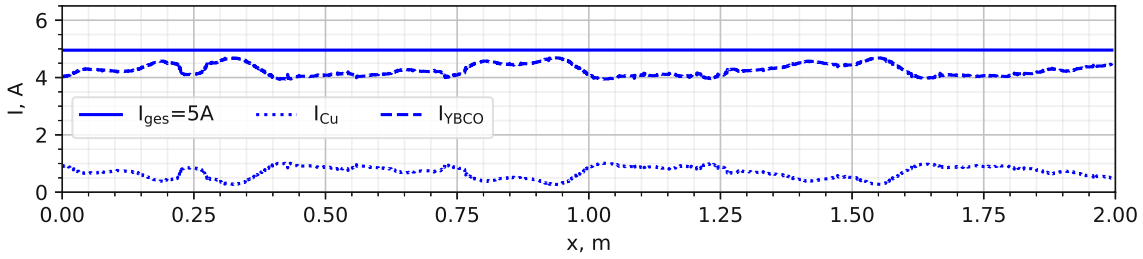

Figure 6.6 – *The superconducting YBCO and normalconducting Cu layer were modeled as parallelly connected resistors. Therefore, the applied transport current $I_{\mathrm{tr}} = I_{\mathrm{ges}}$ splits in two parts I_{Cu} (dotted line) and I_{YBCO} (dashed line). Both parts summed up return I_{tr} (solid line). For an applied transport current $I_{\mathrm{tr}} = 5\,\mathrm{A}$ up to 20 % of the current flows through the copper layer.*

More generally, the ratio of current flowing in the copper $I_{\mathrm{Cu}}/I_{\mathrm{tr}}$ was determined for all cases $I_{\mathrm{tr}} = 4\,\mathrm{A}$, $I_{\mathrm{tr}} = 5\,\mathrm{A}$ and $I_{\mathrm{tr}} = 6\,\mathrm{A}$. From a linear V-I characteristic of copper but power-law based V-I relation of YBCO, it is expected that the relative amount of I_{Cu} increases with increasing I_{tr}. This result is shown in figure 6.7. The relative amount of the total current flowing through the copper increases from 10 % to 30 % for increasing transport currents from 4 A to 6 A.

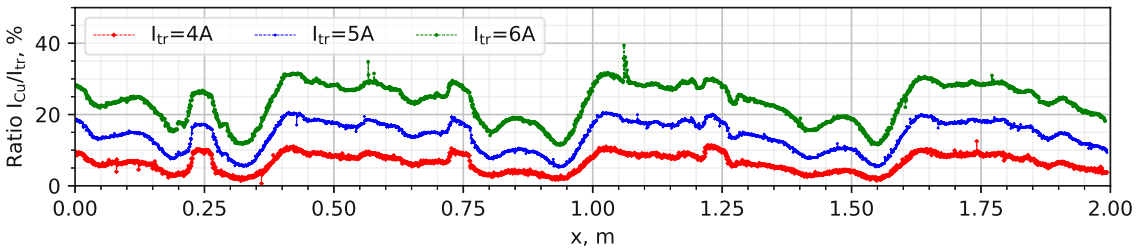

Figure 6.7 – *The ratio of current flowing in the copper is increasing with increasing applied transport current I_{tr}. For $I_{tr} = 4\,A$ up to 10 % of the total current are flowing through the copper layer, whereas this amount increases up to 30 % when $I_{tr} = 6\,A$ are feed into the tape.*

Critical Current Determination of #T-1

The previously discussed results about the shared currents are now implemented into the I_c determination. The critical current was determined for all cases of the applied transport current and all curves match. In the end, the determined critical currents are compared to measurements from a commercial Hall array scanner (TapeStar - THEVA) as well. For comparison reasons within the scope of this study, this was also done for a scenario where the parallelly flowing currents are neglected.

The n-value in the exponent of equation (31) for critical current determination was evaluated via equation (32) where the measured voltages for the cases $U_{int}(4\,A)$ and $U_{int}(5\,A)$ were employed. For the according currents two scenarios were evaluated. First, the according applied transport currents $I_{tr} = 4\,A$ and $I_{tr} = 5\,A$ were directly implemented to determine the n-value 'of the tape'. In the second scenario, only the according 'effective' currents I_{YBCO} were employed for determination of the 'effective' n-value. The results are shown in figure 6.8 and compared to the value $n = 7.954$ obtained from the EAA model (equation (21) in section 4.1.2).

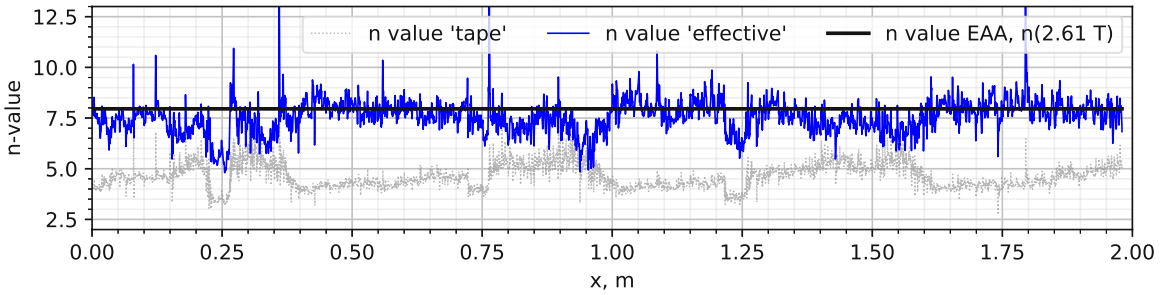

Figure 6.8 – *The n-value was calculated for different scenarios. The grey dotted line shows the n-value 'of the tape', i.e. its determination from the voltage drop and the applied transport current I_{tr}. On the other hand, the blue solid line shows the 'effective' n-value which is determined from the measured voltage drop and the 'effective' current parts I_{YBCO}. The n-value from the EAA model is $n = 7.954$ and shown as a black solid line.*

The samples for the determination of the n-values within the scope of the EAA model (see section 4.1) were silver capped and only comparably low voltages in the µV range were considered. Hence, current sharing could be generally neglected. The EAA modeled n-value is therefore regarded as 'intrinsic' n-value which is consequently in good agreement with the determined 'effective' n-value which was found around the value $n = 8$.

In the additionally evaluated 'tape'-n-value, the applied transport currents I_{tr} were directly employed in the n-value determination. An increased current share into the copper layer at higher voltages was not considered separately in this case which leads to a 'flattened' V-I characteristic followed by a reduction of the measured n. Therefore, the n-value 'of the tape' is only in the range $n = 4$-6.

'Imprints' of the defects D1 at $x = 0.25\,\mathrm{m}$ and D3 at $x = 1.25\,\mathrm{m}$ are visible in the 'effective' $n(x)$ curve. In the previous consideration, the current share was assessed as a whole along the 4 cm long 'active' zone of highest field in the permanent magnet which consequently determines the resolution width. However, due to the defect bypassing currents, the voltage drop is raised in a local spot much smaller than 4 cm. This yields to an correspondingly increased local copper current share, which is not resolved within the length of 4 cm. Therefore, current flow in the copper is locally underestimated which, analogously to the case where copper currents where completely neglected, leads to a reduced n-value.

Additionally, these defects come together with removed parts of the copper as well altering the copper resistance which was also not included in the model.

In the following, the critical current was determined with equation (31) employing the $n(x)$ value for all 'effective' transport currents of the cases of nominally applied I_{tr} =4 A to 6 A. The independence of the determined I_{c} on the pre-selected transport current is shown in figure 6.9. The critical current $I_{\mathrm{c}}(I_{\mathrm{tr}} = 6\,\mathrm{A})$ is depicted with blue crosses. Datapoints of the other cases $I_{\mathrm{c}}(I_{\mathrm{tr}} = 5\,\mathrm{A})$ and $I_{\mathrm{c}}(I_{\mathrm{tr}} = 4\,\mathrm{A})$ are represented by white diamonds and circles, respectively. The critical current $I_{\mathrm{c}}(I_{\mathrm{tr}} = 6\,\mathrm{A})$ was also evaluated employing the constant EAA value n=8. This approximation seems to be reasonable. However, deviations at the defects positions x_1, x_2 and x_3 are visible.

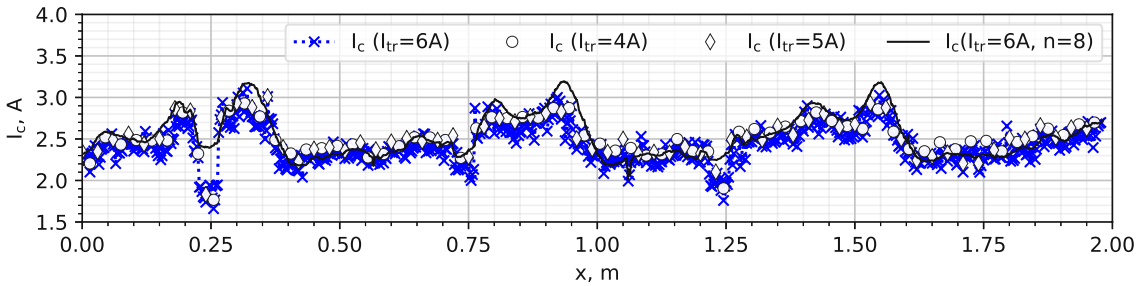

Figure 6.9 – *Evaluated critical current for three cases of $I_{\mathrm{tr}} = 6\,\mathrm{A}$ (blue crosses), $I_{\mathrm{tr}} = 5\,\mathrm{A}$ (white circles) and $I_{\mathrm{tr}} = 4\,\mathrm{A}$ (white diamonds). Evaluation of these currents employ $n(x)$ described in figure 6.8. The evaluated critical current is independent of the transport current. Additionally, the I_{c} value for $I_{\mathrm{tr}} = 6\,\mathrm{A}$ is shown for the EAA-calculated constant n-value of $n = 8$.*

Except at the defects positions, the determined critical current varies between 2.2 A to 3.0 A and has an average value of $I_{\mathrm{c}}^{\mathrm{avrg}} = 2.54\,\mathrm{A}$. At the positions $x_1 = 0.25\,\mathrm{m}$ and $x_2 = 1.25\,\mathrm{m}$, the critical current drops below a level of 2 A.

In a further analysis of the M-Scan result, the tape was additionally scanned with a commercially available Hall array scanner (TapeStar). In order to directly compare the critical current of the Hall array scanner with the evaluated critical current from the M-Scan both I_{c} curves were normalized to their over-all average value, where the average critical current evaluated from the TapeStar device were determined to be $I_{\mathrm{c}}^{\mathrm{avrg}} = 39\,\mathrm{A}$. The comparison of the relative critical currents is shown in figure 6.10. Blue circles represent the M-scan determined I_{c} which is compared to the TapeStar data (red line). Apart from the defect positions, which are treated separately, agreement of the critical current determined from the different scan devices is found. The conceptual case where parallel currents in the copper layer are neglected, i.e. $I_{\mathrm{Cu}} = 0\,\mathrm{A}$, is depicted as white

squares, which is accompanied with a larger misfit to the Hall array scan. The misfit increases with increasing applied transport current, hence consideration of parallelly flowing I_{Cu} is more crucial the further I_{tr} exceeds I_{c}.

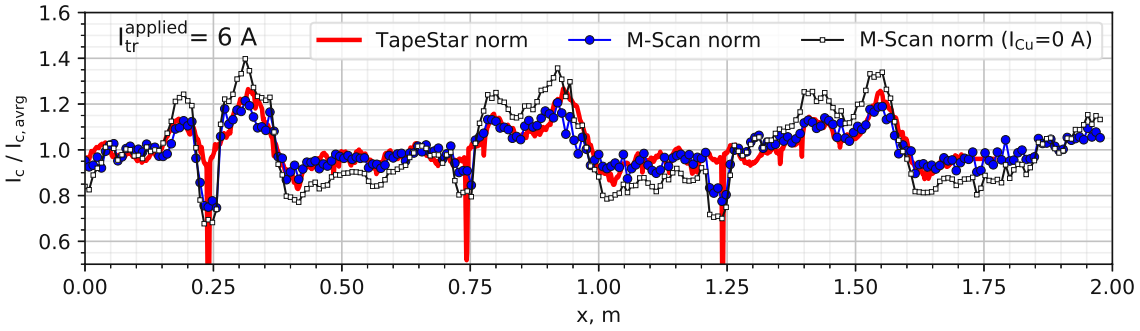

Figure 6.10 – *Comparison of the M-Scan I_{c}-curve with a commercial Hall array Scanner (TapeStar). In order to compare the magnitude of the critical currents, the curves were normalized by their corresponding averages. Blue dots represent the I_{c} curve obtained from M-Scan. The M-Scan and TapeStar data (red line) reasonably agrees with each other, which is different for the conceptual case of no current flow in the copper (white squares).*

Interpretation of Defect D1 with EAA

In the following section, the impact of defect D1 is investigated by analyzing the voltage response with the derived equations from the EAA approach (see section 4.1.3). In comparison to the simulation, described in 4.2.3, current sharing is now considered. The simulation and its assumptions are described in the following and the output is compared to the measured data.

The starting point of the simulation is again an array representing the tape. It is filled with values of the EAA parameter $I_0 = I_{\mathrm{c}}(1\,\mathrm{T})$ and a sub-array of values I_{D} corresponding to the defect's size and determined cross-sectional narrowing. Based on EAA equations, the voltage response between the voltage rollers is calculated by summing up the electric field along the modeled tape array in presence of the magnetic field $B(x)$ and for a given effective transport current I_{YBCO}. This procedure is iteratively repeated for each position of the defect between both voltage contacts i.e. simulating a transition of a defect through the magnet. Since the ratio $I_{\mathrm{Cu}}/I_{\mathrm{tr}}$ alters at the defect's position, the 'effective' transport current I_{YBCO} employed in the simulation is adapted according to the evaluated values from measurements. Finally, the simulated voltage drop $U(x)$ on a distance between the voltage contacts can be directly compared to the

measured voltage drop.

For the simulation a 'clean' tape with $I_0 = 6.2\,\mathrm{A}$ was assumed. The circular defect D1 with diameter of 2 mm was implemented in the modeled tape and the voltage response calculated during its simulated transition through the magnet.

The voltage drops are compared in figure 6.11. Panel (a) again shows the measured voltage drop for the applied transport currents I_{tr} =4 A to 6 A and in panel (b) the voltage response of the modeled defect is shown for the same cases.

In principle the voltage drop due to the defect is well predicted by the EAA (panel (b)), but however, the magnitude of the voltage drop doesn't match everywhere. This is due to the mismatching rough assumption of a 'clean' tape with homogeneously distributed $I_0 = I_{\mathrm{c}}(1\,\mathrm{T})$ for a test tape that in reality employs a rather high critical current inhomogeneity.

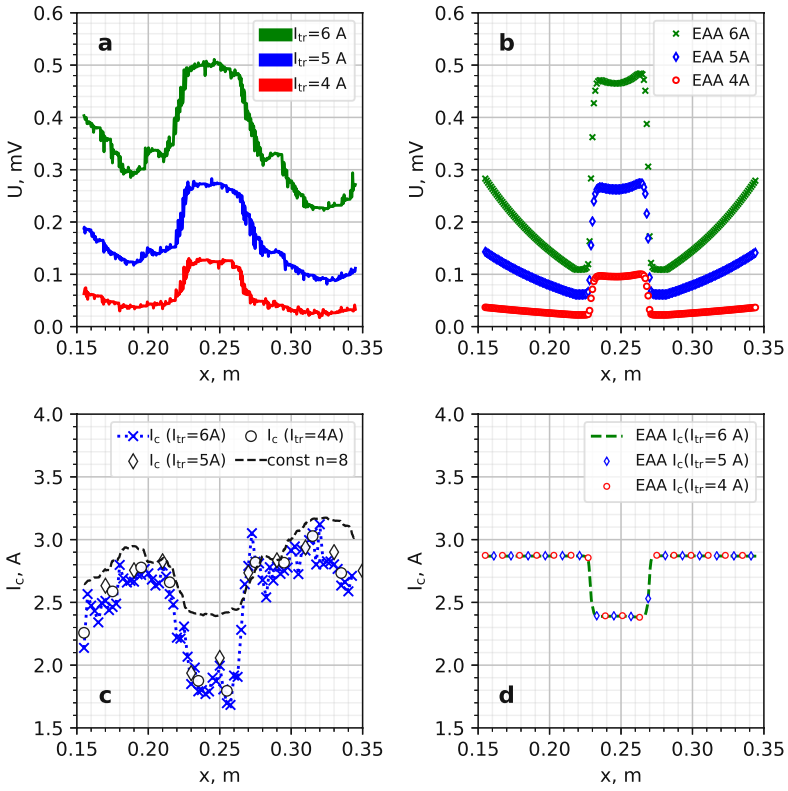

Figure 6.11 – *Comparison of the voltage response from measurement (panel a) and modeling with EAA approach (panel b). The critical currents obtained from measurements and simulation are shown in panels (c) and (d), respectively. As expected the critical current is independent of the transport current and in reasonable agreement with the measured data.*

The previously evaluated critical currents are shown in panel (c) and are compared for the simulated critical current in panel (d). As expected, the simulated critical current is independent of the applied transport current. For the simulation of I_c, the n-value obtained from the EAA equation was used. However, reasonable agreement of curves is found for I_c that was evaluated with constant n-value. Although the defect has a diameter of 2 mm and hence blocking 50 % of the current path, its impact on I_c in both curves is ∼15 % to 20 %. As it will be pointed out more comprehensively in section 6.4, this is a consequence of the $1/n$ exponent of the power law used for critical current determination. Roughly spoken, the determined critical current 'follows' the pattern of a voltage drop much slower than linear, namely with the n-th root.

The investigated artificial defect D1 was introduced with a punching tool fully perforating the tape. Therefore parts of the copper as well as the YBCO layer were removed. This means, that the copper resistance is changing at the defect's position which consequently alters the evaluated ratio of I_{Cu}/I_{tr}. In the presented scenario, the complete removal of tape material was not taken into account as such and a constant copper resistance was assumed for the whole tape.

Nevertheless, based on the described assumptions, reasonable agreement between the EAA-modelled curves and the measurement data is shown. The precision of the results on the EAA approach still can be further increased by a more comprehensive characterization of the tape at the defects position.

6.2.3 Hall Array Scan of #T-1

Finally, the Hall map from the Hall array scanner (TapeStar) is shown in figure 6.12. In the same way as the M-Scan, the Hall array scan was started at the initial position x_0 and scanned along the 2 m long segment of the tape. The magnetic map is built from induced superconducting shielding currents that hinder the 7 mT background field entering the tape. Darker areas therefore correspond to zones of higher shielding. Good agreement between the shape of the magnetic map and the behavior of the directly measured voltage drop of the M-Scan along the x-axis can be concluded.

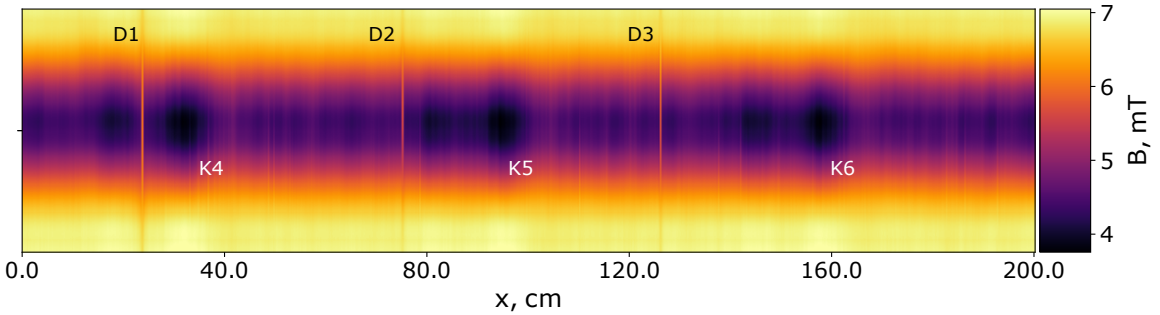

Figure 6.12 – *Magnetic map of scanned part of tape #T-1 obtained via Hall array scan. The external field of 7 mT is shielded towards the center of the tape by induced shielding currents in the tape indicated as darker areas. The vertical axis of this figure is aligned to the vertical axis of the tape. Knot-like shapes at repeated positions indicate a local pronounced shielding which can be consistently matched to zones of highest critical current and lowest voltage response, see figures 6.9 and 6.5, respectively. Defects D1-D3 can be identified as sharp vertical lines.*

The defects D1, D2 and D3 at the positions x_1, x_2 and x_3 can be identified as sharp vertical lines. Additionally, the typical I_c-inhomogeneity, observed in the determined critical current curve from the M-Scan can be matched the magnetic map of the Hall array scan. Repeated 'knot'-like shapes are indicated as K4, K5 and K6 of the magnetic map. These regions K4-K6 correspond to the regions with the highest measured critical current observed in the investigated segment of #T-1.

6.3 Scan 2 - Scan of 100 m Tape Class

In this section, a test of the M-Scan device for long tapes is described. The in total 94 m long tape #T-2 was scanned with the M-Scan device along its length and the critical current was determined. Before the scan, a set of artificial defect was introduced at the ends of the tape which served as identification marker to ensure a reproducible tape orientation in consecutive long-length scans.

The tape was additionally scanned with the Hall array scanner. A pronounced disagreement between the I_c-curves of both scans was found which was further investigated. It turns out that a longitudinal scratch has severe impact on the critical current when evaluated via Hall array scan, which is in contrast to the directly evaluated critical current of the M-Scan.

6.3.1 Critical current of #T-2

The critical current along the first 80 m of #T-2 was determined via the M-Scan device. The tape translation speed was selected to be $5\,\mathrm{mm\,s^{-1}}$ and the transport current was pre-selected to $I_{\mathrm{tr}} = 5.6\,\mathrm{A}$ and kept constant during the whole scan. The 'effective' transport current through the YBCO layer was determined analogously to scan 1 (section 6.2.2) by considering the current share through the copper layer. The resistance of the copper was again set to $R = 0.32\,\mathrm{m\Omega}$.

Prior to the scan, the current-voltage characteristic was determined at the initial position of the scan from which the n-value was derived to be 7.05. During the scan, the n-value was assumed to remain constant.

The determined critical current along the tape is shown in figure 6.13 and shows a repeating pattern of inhomogeneities. Additionally, the level of the critical current along the tape length can be split into different sections. From x =0 m to 10 m the magnitude of I_{c} is centered at a constant level of 3.9 A and is followed by a decreasing magnitude between x =10 m to 20 m. The critical current is at constant level of 3.2 A from x =20 m to 40 m and is increasing from x =40 m to 80 m again. The end-to-end average critical current is $I_{\mathrm{c}}^{\mathrm{avrg}} = 3.5\,\mathrm{A}$ at 77 K and 2.61 T.

The inhomogeneity of I_{c} around the average level of each section in a periodic-like pattern was also observed in the critical current obtained from the continuous Hall array scan (see figure 6.14).

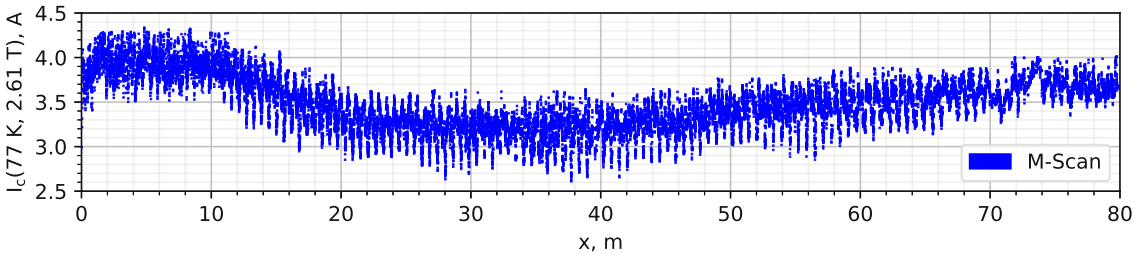

Figure 6.13 – *Critical current along the tape length of #T-2 determined via M-Scan. The transport current of* 5.6 A *was pre-selected and kept constant during the entire scan. Prior to the scan, the n-value was determined to be 7.05 and in first approximation assumed to remain unchanged. For the critical current evaluation, current through the copper layer was considered equally as shown in section 6.2.2. The average end-to-end critical current is* $I_{\mathrm{c}}^{\mathrm{avrg}} = 3.5\,\mathrm{A}$.

The same section of the tape was scanned via Hall array scan (TapeStar) as well and the determined critical current along the tape length shown in figure 6.14. The Hall

array scan scan was performed at 77 K in 'zero', i.e. 0.007 T, field and the evaluated average end-to-end value is $I_c^{avrg} = 59.3$ A. In contrast to the I_c-curve obtained from the M-Scan, a region with a pronounced degradation of the critical current is observed. This deviation was found along a length of 1.5 m from x =54 m to 55.5 m.

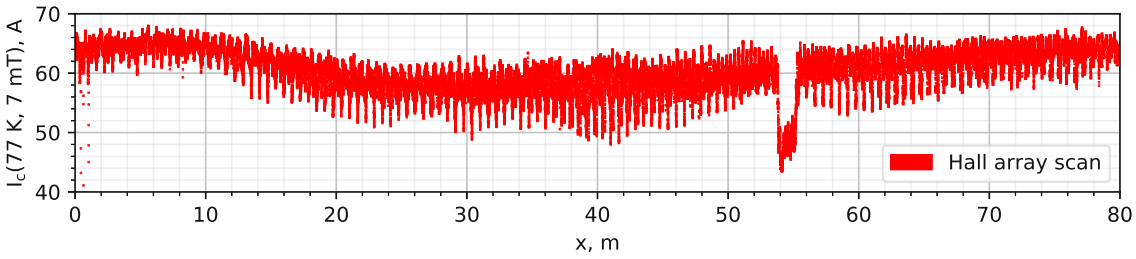

Figure 6.14 – *Critical current of the first* 80 m *of the tape #T-2 scanned with the Hall array scanner. The end-to-end average critical current is* $I_c^{avrg} = 59.3$ A. *In contrast to the directly measured critical current, a pronounced drop of* I_c *is observed on a* 1.5 m *long section between* $x = 54$ m *and* $x = 55.5$ m.

There was no difference of the tape surface found at the optical inspection of copper surface along the tape length from x =53 m to 56 m from the tape surface elswhere. In the next section, this zone of disagreement is investigated closer.

6.3.2 Defect Zone

After the localization of the defect zone with the Hall array scan, artificial defects that can be identified in the I_c-curves were introduced via the punching tool into the tape at $x = 53$ m and $x = 56$ m. This enabled a precise overlapping of I_c-curves of the following scans.

However, the defect zone (now localized between the visible position markers) was scanned again with both, the Hall array scanning tool and the M-Scanner. Technical problems were excluded, since the same results were reproduced in each corresponding scan. In the scope of the second M-Scan, the translation speed was slowed down to 1 mm s^{-1} and the applied transport current was set to $I_{tr} = 5.7$ A.

In the first step of the analysis, both I_c-curves were normalized by its end-to-end average value and plotted together in figure 6.15 where the relative impact of the disagreement on both curves is visible at once. Obviously, there is an I_c drop of ~ 30 % in the critical current obtained from the Hall array scan, which is not visible in the M-Scan. The inhomogeneous pattern of the critical current from the M-Scan simply continues in the defect zone.

In figure 6.15 a grey-shadowed zone indicates the position at the 'transition' from undisturbed to disturbed area where a sample #B20 with a length of 20 cm was cut for further analysis.

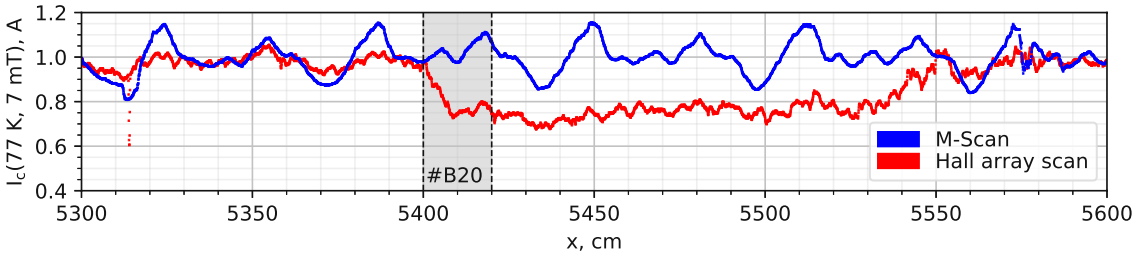

Figure 6.15 – *Normalized critical current determined by the M-Scan device (blue) and the Hall array scanner (red). The according end-to-end critical current was used for normalization. The critical current drops by about* $\sim 30\,\%$ *in the outlined region for the Hall array scan where for the M-Scan no such drop is recorded. For further analysis, the* 20 cm *long sample #B20 was cut at the indicated grey-shadowed position around the 'transition' from undisturbed to disturbed area in the tape.*

The magnetic map obtained from the Hall array scan is shown in figure 6.16. The disturbed area is visible as a region with a reduced shielding in the field profile. It is considered that in the disturbed area a longitudinal scratch in the center of the superconducting layer is blocking the transverse currents. This mitigates to build up the field profile and hence reducing the evaluated critical current. For direct measurements, the reduction of the tape's cross section is determining the impact of a defect on the critical current. The impact of a very thin longitudinal defect (like a scratch) on the critical current is therefore not visible in the M-Scan, especially when the width of the defect is orders of magnitude smaller than the width of the tape. In this case, the defect is practically not affecting the current bypassing width.

The width of a 1 µm thick scratch is three orders of magnitude smaller than the width of the tape and hence considered to be practically not influential in the direct measurements of the M-Scan.

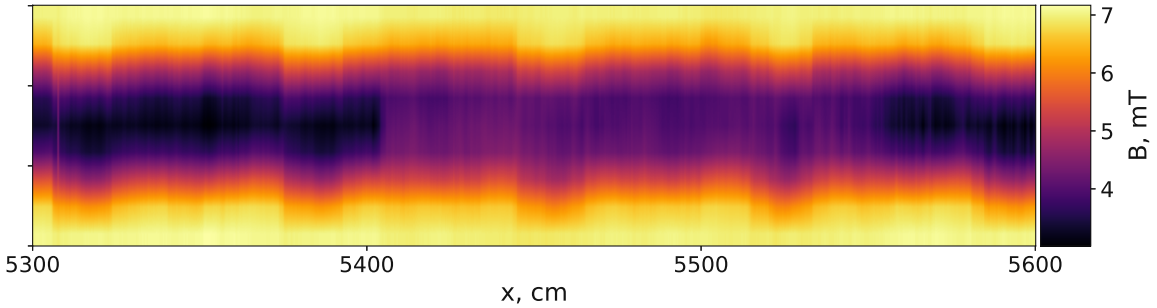

Figure 6.16 – *Field profile of the defect zone obtained from the Hall array scan. At the disturbed area a reduction in the field profile is observed. It is considered that this reduction originates in a longitudinal scratch that is blocking the transverse currents in the tape. This mitigates the building of the field profile and hence lowering the evaluated critical current.*

To confirm the consideration of a longitudinal scratch, further analysis was done. As already mentioned above, the tape #T-2 was cut at the indicated position in figure 6.15 at the 'transition' to the disturbed area and the sample #B20 with a length of 20 cm was used for further investigated. This sample #B20 is placed in a bath of liquid nitrogen and scanned with a scanning Hall probe microscopy device [110] with a resolution of 250 µm. The result of the scan, which was performed by my colleague Sigrid Holleis, is shown in figure 6.17.

The x-axis of the Hall map is aligned to the center of the sample. Obviously, the influence of a longitudinal defect blocks transverse currents and hence 'splits' the field profile in two parts as observed. This influence of profile-splitting is visible from $x = -50$ mm to 100 mm of the sample and becomes more pronounced as x increases. This matches the expectation of the field profile at the 'transition' from undisturbed to disturbed area.

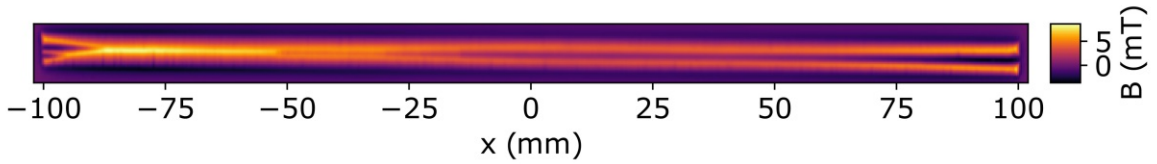

Figure 6.17 – *Hall map of the* 20 cm *long sample #B20 with a resolution of* 250 µm. *The x-axis is aligned to the center of the sample. According to the Hall map, the transverse currents are blocked at the disturbed zone by a longitudinal scratch. This yields a split of the field profile into two parts. Many thanks to my colleague Sigrid Holleis for carrying out this scan.*

To make the longitudinal scratch optically visible, a sub-sample of 1 cm length was cut of #B20 from 90 mm to 100 mm which was further investigated in an optical microscope. The copper surface and underlying silver layer were removed.

The copper layer was etched by placing the sample in a solution of sodium persulfate at 41 °C. The 2 µm thick silver layer was removed by a solution of ammonia and hydrogen peroxide. The bare surface of the remaining YBCO layer was then investigated in a light microscope which is shown in figure 6.18.
Two parallel thin scratches become visible in the superconducting film. Both scratches are separated by 350 µm and are considered to have a width of ~ 1 µm.

Figure 6.18 – *Picture of a representative position in the defect zone of tape #T-2 taken via light microscope. Copper and silver have been etched and two parallel,* ~ 1 µm *thick scratches, separated by* 350 µm *are visible in the YBCO film. This scratch blocks the transverse currents building up a disturbed field profile and hence changes the value of the critical current evaluated by Hall array scans.*

From this scan, two main conclusions can be drawn. First, the feasibility of long tape scans (up to 100 m) with the current M-Scan setup is confirmed. Secondly, a thin longitudinal scratch in the superconducting layer causes severe impact on the evaluated critical current from the Hall array scan, whereas the directly obtained I_c-curve from the M-Scan is practically not affected.

6.4 Scan 3 - Scans of Tape with Defects

In this section, the standard (i.e. non double disordered) tape #T-3 was analyzed with the M-Scan device. In the scope of this test, the standard tape was investigated with the EAA approach which was initially developed for double disordered tapes. The characteristic feature of the previously investigated tapes that employ a double

disordered structure is an abnormally high ratio (up to 10) of critical current densities measured at 4.2 K, 19 T and 77 K, self-field [75]. From the irreversibility line of double-disordered samples a low critical temperature $T_c(0\,T) = 85\,K$ to 86 K and $T_c(3\,T) = 81\,K$ to 82 K is observed. Therefore, the critical current at 77 K of the standard tape #T-3 is expected to be higher in comparison to the previously investigated double disordered tapes. In particular the critical current at 77 K and 2.61 T was found to be in the range of I_c ~8 A to 9 A.

6.4.1 Tape #T-3

The standard tape #T-3 is a ~10 m long tape with a laminated surface. In comparison to the typically used copper or silver surface, this surface is rather rough.

However, the tape was scanned along its entire length and closer investigated at four positions D1, D2, D3 and D4 where defects are degrading the critical current. At positions D1 and D4, the tape was perforated with the previously described punching tool but at position D4 the tape was perforated a second time within a short section of 2 cm. The diameter of each perforation is 2 mm, i.e. half of the tape width. In the following, these defects are called 'opening defect' for D1 and 'double opening defect' for D4. The origin of the defects D2 and D3 is unknown and therefore these defects are called 'natural'.

For the M-Scan procedure, the tape was scanned with a constant transport current of $I_{tr} = 8.5\,A$. The n-value was pre-determined to be $n = 7.59$ and set constant along the tape. The 'effective' transport current through the YBCO layer is determined by assuming a resistance of $R = 0.32\,m\Omega$ which was implemented for the I_c evaluation.

As it was performed for previous scans, tape #T-3 was scanned with the Hall array scanner as well. In comparison to double disordered tapes, the standard tape #T-3 employs a critical current at 77 K in 'zero' (i.e. 0.007 T) field of a higher level, calculated as end-to-end average critical current of $I_c^{avrg} = 109\,A$. In the M-Scan at 77 K and 2.61 T, a end-to-end averaged critical current of $I_c^{avrg} = 7.3\,A$ is observed. Figure 6.19 shows the I_c-curves along the tape for the Hall array scan (TapeStar - red) and the M-Scan (blue).

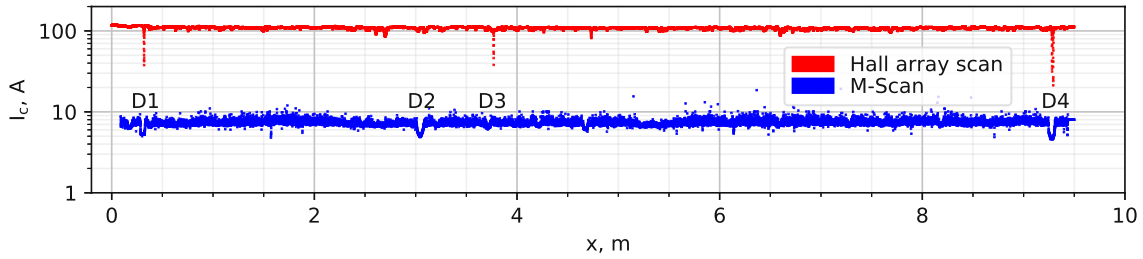

Figure 6.19 – *Scan of #T-3 with Hall array scan (red) and M-Scan (blue). The end-to-end averaged critical current is* $I_c^{avrg} = 109\,A$ *in the Hall array scan and* $I_c^{avrg} = 7.3\,A$ *for the M-Scan. Four defects D1, D2, D3 and D4 were identified and investigated closer. Defects D1 and D4 were introduced artificially, whereas D2 and D3 have unknown origin and therefore are called 'natural'.*

In this overview, the I_c degradation due defects D1 and D4 locally coincides in both curves whereas a defect (D2) is identified in the M-Scan curve only and vice versa the impact of a defect (D3) is visible in the TapeStar curve. These four spots are investigated closer and the expected voltage drop for the known defects D1 and D4 were calculated with the EAA approximation.

Known Defects D1 and D4

The measured and expected voltage drop of the known opening defect D1 and double opening defect D4 is shown in figure 6.20 in panel (a) and (b) respectively. For the modelling of the voltage response with the EAA approach the parameters $I_0 = 15\,A$ and an 'effective' transport current $I_{YBCO} = 8.1\,A$ were determined and employed in the simulation. The voltage drop exhibits a 'flat-hat' profile (panel a) and a 'double flat-hat' profile (panel b) at the according defects' positions. It can be seen, that both EAA predictions are in good agreement with the measured data. For the double opening defect D4, the second step 'doubles' the voltage in the profile which is due to the simultaneous presence of both defects within the field zone of 2.61 T. The height of each steps is $\sim 0.1\,mV$, yielding a total voltage response of $\sim 0.2\,mV$ for two defects within the field zone.

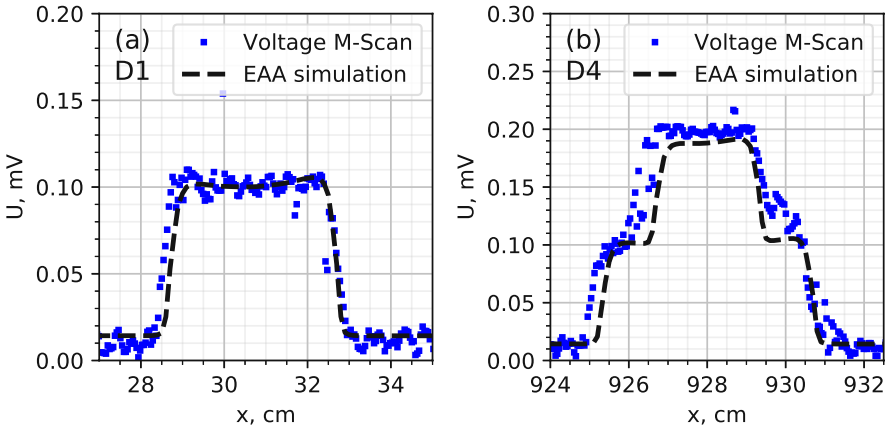

Figure 6.20 – *Voltage drop of measurement (points) and the predictions from the EAA approximation (dashed line) for the opening defect D1 (panel a) and the double opening defect D4 (panel b). The voltage drop of* 0.1 mV *for one defect inside the flux zone 'doubles' when both openings simultaneously are within the field zone during the scan (panel b).*

The impact of the defects on the Hall map from the TapeStar is shown in figure 6.21 for D1 and in figure 6.22 for D4. At the according positions each defect is resolved as vertical line where the shielding of the 7 mT background field is reduced.

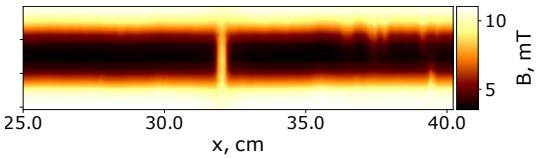

Figure 6.21 – *Hall map of the Hall array scan around defect D1. The opening defect is visible as vertical line where the shielding of the tape is reduced*

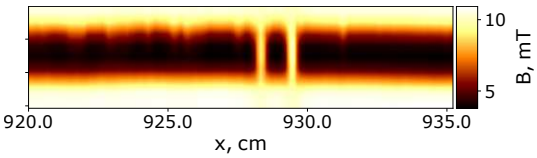

Figure 6.22 – *The magnetic data of D4 shows two lines for the double opening defects.*

The critical current at the defects' positions D1 and D4 was evaluated from the measured and the simulated voltage drop. The results of defect D1 is shown in panel (a) and the results of defect D4 in panel (b) of figure 6.23. In contrast to the previously discussed voltage response, the 'second step' in the double flat-hat profile of D4 is not of the same height as the 'first' step. In the purely EAA-modeled critical current, I_c degrades from initially 6.6 A by 1.4 A to $I_c = 5.2$ A and, as soon as the second defect enters the tape, the value drops a second time by 0.4 A to $I_c = 4.8$ A. This is expected from the applied power law to determine I_c since the $1/n$ exponent of the EAA equation (31) yields a nonlinear nth-root dependency on the inverse of the measured

voltage drop. This gives a 'slower' decrease of I_c for a corresponding increasing total voltage drop U_{int}.

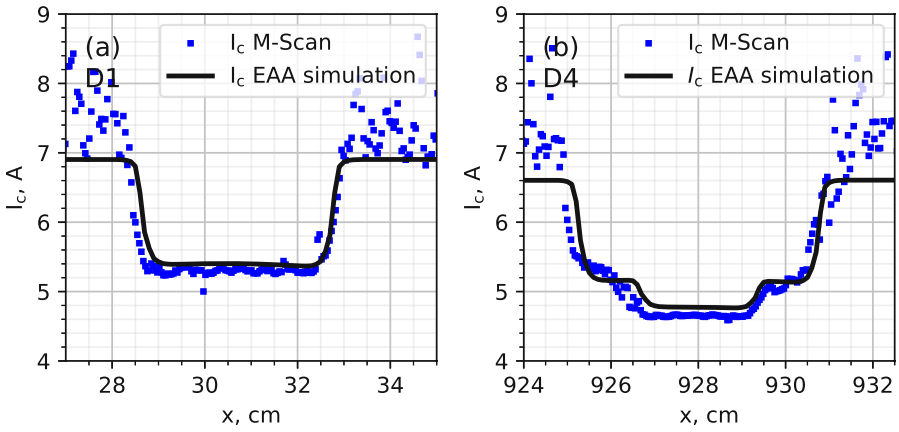

Figure 6.23 – *Determination of the critical current with the power law from measured data (blue dots) and fully EAA-simulated data (black solid line) for defect D1 (panel a) and defect D4 (panel b). Good agreement between the curves is found. The critical current degradation due to D4 shows a 'double flat hat' profile again, but with a smaller step size for the 'second step'. This follows from the $1/n$ exponent in the power law used for I_c determination.*

Unknown 'Natural' Defects D2 and D3

In contrast to the intentionally introduced opening defects D1 and D4, the impact of two identified 'natural' defects D2 and D3 on the critical current was evaluated. The analyzation of the critical current was performed with the aid of the TapeStar scanner.

Figure 6.24 shows the normalized critical current evaluated from the M-Scan (blue squares) and the Hall array scanner (TapeStar - red dashed line). As mentioned above, the end-to-end averages of the critical currents were determined to be $I_c^{avrg} = 109\,A$ for the TapeStar-I_c and $I_c^{avrg} = 7.3\,A$ for the M-Scan-I_c.

The normalized critical current around defect D2 is shown in panel (a) of figure 6.24. In the M-Scan the normalized critical current degrades to ~0.68 from its average level. In contrast to the opening defects, the profile of this defect in the I_c-curve is rounded. In the Hall array scan, however, a degradation to only to ~0.92 from its average value is observed.

The defect D2 is investigated closer by looking at the magnetic data which is shown in figure 6.25. At the position, where the degradation of I_c is observed in the M-Scan and Hall array scan, fringe-like imprints of both edges of the tape are visible. These

defects are perpendicular to the tape length and match to the spikes in the TapeStar curve at D2's position.

One possible reason for the disagreement between the relative impact of both curves is a local spot of reduced T_c. The dissipation of the constantly applied transport current additionally increases during the translation of the low-T_c spot through the magnetic flux zone of 2.61 T. This yields to an increased measured voltage drop which is inversely proportional to I_c. The possibility of D2 being a 'field dependent defect' can also be considered as some work was previously done in this direction e.g. by [58]

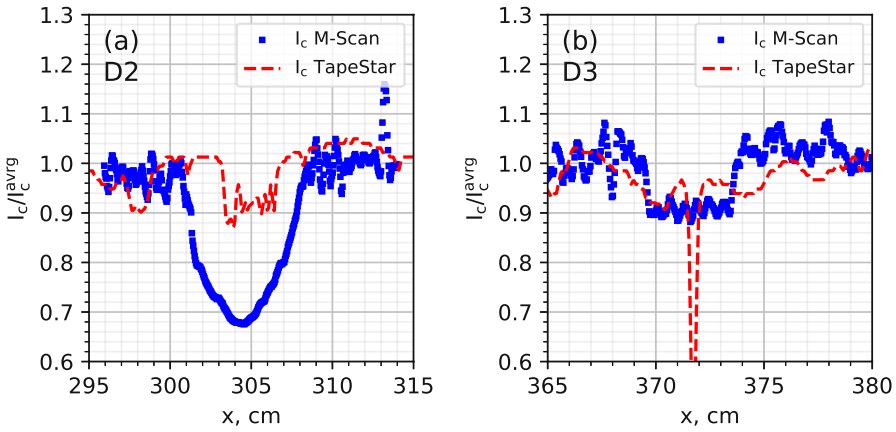

Figure 6.24 – *Normalized critical current around defect spots D2 (panel a) and D3 (panel b). For D2, the critical current degrades to ∼0.68 from its average level in the M-Scan. On the other hand, I_c reduces to ∼0.92 in the TapeStar curve. It is assumed that a spot of T_c reduction increases dissipation and hence degrading I_c. For D3 (panel b), a vertical crack or scratch in the YBCO layer is assumed to block longitudinal current flow.*

The I_c profile of the unknown defect D3 is shown in panel (b) of figure 6.24 and exhibits a flat-hat profile when measured with the M-Scan. The sharp drop of the relative I_c observed in the TapeStar indicates a very localized weak spot of the tape. The shape of impact on I_c is similar to that of D1.

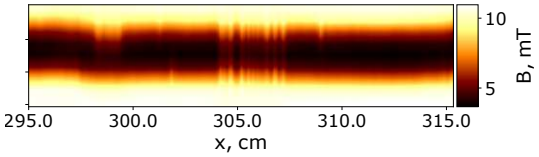

Figure 6.25 – *The magnetic map around defect D2 shows fringe-like imprints at the defects position. These imprints coincide with the spikes of the measured critical current with the TapeStar. The impact of this defect on the M-Scan is assumed to originate in a spot of lower T_c. It is expected, that dissipation of the constant transport current is increased when the 'low-T_c'-spot is entering the flux zone of* 2.61 T.

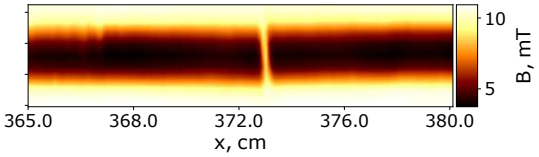

Figure 6.26 – *The magnetic map around defect D3 has similar magnetic response like defect D1. It is expected that a perpendicular defect such as a scratch or crack is blocking the longitudinal currents along the tape causing current sharing into the copper layer.*

In the magnetic map of the unknown defect D3, shown in figure 6.26, a sharp vertical line is visible, which is similar to the impact of D1 in the magnetic map. However, this defect is of 'natural' origin and it is expected to be a perpendicular crack or scratch in the YBCO layer which is interrupting the current flow in longitudinal direction of the superconductor causing additional current sharing to the surrounding copper layer.

7

Conclusions and Outlook

In general, the assessment of the critical current along the tape length is required to evaluate and control the tape's quality prior to its implementation into a technical application. This work describes the successful development and implementation of the M-Scan device for characterization of long-length coated conductors. The main feature of this machine is a permanent magnet with an aperture for tape throughput in which a 4 cm long flux density zone of 2.61 T at 77 K is generated. During the scan procedure, the tape is four-probe connected with contact rollers in a liquid nitrogen bath and loaded with a pre-selected constant transport current while the according voltage response is continuously measured.

This work was split in three major aspects which are shortly summarized below:

(a) In the first part of this work the concept of the main components of the M-Scan, such as the high-field permanent magnet, the low-noise contact rollers and ice-preventing gas flow heated feedthroughs as well as their construction and assembly were outlined.

(b) Secondly, a method to model the critical current along the tape from the continuously measured voltage response of the M-Scan was derived and named 'Extended Alpha Approximation' (EAA). Modeling of the electric field within the EAA approach between the voltage contacts predicted that the electric field practically occurs only within the flux zone of the magnet. Further, the calculated voltage response from the EAA approach was experimentally verified on different test benches.

(c) In the third part, performed tape scans with the assembled M-Scan are described. The tapes exhibited lengths up to 100 m were prepared with artificial defects.

The predictions of the voltage response from the EAA model on such tapes were verified with the experimentally obtained data of the M-Scan.

In the following paragraph, a few topics are outlined regarding the summarized points above.

Ad (a) Since the machine was built from scratch within the scope of this work, few points for future improvement are pointed out in the following.

Regarding a future prospect of commercial and competitive implementation of the M-Scan, a further increase of tape throughput through the scan device is desired. The currently longest tape of ∼100 m that was investigated within this study, was measured with a translation speed of 5 mm s^{-1}. For competitive usage, a 'benchmark' value for a tolerable scan duration could be equivalently set to the slowest process of tape fabrication. However, scanning a 1000 m long tape with a speed of 5 mm s^{-1} would require ∼55 h to 56 h. Nevertheless, an increase of scan speed of the M-Scan device is not limited per se and successful preliminary tests showed feasibility of scans with a translation speed of 10 mm s^{-1}. In the end, a scan speed of 50 mm s^{-1}, which is equivalent to 180 m h^{-1} is suggested for a final M-Scan implementation.

Another aspect is the control of tape driving by motors. In the currently developed stage of the M-Scan, two motors with constant angular velocity are driving the tape. This needs to be taken into account, since the tape is stacking on the coil, which means that increasing length of investigated tapes results in a higher stack inside the coil. The speed at the end of the stack for taking-off and picking-up the tape is therefore varying during a scan. The difference in the velocity on both ends of the scan is currently compensated by a roller with a movable axis. For tests in this work, the current setup is totally sufficient and the error of positioning was estimated to be about ∼1 % to 2 % (for 2 m and 10 m long tapes). In the ∼100 m scan, manual rewinding was done from time to time to balance different relative motor motions. However, improvements on the tape carrying mechanism are desired on the long term view. An elegant solution would be motors automatically adapting their corresponding angular velocity to a constant tape speed with a constant tape tension.

The distribution of the flux density of the 2.61 T permanent magnet limits the spatial resolution at the current stage of this method to 40 mm. However, higher resolution is desired in a routine characterization device. In principle this could

be achieved by alternative designs of the permanent magnet with a reduced zone of maximum flux density. Another approach is to process the derivative of the scanned voltage signal which is increased when a defect translates through the edge regions of the flux density profile.

Ad (b) The impact of the edge regions of the flux density zone of the 2.61 T permanent magnet on the critical current is estimated to be in a range of ∼4 % to 5 %. The calculation of I_c is simplified in the first performed tests by approximating a homogeneous flux zone within the magnet. In future considerations, if a 'narrower' flux density is forseen to increases the resolution limit of the scan, the increased relative impact of the edge zones needs to be taken into account.

Ad (c) The impact of defects on the voltage response is modeled and tested with the EAA approach. However, these artificially introduced defects in the tape surface are produced by hand via scratching with a hard spike tool or fully perforating the tape with a punching tool. Two aspects are pointed out for these methods: (i) precise reproducibility of defects is limited to the experimenter's dexterity and (ii) a full perforation of the tape as defect is not expected to occur 'naturally'. In next-step comprehensive studies on defects, development of a tool for reproducible defects is suggested. For defects, that remove parts of the copper layer as well, the reduced resistance of the copper layer at this position needs to be taken into account to predict the current sharing in copper and YBCO layer with higher precision.

Although the principle of critical current assessment along the tape length might seem to be a trivial task at the first glance, plenty of sometimes contrary requirements need to be solved to establish a well-working characterization tool. Challenges are coming from two sides, namely the engineering ones that addresses questions to the selection of appropriate materials for the assembly, mechanical stabilities of the components, possible issues due to thermal cycling et cetera. Fortunately, solutions on these topics are often already existing and the task transforms to their correct implementation to the own device. On the other hand, the produced data from the M-Scan needs to be adequately interpreted in order to produce suitable results. For this purpose the EAA model has been developed.

Typically, the characterization of superconducting tapes is routinely performed with the TapeStar (THEVA) device [59] which is based on a Hall array that scans tapes at 77 K and in 'zero' (7 mT) field. Another, well-established approach, is the YateStar

device [60] that directly measures tapes via V-I-curves on consecutive positions. With the M-Scan device a new four-probe scanning concept where the tape translates through a 2.61 T flux zone is introduced. Since TapeStar and M-Scan are based on different I_c assessment principles, caution is needed when the results are directly compared. Indeed, results of both devices on the critical current show both, agreement on parts on the tape as well as significant disagreement on other parts, especially at the position of defects. Analyzation of such disagreements have been started in this work with the conclusion of possible 'field dependent defects' or spots of lower T_c, which, of course, can be continued in the future.

Although it was not focused in this work, an ultimate goal is definitively the prediction of low-temperature (e.g. $T < 30$ K) performance of tapes from 77 K measurements. There are some hints discussed in the literature that correlations might exist at higher fields (e.g. in [111, 112, 58, 64]). Future studies in this direction might pick up some ideas of in-field scans that have been developed in this thesis.

However, it is shown in this work that the derived equations of the 'Extended Alpha Approximation' predict in good agreement the impact of specified defects on the measured voltage response from the M-Scan. The successful first tests in this work confirm the reliability of the M-Scan concept from which further research and development can be started.

Bibliography

[1] J. G. Bednorz and K. A. Müller. "Possible high Tc superconductivity in the Ba - La - Cu - O system". In: *Z. Phys. B* 64 (1986), pp. 189–193. DOI: 10.1142/9789814293365_0011.

[2] M. K. Wu et al. "Superconductivity at 93 K in a new mixed-phase Yb-Ba-Cu-O compound system at ambient pressure". In: *Physical Review Letters* 58.9 (1987), pp. 908–910. ISSN: 00319007. DOI: 10.1103/PhysRevLett.58.908.

[3] M. D. Bird et al. "Commissioning of the 36 T Series-Connected Hybrid Magnet at the NHMFL". In: *IEEE Transactions on Applied Superconductivity* 28.3 (2018), pp. 3–8. ISSN: 10518223. DOI: 10.1109/TASC.2017.2781727.

[4] A. J. Creely et al. "Overview of the SPARC tokamak". In: *Journal of Plasma Physics* 2020 (2020), pp. 1–25. ISSN: 14697807. DOI: 10.1017/S0022377820001257.

[5] B. D. Josephson. "Possible New Effects in Superconductive Tunneling". In: *Physics Letters* 1.7 (1962), pp. 251–253. DOI: https://doi.org/10.1016/0031-9163(62)91369-0.

[6] P. W. Anderson and J. M. Rowell. "Probable Observation of the Josephson Superconducting Tunneling Effect". In: *Career In Theoretical Physics, A (2nd Edition)* 10.6 (1963), pp. 230–232. DOI: 10.1142/9789812567154_0016.

[7] A. Johnson. "How Ford invented the SQUID". In: *IEEE Spectrum* 51.11 (2014), pp. 40–61. ISSN: 00189235. DOI: 10.1109/MSPEC.2014.6934931.

[8] H. Kamerlingh Onnes. "The liquefaction of helium". In: *KNAW, Proceedings* 11 (1909), pp. 168–185.

[9] H. Kamerlingh Onnes. "Investigations into the properties of substances at low temperatures, which have led, amongst other things, to the preparation of liquid helium". In: *Nobel Lecture* (1913), pp. 306–336.

[10] H. Kamerlingh Onnes. "Further experiments with liquid helium. On the change of electric resistance of pure metals at very low temperatures etc. The resistance of pure mercury at helium temperatures". In: *KNAW, Proceedings* 13 II (1911), pp. 1274–1276.

[11] D. v. Delft. "History and significance of the discovery of superconductivity by Kamerlingh Onnes in 1911". In: *Physica C* 479 (2012), pp. 30–35. ISSN: 09214534. DOI: 10.1016/j.physc.2012.02.046.

[12] J. L. MacManus-Driscoll and S. C. Wimbush. "Processing and application of high-temperature superconducting coated conductors". In: *Nature Reviews Materials* 6.7 (2021), pp. 587–604. ISSN: 20588437. DOI: 10.1038/s41578-021-00290-3. URL: http://dx.doi.org/10.1038/s41578-021-00290-3.

[13] J. Bardeen. "Superconductivity and Other Macroscopic Quantum Phenomena". In: *Physics Today* 43.12 (1990), pp. 25–31. ISSN: 19450699. DOI: 10.1063/1.881218.

[14] J. Bardeen, L. N. Cooper, and J. R. Schrieffer. "Theory of Superconductivity". In: *Physical Review* 108.5 (1957), pp. 1175–1204. DOI: 10.1201/9780429495700.

[15] W. Meissner and R. Ochsenfeld. "Ein neuer Effekt bei Eintritt der Supraleitfähigkeit". In: *Die Naturwissenschaften* 21.44 (1933), pp. 787–788. ISSN: 00281042. DOI: 10.1007/BF01504252.

[16] F. London and H. London. "Supraleitung und Diamagnetismus". In: *Physica* 2.1-12 (1935), pp. 341–354. ISSN: 00318914. DOI: 10.1016/S0031-8914(35)90097-0.

[17] A. B. Pippard. "An Experimental and Theoretical Study of the Relation between Magnetic Field and Current in a Superconductor". In: *Proc. R. Soc. Lond. A* 216.1127 (1953), pp. 547–568. ISSN: 0080-4630. DOI: 10.1098/rspa.1953.0040.

[18] V. L. Ginzburg. "On the theory of superconductivity". In: *Il Nuovo Cimento Series 10* 2.6 (1955), pp. 1234–1250. ISSN: 00296341. DOI: 10.1007/BF02731579.

[19] V. L. Ginzburg. "On Superconductivity and Superfluidity". In: *Nobel Lecture 2003* (2003), pp. 96–127. DOI: 10.1007/978-3-540-68008-6.

[20] A. A. Abrikosov. "On the Magnetic Properties of Superconductors of the Second Group". In: *Soviet Physics Jetp* 5.6 (1957), pp. 1174–1182.

[21] A. A. Abrikosov. "Type II superconductors and the vortex lattice". In: *Uspekhi Fizicheskikh Nauk* 174.11 (2003), pp. 1234–1239. ISSN: 00421294. DOI: 10.3367/ufnr.0174.200411f.1234.

[22] D. Cribier et al. "Study of the Superconductive Mixed State by Neutron-Diffraction". In: *Progress in Low Temperature Physics* Volume 5 (1967), pp. 161–180.

[23] U. Essmann and H. Träuble. "The direct observation of individual flux lines in type II superconductors". In: *Physics Letters A* 24.10 (1967), pp. 526–527. ISSN: 03759601. DOI: 10.1016/0375-9601(67)90819-5.

[24] U. Gottlieb et al. "Superconductivity in TaSi2 single crystals". In: *Physical Review B* 45.9 (1992), pp. 4803–4806.

[25] B. T. Matthias. "Empirical relation between superconductivity and the number of valence electrons per atom". In: *Physical Review* 97.1 (1955), pp. 74–76. ISSN: 0031899X. DOI: 10.1103/PhysRev.97.74.

[26] M. R. Beasley. "Overview of the Experimental History, Status and Prospects of HTS". In: *100 Years of Superconductivity*. Ed. by H. Rogalla and P. H. Kes. CRC Press, Taylor & Francis Group, 2012, pp. 213–222. ISBN: 978-1-4398-4646-0.

[27] V. L. Ginzburg. "Once again about high-temperature superconductivity". In: *Contemporary Physics* 33.1 (1992), pp. 15–23. ISSN: 0010-7514. DOI: 10.1080/00107519208219137.

[28] D. C. Johnston et al. "High temperature superconductivity in the LiTiO ternary system". In: *Materials Research Bulletin* 8 (1973), pp. 777–784. ISSN: 00255408. DOI: 10.1016/0025-5408(73)90183-9.

[29] A. W. Sleight, J. L. Gillson, and P. E. Bierstedt. "High-temperature superconductivity in the BaPb1-xBixO3 system". In: *Solid State Communications* 17.1 (1975), pp. 27–28. ISSN: 00381098. DOI: 10.1016/0038-1098(93)90253-J.

[30] H. Takagi et al. "High-Tc superconductivity of La-Ba-Cu oxides. II. –Specification of the superconducting phase". In: *Japanese Journal of Applied Physics* 26.2 A (1987), pp. L123–L124. ISSN: 13474065. DOI: 10.1143/JJAP.26.L123.

[31] P. W. Anderson. "The Resonating Valence Bond State in La2CuO4 and Superconductivity". In: *Science* 235.1 (1986), pp. 1196–1198.

[32] P. A. Lee, N. Nagaosa, and X. G. Wen. "Doping a Mott insulator: Physics of high-temperature superconductivity". In: *Reviews of Modern Physics* 78.1 (2006). ISSN: 00346861. DOI: 10.1103/RevModPhys.78.17.

[33] S. Uchida. *High Temperature Superconductivity - The Road to Higher Critical Temperature*. Springer S. Springe Japan 2015, 2015. ISBN: 978-4-431-55299-4. DOI: 10.1007/978-4-431-55300-7.

[34] H. Alloul et al. "Defects in correlated metals and superconductors". In: *Reviews of Modern Physics* 81.1 (2009), pp. 45–108. ISSN: 15390756. DOI: 10.1103/RevModPhys.81.45. arXiv: 0711.0877.

[35] M. Kazumi. "Introduction to d -wave superconductivity". In: *AIP Conference Proceedings*. Vol. 438. 1998, pp. 83–128. ISBN: 1563967898. DOI: https://doi.org/10.1063/1.56343.

[36] J. F. Annett. *Superconductivity, Superfluids and Condensates*. Great Clarendon Street, Oxford: Oxford University Press, 2004. ISBN: 978-0-19-850755-0.

[37] J. E. Hirsch, M. B. Maple, and F. Marsiglio. "Superconducting materials classes: Introduction and overview". In: *Physica C: Superconductivity and its Applications* 514 (2015), pp. 1–8. ISSN: 09214534. DOI: 10.1016/j.physc.2015.03.002. arXiv: 1504.03318.

[38] D. C. Larbalestier. "Critical currents and magnet applications of high-Tc superconductors". In: *Physics Today* 44.6 (1991), pp. 74–82. ISSN: 19450699. DOI: 10.1063/1.881305.

[39] G. Deutscher and K. A. Müller. "Origin of superconductive glassy state and extrinsic critical currents in high-Tc oxides". In: *Physical Review Letters* 59.15 (1987), pp. 1745–1747. ISSN: 00319007. DOI: 10.1103/PhysRevLett.59.1745.

[40] D. Dimos, P. Chaudhari, and J. Mannhart. "Superconducting transport properties of grain boundaries in YBa2Cu3O7 bicrystals". In: *Physical Review B* 41.7 (1990), pp. 4038–4049. ISSN: 01631829. DOI: 10.1103/PhysRevB.41.4038.

[41] G. W. Webb, F. Marsiglio, and J. E. Hirsch. "Superconductivity in the elements, alloys and simple compounds". In: *Physica C: Superconductivity and its Applications* 514 (2015), pp. 17–27. ISSN: 09214534. DOI: 10.1016/j.physc.2015.02.037. arXiv: 1502.04724.

[42] J. Muller. "A15-type superconductors". In: *Rep. Prog. Phys* 43 (1980), pp. 642–682. ISSN: 0028-0836. DOI: 10.1038/164203a0.

[43] G. R. Stewart. "Superconductivity in the A15 structure". In: *Physica C: Superconductivity and its Applications* 514.November 1953 (2015), pp. 28–35. ISSN: 09214534. DOI: 10.1016/j.physc.2015.02.013.

[44] Y. Kamihara et al. "Iron-Based Layered Superconductor La[O1 - xFx] FeAs(x)0.05-0.12) with Tc = 26 K". In: *Journal of the American Chemical Society* 130.11 (2008), pp. 3296–3297.

[45] Hideo Hosono et al. "Recent advances in iron-based superconductors toward applications". In: *Materials Today* 21.3 (2018), pp. 278–302. ISSN: 18734103. DOI: 10.1016/j.mattod.2017.09.006.

[46] C. V. Sundaram and T. S. Radhakrishnan. "Current trends in the development and applications of superconducting materials". In: *Bull. Mater. Sci.* 12.September (1989), pp. 225–244.

[47] P. Seidel, ed. *Applied Superconductivity - Handbook on Devices and Applications*. Weinheim, Germany: Wiley-VCH Verlag GmbH & Co. KGaA, 2015. ISBN: 9783527408320.

[48] D. C. Larbalestier and M. P. Maley. "Conductors from Superconductors: Conventional Low-Temperature and New High-Temperature Superconducting Conductors". In: *MRS Bulletin* 18.8 (1993), pp. 50–56. ISSN: 19381425. DOI: 10.1557/S0883769400037775.

[49] F. Debray and P. Frings. "State of the art and developments of high field magnets at the "Laboratoire National des Champs Magnétiques Intenses"". In: *Comptes Rendus Physique* 14.1 (2013), pp. 2–14. ISSN: 16310705. DOI: 10.1016/j.crhy.2012.11.002.

[50] Y. Shimomura and W. Spears. "Review of the ITER Project". In: *IEEE Transactions on Applied Superconductivity* 14.2 (2004), pp. 1369–1375.

[51] H. Shirai et al. "Recent Progress of the JT-60SA Project". In: *Nuclear Fusion* 57 (2017).

[52] T. Klinger et al. “Performance and properties of the first plasmas of Wendelstein 7-X”. In: *Plasma Physics and Controlled Fusion* 59.1 (2017). ISSN: 13616587. DOI: 10.1088/0741-3335/59/1/014018.

[53] L. Rossi. “The LHC superconducting magnets”. In: *Proceedings of the IEEE Particle Accelerator Conference* 1.July 2003 (2003), pp. 141–145. DOI: 10.1109/pac.2003.1288863.

[54] H. W. Lee, K. C. Kim, and J. Lee. “Review of Maglev train technologies”. In: *IEEE Transactions on Magnetics* 42.7 (2006), pp. 1917–1925. ISSN: 00189464. DOI: 10.1109/TMAG.2006.875842.

[55] K. Sawada. “Development of magnetically levitated high speed transport system in Japan”. In: *IEEE Transactions on Magnetics* 32.4 PART 2 (1996), pp. 2230–2235. ISSN: 00189464. DOI: 10.1109/20.508609.

[56] W. D. Markiewicz et al. “Design of a superconducting 32 T magnet with REBCO high field coils”. In: *IEEE Transactions on Applied Superconductivity* 22.3 (2012). ISSN: 10518223. DOI: 10.1109/TASC.2011.2174952.

[57] X. Hu et al. “An experimental and analytical study of periodic and aperiodic fluctuations in the critical current of long coated conductors”. In: *IEEE Transactions on Applied Superconductivity* 27.4 (2017). ISSN: 10518223. DOI: 10.1109/TASC.2016.2637330.

[58] L. Rossi et al. “Sample and length-dependent variability of 77 and 4.2 K properties in nominally identical RE123 coated conductors”. In: *Superconductor Science and Technology* 29.5 (2016). ISSN: 13616668. DOI: 10.1088/0953-2048/29/5/054006.

[59] S. Furtner et al. “Reel-to-reel critical current measurement of coated conductors”. In: *Superconductor Science and Technology* 17.5 (2004). ISSN: 09532048. DOI: 10.1088/0953-2048/17/5/037.

[60] J. Y. Coulter et al. “Position and magnetic field angle dependent Ic for long-length coated conductors”. In: *IEEE Transactions on Applied Superconductivity* 17.2 (2007), pp. 3394–3397. ISSN: 10518223. DOI: 10.1109/TASC.2007.898944.

[61] J. Y. Coulter et al. “Nondestructive investigation of position dependent ic variations in multi-meter coated conductors”. In: *IEEE Transactions on Applied Superconductivity* 19.3 (2009), pp. 3609–3613. ISSN: 10518223. DOI: 10.1109/TASC.2009.2019252.

[62] J. O. Willis, J. Y. Coulter, and M. W. Rupich. “N-Value analysis of position-dependent property variability in long-length coated conductors”. In: *IEEE Transactions on Applied Superconductivity* 21.3 PART 3 (2011), pp. 2988–2991. ISSN: 10518223. DOI: 10.1109/TASC.2010.2087372.

[63] S. Kim et al. “Development of high speed continuous transport critical current measurement system for long piece of HTS conductor”. In: *Physica C: Superconductivity and its Applications* 484 (2013), pp. 142–147. ISSN: 09214534. DOI: 10.1016/j.physc.2012.03.024.

[64] X. F. Li et al. “Reel-to-reel critical current measurement of REBCO coated conductors”. In: *IEEE Transactions on Applied Superconductivity* 27.4 (2017), pp. 10–14. ISSN: 10518223. DOI: 10.1109/TASC.2016.2640942.

[65] R. H. Bellis and Y. Iwasa. “Quench propagation in high Tc superconductors”. In: *Cryogenics* 34.2 (1994), pp. 129–144. ISSN: 00112275. DOI: 10.1016/0011-2275(94)90036-1.

[66] J. Schwartz. “Quench in high temperature superconductor magnets”. In: *WAMSDO 2013: Workshop on Accelerator Magnet, Superconductor, Design and Optimization; 15 - 16 Jan 2013, CERN, Geneva, Switzerland*. 2014, p. 9. DOI: 10.5170/CERN-2013-006.21. arXiv: 1401.3937.

[67] A. Usoskin et al. “Processing of long-length YBCO coated conductors based on stainless steel tapes”. In: *IEEE Transactions on Applied Superconductivity* 17.2 (2007), pp. 3235–3238. ISSN: 10518223. DOI: 10.1109/TASC.2007.900041.

[68] A. Usoskin and L. Kirchhoff. “In-Plane Texturing of Buffer Layers by Alternating Beam Assisted Deposition: Large Area and Small Area Applications”. In: *MRS Proc.* 1150 (2008). DOI: 10.1557/PROC-1144-LL16-04.

[69] A. Usoskin et al. “Large-area HTS-coated stainless steel tapes with high critical currents”. In: *IEEE Transactions on Applied Superconductivity* 11.1 III (2001), pp. 3385–3388. ISSN: 10518223. DOI: 10.1109/77.919789.

[70] A. Usoskin and H. C. Freyhardt. “YBCO-Coated Conductors Manufactured by High-Rate Pulsed”. In: *MRS Bulletin* August2004.May (2004), pp. 583–589.

[71] A. Rutt et al. “Ultrahigh-Speed Pulsed Laser Deposition of YBCO Layer in Processing of Long HTS Coated Conductors”. In: *IEEE Transactions on Applied Superconductivity* 26.3 (2016), pp. 3–6. ISSN: 10518223. DOI: 10.1109/TASC.2016.2536799.

[72] A. Usoskin et al. “Long HTS Tapes with High In-Field Performance Manufactured via Multibeam PLD with Dynamic Drum Concept”. In: *IEEE Transactions on Applied Superconductivity* 27.4 (2017). ISSN: 10518223. DOI: 10.1109/TASC.2016.2627799.

[73] A. Usoskin et al. “Long HTS Coated Conductor Processed via Large-Area PLD/ABAD for High-Field Applications”. In: *IEEE Transactions on Applied Superconductivity* 26.3 (2016), pp. 3–6. ISSN: 10518223. DOI: 10.1109/TASC.2016.2542253.

[74] A. Usoskin, H. C. Freyhardt, and H. U. Krebs. "Influence of light scattering on the development of laser-induced ridge-cone structures on target surfaces". In: *Applied Physics A: Materials Science and Processing* 69.7 (1999), pp. 823–826. ISSN: 09478396. DOI: 10.1007/s003390051539.

[75] D. Abraimov et al. "Double disordered YBCO coated conductors of industrial scale: High currents in high magnetic field". In: *Superconductor Science and Technology* 28.11 (2015). ISSN: 13616668. DOI: 10.1088/0953-2048/28/11/114007.

[76] U. Floegel-Delor et al. "Reel-to-reel copper electroplating on pulse laser deposition coated conductor". In: *IEEE Transactions on Applied Superconductivity* 21.3 PART 3 (2011), pp. 2984–2987. ISSN: 10518223. DOI: 10.1109/TASC.2010.2101031.

[77] U. Floegel-Delor et al. "Operation and experience of a 2 km coated conductor REEL-to-REEL copper pulse plating facility". In: *Journal of Physics: Conference Series* 507.PART 2 (2014), pp. 1–5. ISSN: 17426596. DOI: 10.1088/1742-6596/507/2/022006.

[78] U. Floegel-Delor et al. "Optimum design of copper stabilizer on coated conductors". In: *IEEE Transactions on Applied Superconductivity* 25.3 (2015), pp. 3–6. ISSN: 10518223. DOI: 10.1109/TASC.2014.2376776.

[79] A. Usoskin et al. "Long-length YBCO coated conductors for ultra-high field applications: Gaining engineering current density via pulsed laser deposition/alternating beam-assisted deposition route". In: *Superconductor Science and Technology* 32.9 (2019). ISSN: 13616668. DOI: 10.1088/1361-6668/ab2cba.

[80] H. Kobayashi et al. "Investigation of in-field properties of YBCO multi-layer film on PLD/IBAD metal substrate". In: *Physica C: Superconductivity and its Applications* 463-465.SUPPL. (2007), pp. 661–664. ISSN: 09214534. DOI: 10.1016/j.physc.2007.02.027.

[81] A. Usoskin et al. "Double-Disordered HTS-Coated Conductors and Their Assemblies Aimed for Ultra-High Fields: Large Area Tapes". In: *IEEE Transactions on Applied Superconductivity* 28.4 (2018), pp. 1–6. ISSN: 10518223. DOI: 10.1109/TASC.2018.2801348.

[82] A. L. Robinson. "Powerful New Magnet Material Found". In: *Science* 223.4639 (1984), pp. 920–922. DOI: DOI:10.1126/science.223.4639.920.

[83] M. Sagawa et al. "New material for permanent magnets on a base of Nd and Fe (invited)". In: *Journal of Applied Physics* 55.6 (1984), pp. 2083–2087. ISSN: 00218979. DOI: 10.1063/1.333572.

[84] J. F. Herbst and J. J. Croat. "Neodymium - iron - boron permanent magnets". In: *Journal of Magnetism and Magnetic Materials* 100 (1991), pp. 57–78. DOI: https://doi.org/10.1016/0304-8853(91)90812-O.

[85] J. Lucas et al. *Rare Earths Rare Earths Production and Use*. Elsevier, 2014, pp. 213–230. ISBN: 9780444627353.

[86] M. Kumada et al. "Development of 4 Tesla permanent magnet". In: *Proceedings of the IEEE Particle Accelerator Conference* 5 (2001), pp. 3221–3223. DOI: 10.1109/pac.2001.988064.

[87] *Neodymium Iron Boron Magnets*. URL: https://www.arnoldmagnetics.com/products/neodymium-iron-boron-magnets/ (visited on 09/02/2021).

[88] *Magnetische Kenndaten*. URL: https://www.magnet-shop.net/wissenswertes/kenndaten (visited on 09/02/2021).

[89] *Grades of Neodymium*. URL: https://e-magnetsuk.com/introduction-to-neodymium-magnets/grades-of-neodymium/ (visited on 09/02/2021).

[90] J. C. Mallinson. "One-Sided Fluxes — A Magnetic Curiosity?" In: *IEEE Transactions on Magnetics* 9.4 (1973), pp. 678–682. ISSN: 19410069. DOI: 10.1109/TMAG.1973.1067714.

[91] K. B. Baltzis. "The finite element method magnetics (FEMM) freeware package: May it serve as an educational tool in teaching electromagnetics?" In: *Education and Information Technologies* 15.1 (2010), pp. 19–36. ISSN: 13602357. DOI: 10.1007/s10639-008-9082-8.

[92] K. Halbach. "Design of permanent multipole magnets with oriented rare earth cobalt material". In: *Nuclear Instruments and Methods* 169.1 (1980), pp. 1–10. ISSN: 0029554X. DOI: 10.1016/0029-554X(80)90094-4.

[93] M. Kumada et al. "Three Tesla Magnet-in-Magnet". In: *Proceedings of EPAC 2002, Paris, France*. 2002, pp. 2358–2360.

[94] S. Ryf et al. "Interference of neodymium magnets with cardiac pacemakers and implantable cardioverter-defibrillators: An in vitro study". In: *Technology and Health Care* 16.1 (2008), pp. 13–18. ISSN: 09287329. DOI: 10.3233/thc-2008-16102.

[95] A. Rishpon et al. "Assessment of the Safety Risk of Dermatoscope Magnets in Patients with Cardiovascular Implanted Electronic Devices". In: *JAMA Dermatology* 154.10 (2018), pp. 1204–1207. ISSN: 21686068. DOI: 10.1001/jamadermatol.2018.2531.

[96] M. H. Hebb. "Electrical conductivity of silver sulfide". In: *The Journal of Chemical Physics* 20.1 (1952), pp. 185–190. ISSN: 00219606. DOI: 10.1063/1.1700165.

[97] G. J. Russ. "Electrical Characteristics of Contacts Contaminated With Silver Sulfide Film". In: *IEEE Transactions on Parts, Materials and Packaging* 6.4 (1970), pp. 129–137. ISSN: 00189502. DOI: 10.1109/TPMP.1970.1136268.

[98] M. M. Yovanovich. "Four decades of research on thermal contact, gap, and joint resistance in microelectronics". In: *IEEE Transactions on Components and Packaging Technologies* 28.2 (2005), pp. 182–206. ISSN: 15213331. DOI: 10.1109/TCAPT.2005.848483.

[99] R. Fuger et al. "Scan techniques for coated conductors". In: *IEEE Transactions on Applied Superconductivity* 17.2 (2007), pp. 3753–3756. ISSN: 10518223. DOI: 10.1109/TASC.2007.899646.

[100] J. Gnilsen et al. "Current-voltage characteristics of double disordered REBCO coated conductors exposed to magnetic fields with edge gradients". In: *Superconductor Science and Technology* 32.10 (2019). ISSN: 13616668. DOI: 10.1088/1361-6668/ab3c09.

[101] T. Sueyoshi et al. "Influence of multiple angled columnar defects 011 critical current density and w-value in YBCO thin films". In: *Physics Procedia* 36 (2012), pp. 1570–1575. ISSN: 18753892. DOI: 10.1016/j.phpro.2012.06.212.

[102] M. Chudy et al. "N-Values of commercial YBCO tapes before and after irradiation by fast neutrons". In: *Superconductor Science and Technology* 28.3 (2015). ISSN: 13616668. DOI: 10.1088/0953-2048/28/3/035008.

[103] V. Pan et al. "Supercurrent transport in Y Ba2 Cu3 O7-δ epitaxial thin films in a dc magnetic field". In: *Physical Review B* 73.5 (2006), pp. 1–11. ISSN: 10980121. DOI: 10.1103/PhysRevB.73.054508.

[104] P. M. Leys et al. "Analysis of the anisotropic critical current behaviour of HTS coated conductors". In: *Journal of Physics: Conference Series* 507.PART 2 (2014), pp. 2–6. ISSN: 17426596. DOI: 10.1088/1742-6596/507/2/022013.

[105] X. Zhang et al. "General approach for the determination of the magneto-angular dependence of the critical current of YBCO coated conductors". In: *Superconductor Science and Technology* 30.2 (2017). ISSN: 13616668. DOI: 10.1088/1361-6668/30/2/025010.

[106] V. Drach and J. Fricke. "Transient heat transfer from smooth surfaces into liquid nitrogen". In: *Cryogenics* 36.4 (1996), pp. 263–269. ISSN: 00112275. DOI: 10.1016/0011-2275(96)88785-6.

[107] A. Usoskin et al. "Interchange of current between shunt layer and HTS film in long coated tapes". In: *Physica C* 372-376 (2002), pp. 857–862. ISSN: 09214534. DOI: 10.1016/S0921-4534(02)00872-9.

[108] M. Polak, P. N. Barnes, and G. A. Levin. "YBCO/Ag boundary resistivity in YBCO tapes with metallic substrates". In: *Superconductor Science and Technology* 19.8 (2006), pp. 817–820. ISSN: 09532048. DOI: 10.1088/0953-2048/19/8/022.

[109] G. A. Levin, K. A. Novak, and P. N. Barnes. "The effects of superconductor-stabilizer interfacial resistance on the quench of a current-carrying coated conductor". In: *Superconductor Science and Technology* 23.1 (2010). ISSN: 09532048. DOI: 10.1088/0953-2048/23/1/014021. arXiv: 0909.5209.

[110] M. Lao et al. "Planar current anisotropy and field dependence of J c in coated conductors assessed by scanning Hall probe microscopy". In: *Superconductor Science and Technology* 30.2 (2017). ISSN: 13616668. DOI: 10.1088/1361-6668/30/2/024004.

[111] V. Selvamanickam et al. "Correlation between in-field critical currents in Zr-added (Gd, Y)Ba 2Cu3Ox superconducting tapes at 30 and 77 K". In: *Superconductor Science and Technology* 27.5 (2014). ISSN: 13616668. DOI: 10.1088/0953-2048/27/5/055010.

[112] A. Xu et al. "Strong correlation between Jc(T, H//c) and Jc(77 K, 3 T//c) in Zr-added (Gd, Y)BaCuO coated conductors at temperatures from 77 down to 20 K and fields up to 9 T". In: *Superconductor Science and Technology* 28.8 (2015). ISSN: 13616668. DOI: 10.1088/0953-2048/28/8/082001.